

AD _____

Award Number: W81XWH-10-2-0101

TITLE: Design, Fabrication, Characterization and Modeling of Integrated Functional Materials

PRINCIPAL INVESTIGATOR: Professor Pritish Mukherjee

CONTRACTING ORGANIZATION: University of South Florida
Tampa, FL 33620

REPORT DATE: October 2011

TYPE OF REPORT: Annual

PREPARED FOR: U.S. Army Medical Research and Materiel Command
Fort Detrick, Maryland 21702-5012

DISTRIBUTION STATEMENT: Approved for public release; distribution unlimited

The views, opinions and/or findings contained in this report are those of the author(s) and should not be construed as an official Department of the Army position, policy or decision unless so designated by other documentation.

REPORT DOCUMENTATION PAGE				<i>Form Approved</i> OMB No. 0704-0188	
Public reporting burden for this collection of information is estimated to average 1 hour per response, including the time for reviewing instructions, searching existing data sources, gathering and maintaining the data needed, and completing and reviewing this collection of information. Send comments regarding this burden estimate or any other aspect of this collection of information, including suggestions for reducing this burden to Department of Defense, Washington Headquarters Services, Directorate for Information Operations and Reports (0704-0188), 1215 Jefferson Davis Highway, Suite 1204, Arlington, VA 22202-4302. Respondents should be aware that notwithstanding any other provision of law, no person shall be subject to any penalty for failing to comply with a collection of information if it does not display a currently valid OMB control number. PLEASE DO NOT RETURN YOUR FORM TO THE ABOVE ADDRESS.					
1. REPORT DATE (DD-MM-YYYY) 01-10-2011		2. REPORT TYPE Annual		3. DATES COVERED (From - To) 20 Sep 2010 - 19 Sep 2011	
4. TITLE AND SUBTITLE Design, Fabrication, Characterization and Modeling of Integrated Functional Materials				5a. CONTRACT NUMBER	
				5b. GRANT NUMBER W81XWH-10-2-0101	
				5c. PROGRAM ELEMENT NUMBER	
6. AUTHOR(S) Professor Pritish Mukherjee E-Mail: pritish@usf.edu				5d. PROJECT NUMBER	
				5e. TASK NUMBER	
				5f. WORK UNIT NUMBER	
7. PERFORMING ORGANIZATION NAME(S) AND ADDRESS(ES) University of South Florida Tampa, FL 33620				8. PERFORMING ORGANIZATION REPORT NUMBER	
9. SPONSORING / MONITORING AGENCY NAME(S) AND ADDRESS(ES) U.S. Army Medical Research and Materiel Command Fort Detrick, Maryland 21702-5012				10. SPONSOR/MONITOR'S ACRONYM(S)	
				11. SPONSOR/MONITOR'S REPORT NUMBER(S)	
12. DISTRIBUTION / AVAILABILITY STATEMENT Approved for Public Release; Distribution Unlimited					
13. SUPPLEMENTARY NOTES					
14. ABSTRACT The dynamically evolving needs of the U.S. soldier in the battlefield in response to changes in the technology of warfare and associated threats require advances in multiple areas including biomedical diagnostics, chemical sensing, communication technology, efficient power generation without increased payload, and mobile refrigeration. These technological advances are critically dependent on the development of new and currently non-existing materials. This research addresses the directed development of novel materials towards long-term needs of the United States Army. In order to address specific areas of integrated functional materials targeted towards the needs of the U.S. soldier in the field we have initiated research efforts in three main areas which are diagnostics and sensing, communication and energy, and power generation and refrigeration. The specific three independent "Tasks" that have been undertaken are: Task I: Nanostructured materials for biomedical diagnostics and chemical sensing Task II: Multifunctional composites for communication and energy applications Task III: Solid-state materials for power generation and refrigeration The specific outcome of the research activities is expected to lead to new devices/systems/composite materials useful for the USAMRMC.					
15. SUBJECT TERMS Functional materials, integrated fabrication, nanobiotechnology, smart materials, multifunctional, dimensional integration, nanocomposites, sensor technology, thermoelectrics, solar cells, photovoltaics, polypeptide multilayer films					
16. SECURITY CLASSIFICATION OF:			17. LIMITATION OF ABSTRACT UU	18. NUMBER OF PAGES 82	19a. NAME OF RESPONSIBLE PERSON USAMRMC
a. REPORT U	b. ABSTRACT U	c. THIS PAGE U			19b. TELEPHONE NUMBER (include area code)

Design, Fabrication, Characterization and Modeling of Integrated Functional Materials
(Program Director and PI: Prof. Pritish Mukherjee, Department of Physics, USF, Tampa, FL)
(co-PIs: Profs. Hariharan Srikanth, Sarath Witanachchi and George Nolas)
(Contributing Faculty: Prof. Donald Haynie)

Table of Contents

	<u>Page</u>
I. Introduction.....	4
II. Technical Description of Research Progress.....	6
III. Reportable Outcomes.....	70
IV. Conclusion.....	73
V. Bibliography.....	78

Design, Fabrication, Characterization and Modeling of Integrated Functional Materials
(Program Director and PI: Prof. Pritish Mukherjee, Department of Physics, USF, Tampa, FL)
(co-PIs: Profs. Hariharan Srikanth, Sarath Witanachchi and George Nolas)
(Contributing Faculty: Prof. Donald Haynie)

I. Introduction

The dynamically evolving needs of the U.S. soldier in the battlefield in response to changes in the technology of warfare and associated threats require advances in multiple areas including biomedical diagnostics, chemical sensing, communication technology, efficient power generation without increased payload, and mobile refrigeration. These technological advances are critically dependent on the development of new and currently non-existing materials. This research addresses the directed development of novel materials towards long-term needs of the United States Army.

Objective:

In addition to the integration of multiple functionalities with desirable properties (thermal, electrical, magnetic, mechanical, optical, etc.), the connection to real-world applications and devices also requires the seamless integration of dimensions (nano, micro, meso, macro) leading to integrated functional materials. We have initiated this Integrated Functional Materials Project at the Physics Department at the University of South Florida (USF) geared towards precisely addressing this grand challenge of dual integration. A series of targeted projects specifically address a spectrum of issues relevant to the needs of the U.S. soldier.

Specific Aims:

The Physics Department at the University of South Florida is home to a unique doctoral program in Applied Physics with an affiliated industrial practicum and nationally recognized research programs in physical and chemical materials synthesis and characterization of bulk materials, thin films and nanomaterials; crystal fiber growth; fundamentals of materials manufacturing processes and computational theoretical materials physics. This research synergistically coalesces existing expertise and leverages research infrastructure at USF in novel bulk materials synthesis, thin film growth, and nanotechnology. These goals are being further addressed through multidisciplinary research and new infrastructure development. The basic purpose of this project is to develop the novel science base both in the areas of multi-scale dimensional integration as well as multiple functional integration leading to previously unattained integrated functional materials.

Study Design:

In order to address specific areas of integrated functional materials targeted towards the needs of the U.S. soldier in the field we are directing the research efforts in three main areas which are diagnostics and sensing, communication and energy, and power generation and refrigeration. The specific three independent “Tasks”, further subdivided into seven “Projects” are:

Task I: Nanostructured materials for biomedical diagnostics and chemical sensing

(Technical Directors.: Drs. H. Srikanth and P. Mukherjee)

- Project 1* Functional magnetic fluids for biomedical applications
- Project 2* Nanoporous/nano-wire structures and polymer nanotemplates for sensing and molecular manipulation
- Project 3* Carbon-nanotube based sensors
- Project 4* Functional materials for affecting cell proliferation and locomotion

Task II: Multifunctional composites for communication and energy applications

(Technical Director: Dr. S. Witanachchi)

- Project 5* Tunable multifunctional nano- and heterostructures for RF and microwave applications
- Project 6* Flexible photonic materials for solar-based energy sources

Task III: Solid-state materials for power generation and refrigeration

(Technical Director: Dr. G. S. Nolas)

- Project 7* High-performance nanofabricated thermoelectric materials for power generation and refrigeration

II. Technical Description of Research Progress

The following discussion details the progress made on each of the Tasks during the fourth year of research (the first year of continuation funding):

Task I: Nanostructured materials for biomedical diagnostics and chemical sensing

The goal of this project is to synthesize and characterize advanced magnetic nanoparticles and nanocomposites for high-performance sensor and biomedical applications. During this 2010-2011 project duration, we have successfully fabricated a wide range of ferrite nanoparticles with controlled size and shape, their magnetic polymer nanocomposites, carbon nanotubes (CNTs) filled with these nanoparticles, graphene patterned with the nanoparticles, and their structure, magnetic and microwave properties have been studied systematically. We have conducted the first studies of the impacts of coating and exchange anisotropy on the giant magneto-impedance (GMI) effect, providing new ways for tailoring the material properties for high-performance magnetic sensor applications. We have discovered that the GMI effect can be enhanced in a ferromagnetic ribbon coated with CNTs. This new finding suggests the possibility for developing a new class of CNT-based gas/chemical sensors that operate based on the principle of GMI effect. We have also shown that GMI can be a promising biosensor for detection of cancer cells and biomolecules that have taken up magnetic nanoparticles. A graduate student Mr. Sayan Chandra received support and worked on this project. In addition, a graduate student Ms. Kristen Stojak, undergraduate student Mr. Ramon Ruiz, and Research Assistant Professor Dr. Manh-Huong Phan were key contributors to the project. A summary of our research activities in the year 2010-2011 is presented below:

(a) Shape-controlled Synthesis and Magnetic Properties of Magnetite Nanoparticles:

Magnetite nanoparticles (Fe_3O_4) are technologically important materials for sensor and biomedical applications. A shape-controlled synthesis of monodisperse Fe_3O_4 nanoparticles is a great challenge to the materials scientist [1]. Here we report the synthesis, structural and magnetic characterization of uniform cubic Fe_3O_4 nanoparticles.

Synthesis:

To synthesize Fe_3O_4 nanoparticles, we followed a standard thermal decomposition method [2] in which we mix 2 mmol of Iron (III) acetylacetonate with 1,2-hexadecanediol, 6 mmol oleic acid, 6 mmol oleylamine and varying amounts of benzyl ether depending on the size we desired. We then magnetically stirred the particles while flowing argon. We heated the system to 200 degrees C for 2 hours and 300 degrees C for one hour to reflux. We then let the system cool to room temperature naturally and add 40 ml of ethanol to wash the particles. We centrifuged the resulting solution at 5000 rpm for 5 minutes, dispose of the chemical waste from process, and repeated washing by centrifugation until the

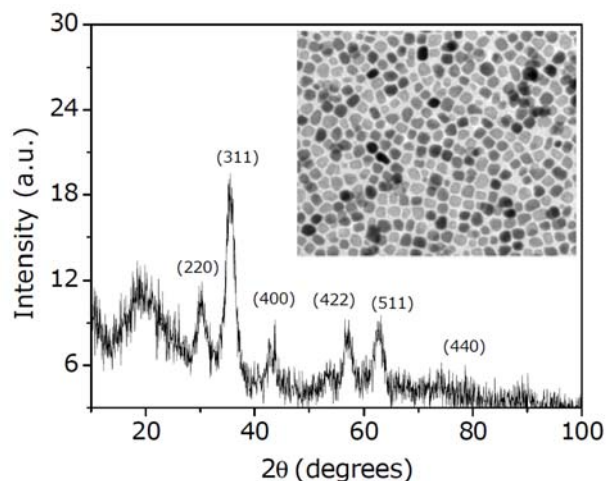


Fig. 1 XRD and TEM of Fe_3O_4 nanoparticles

liquid was clear, indicating that the particles are clean. The washed particles were then suspended in hexane in the presence of a small amount of oleic acid and oleylamine (~0.5 ml each) and centrifuged again at a higher rpm to remove any larger particles from the system. The result is typically 16 nm \pm 1 nm Fe₃O₄ nanoparticles which are then characterized by XRD, TEM and PPMS.

Results and discussion:

The XRD pattern and TEM image of Fe₃O₄ nanoparticles are shown Fig. 1 and its inset. The as-synthesized nanoparticles were identified as the cubic spinel structure of Fe₃O₄ with the average diameter of 16 nm \pm 1 nm. The nanoparticles are cubic and mono dispersed. Figure 2a shows the zero-field-cooled (ZFC) and field-cooled (FC) M-T curves of 16 nm Fe₃O₄ cubic nanocrystals. The blocking temperature (T_B) of the nanoparticles is ~100 K, which is larger than that of the spherical nanoparticles [2]. The M-H data taken at temperatures below T_B are shown in inset of Fig. 2b. As expected, the coercivity (H_c) and saturation magnetization (M_s) increase with lowering temperature (see Fig. 2b). Above T_B , $H_c \sim 0$ Oe, the sample behaves superparamagnetically.

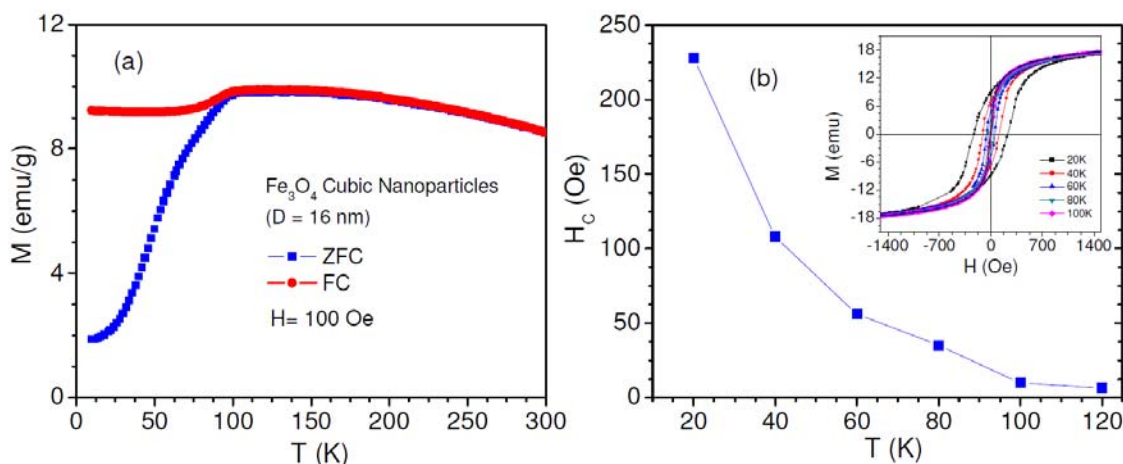


Fig. 2 (a) ZFC and FC M-T curves of Fe₃O₄ cubic nanoparticles and (b) temperature dependence of coercivity (H_c) and M-H curves at different temperatures shown in inset of Fig. 2b.

Overall, we have successfully synthesized the monodisperse, cubic Fe₃O₄ nanoparticles in a controllable fashion. Such nanoparticles are useful for a variety of sensor and biomedical applications. For example, they could have utility in biomedical immune-electron microscopy allowing differentiation by both size and shape simultaneously. It is important to note that magnetic nanoparticles with tunable shapes and sizes provide more magnetic labeling options that are currently restricted to spherical particles below 15 nm in size [3]. Once shape-variant MNPs are used, different biological molecules (eg: proteins, lipids) can be labeled to simultaneously target different sites within a single sample, giving a direct comparison of signaling networks or multi-subunit molecular machines. In our research, some of them were used for making their magnetic polymer and graphene nanocomposites as outlined below.

(b) Magnetic Polymer Nanocomposites for Sensor and Microwave Device Applications:

Incorporation of monodisperse magnetic nanoparticles into a polymer matrix for making novel magnetic polymer nanocomposites for a wide range of sensor and RF microwave device applications is of topical interest [4,5]. We report here the synthesis, structural and magnetic

characterization and tunable microwave properties of Rogers – CoFe_2O_4 nanocomposites. Our studies reveal that these nanocomposites are excellent candidate materials for such applications.

Synthesis:

CoFe_2O_4 nanoparticles were synthesized using a thermal decomposition method [6] by mixing 1 mmol of cobalt (II) acetylacetonate, 2 mmol of iron (III) acetylacetonate, 10 mmol 1,2-hexadecanediol, 6 mmol oleic acid, 6 mmol oleylamine, and 20 ml benzyl ether. The mixture was stirred magnetically in the presence of argon gas and was heated at 200°C for 2 hr and then refluxed at 300°C for 1 hr. The mixture was allowed to cool to room temperature by removing the heat source and 40 ml ethanol was added once cool. A black precipitate formed in the presence of ethanol and was centrifuged to collect the desired particles and remove any chemical waste. The black product was dissolved in hexane in the presence of oleic acid and oleylamine ($\sim 0.05\text{ml}$ each) to create a ferrofluid. The polymer nanoparticle composites (PNCs) were made by adding the synthesized particles to Rogers Polymer (a low-loss, high-temperature thermosetting resin provided by the Rogers Corporation). A calculated amount nanoparticles and polymer were then mixed together to create composites with different loadings. Each sample was left stirring with a magnetic stir bar overnight to ensure uniform dispersion of nanoparticles within the polymeric matrix. Once the solutions were formed, the PNC material was drop-casted onto a multilayer microstrip linear resonator and heated in a vacuum oven to evaporate the solvent and cure the polymer. PNCs were made to be 30 wt%, 50 wt% and 80 wt% in films as thick as $435\ \mu\text{m}$.

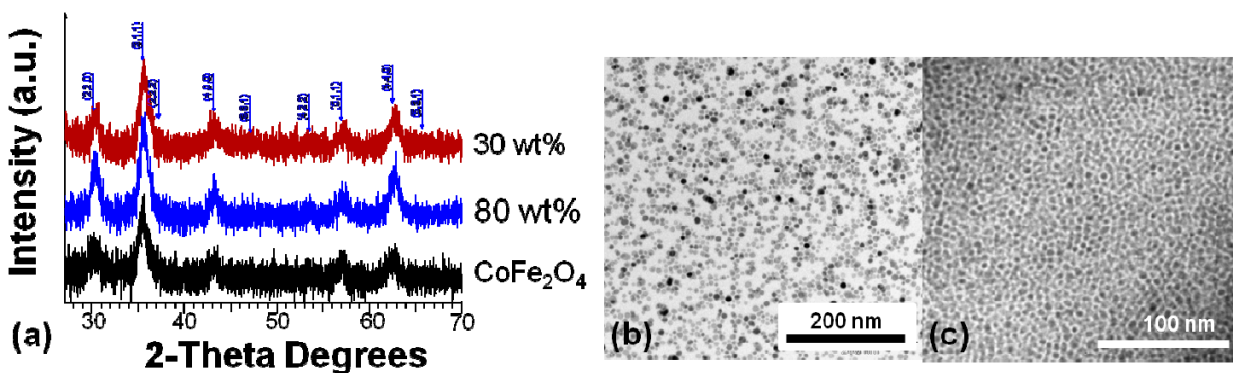


Fig. 3 (a) XRD plot of pure CoFe_2O_4 nanoparticles, 30 wt% PNC, and 80wt% PNC; (b) TEM image of pure CoFe_2O_4 nanoparticles; and (c) TEM image of 50 wt% composite.

Results and discussion:

Fig. 3a shows the XRD plot of the pure CoFe_2O_4 nanoparticles compared to the highest and lowest weight percentages. The synthesized nanoparticles and the composites alike are of the same phase, indicating that any heating of the PNCs did not affect the phase of the nanoparticles.

Fig. 3b and 3c show TEM images of the $10 \pm 1\ \text{nm}$ CoFe_2O_4 nanoparticles alone and within the 50 wt% composite, respectively. In both cases, the particles are well-separated and free from any agglomeration.

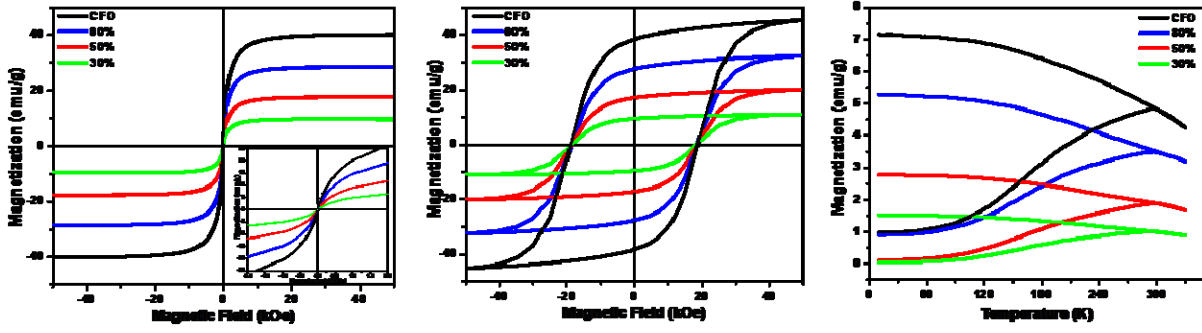


Fig. 4 (a) M-H curves at 300K for different concentrations of CoFe₂O₄ in Rogers Polymer with inset showing zero coercivity; (b) M-H curves at 10K for the same concentrations showing coercivity of 18 kOe; and (c) M-T curves for same concentrations showing a T_B of ~298 K for all samples.

Magnetization vs. magnetic field (M-H) measurements at 300 K show curves of varying saturation magnetizations (M_s) based on the different loadings of the PNCs all with zero coercivity, confirming the superparamagnetic behavior of the samples at room temperature (**Fig. 4a**). **Fig. 4b** shows that M-H measurements at 10 K display the same pattern of varying M_s with loading of particles and also a coercivity of ~18 kOe for all samples. Note that the large coercivity in this system is expected because of large magnetic anisotropy of the CoFe₂O₄ system. Magnetization vs. temperature measurements reveal a blocking temperature (T_B) of ~298 K for the CoFe₂O₄ nanoparticles and all three PNCs, shown in **Fig. 4c**. This is beneficial for many commercial applications as both the ferromagnetic and superparamagnetic states of the material are accessible near room temperature. Also note that since the M_s changes with particle loading, but the T_B does not, these PNCs display a tunable magnetization.

To test the microwave response of the Rogers-CoFe₂O₄ PNCs, a two-port microstrip linear resonator was designed using the multilayer structure shown schematically in **Fig. 5a**. The resultant frequency of the resonator relies on the effective material properties of the implemented substrate following the relation, $F_r \sim 1/(\epsilon\mu)^{1/2}$ with μ and ϵ being the effective permeability and permittivity, respectively, for the multilayer system. **Fig. 5b** presents the measured transmission characteristics of the aforementioned resonator with embedded PNC as a function of frequency for several different magnetic fields, ranging from zero magnetic field to 4500 Oe for the 80 wt% sample. The observed variations in the resonance frequency are due to the changes in the permeability and permittivity of the PNC. **Fig. 5c** shows a plot of the quality factor and the frequency as a function of magnetic field, also of the 80 wt% sample. Observe the sharp increase in both of these parameters as the magnetic field is increased. Note that the changes in the magnitude of the transmission characteristics and the quality factor of the device are also partially related to the variation in the effective losses of the nanocomposite material.

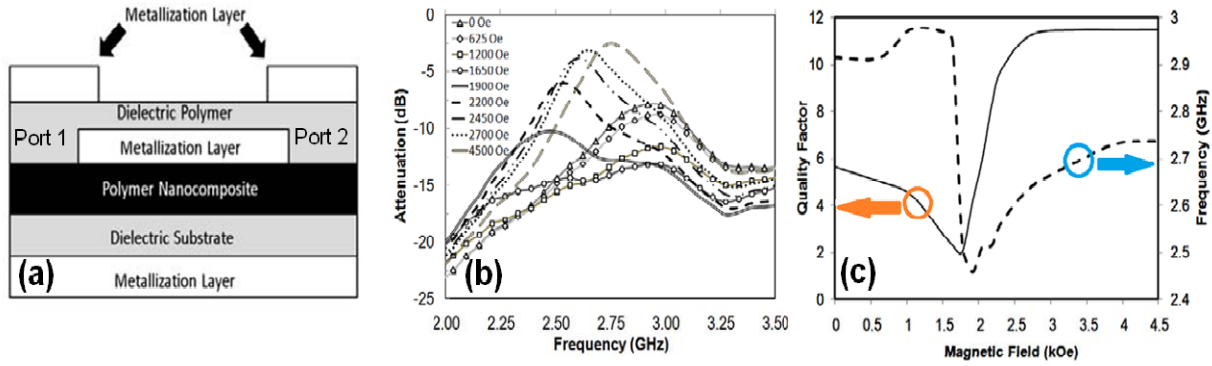


Fig. 5 (a) Cross-sectional diagram of the multilayer microstrip resonator; (b) Measured transmission characteristics of the microstrip linear resonator with embedded CoFe_2O_4 -Rogers nanocomposite of 80% loading; and (c) Quality factor and frequency as a function of magnetic field.

Overall, we have demonstrated an excellent control over nanoparticle dispersion in the Rogers-CFO nanocomposites, and their tunable magnetic and microwave properties make them truly attractive for applications in biomedical sensing and microwave communication devices. These results have been published in *Nanotechnology* 2011.

(c) High-aspect ratio magnetic nanostructures for biosensor and microwave device applications

Recently we have introduced a new concept of incorporating superparamagnetic nanoparticles such as Fe_3O_4 and CoFe_2O_4 into a polymer matrix to create a new class of nanocomposite materials with tunable microwave response [5,7]. We propose that the microwave response can be further enhanced in high-aspect ratio magnetic nanostructures, such as carbon nanotubes (CNTs) filled with supermagnetic nanoparticles [8], where the magnetic anisotropy can easily be tuned by varying the size and density of magnetic nanoparticles inside CNTs. We reported on the fabrication method and structural and magnetic characterization of CNTs filled with CoFe_2O_4 nanoparticles. We have demonstrated that the high compacting of CoFe_2O_4 nanoparticles inside CNTs can enhance the saturation magnetization and shape anisotropy, both of which are desirable for enhancing the microwave absorption properties for sensor and microwave device applications. High saturation magnetization and shape anisotropy achieved in our magnetic nanotubes indicate their usefulness not only for microwave and sensor device applications, but also for others such as cantilever tips in magnetic force microscopes, CNT-based biomedical agents, and as interconnects in hybrid CMOS spintronic devices. Some of the main results are highlighted below.

Synthesis:

CoFe_2O_4 nanoparticles were synthesized by the thermal decomposition method. The CNTs were synthesized using a multi-step chemical vapor deposition method [8]. We used alumina templates with pore sized reported as 200 nm from a commercial vender as the carrier for the tubes. Before the growth of the CNTs, the alumina templates were placed between two quartz slides and heated to 740°C for one hour to prevent bending of the templates during CNT growth. The heat-treated alumina templates were then placed vertically inside a quartz tube already seated in the CVD reactor furnace and the temperature was increased to 670° in the presence of argon. Once the temperature was stable at 670°C , the argon was turned off and 30 sccm ethylene

and 70 sccm helium were set to flow for 6 hours. When the reaction was finished, the furnace was turned off, the ethylene was turned off, the argon was turned back on and the template was allowed to cool to room temperature under the flow of helium and argon. The resulting CNTs were between 250 and 300 nm in diameter on average. This increase in expected size is most likely due to the pore size being non-uniform through the depth of the 60 μm templates. The black template filled with CNTs was then placed on a 0.4 T permanent laboratory magnet (**Fig. 6**) and the synthesized ferrofluid was dropped onto the template. The magnetic field created by the permanent laboratory magnet was enough to pull the nanoparticles into the CNTs through capillary motion. Once the CNTs were filled, the alumina template was dissolved in a 7.0 M

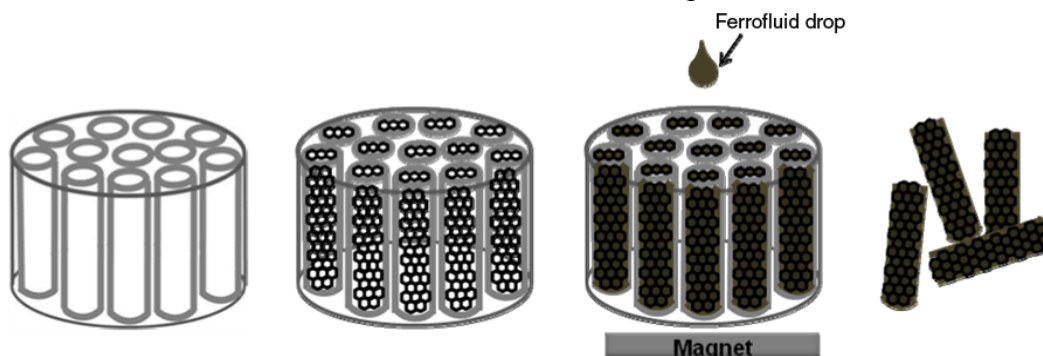


Fig. 6 Schematic of the method for synthesis of CoFe_2O_4 -filled CNTs.

NaOH solution and vacuum filtered through a polyester nucleopore membrane. After filtration, the residue was rinsed with toluene to remove any stray nanoparticles from the surface of the membrane. The residue was then rinsed with isopropanol and deionized water several times and dried at room temperature. The dry sample was collected for characterization.

Results and discussion:

Figure 7 shows the XRD pattern of CoFe_2O_4 nanoparticles. The nanoparticles were identified as the cubic spinel structure of CoFe_2O_4 . The inset of Fig. 1 shows the TEM image of spherical shaped monodisperse nanocrystals with diameter of $7\text{ nm} \pm 1\text{ nm}$. **Figure 8** shows TEM images of CNTs with an average diameter of 250-300 nm and those filled with CoFe_2O_4 nanoparticles. The magnetic properties of CoFe_2O_4 nanoparticles and CoFe_2O_4 -filled CNTs were investigated using the physical property measurement system (PPMS) from Quantum Design. **Figure 9a** shows the temperature dependence of zero-field-cooled (ZFC) and field-cooled (FC) magnetization in a magnetic field of 100 Oe for CoFe_2O_4 nanoparticles and CoFe_2O_4 -filled CNTs. It is very interesting to note in this figure that the blocking temperature ($T_B = 264\text{ K}$) of

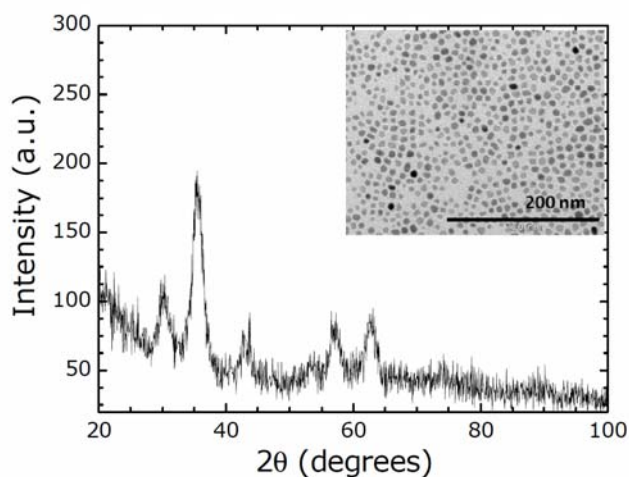


Fig. 7 XRD of 7 nm CoFe_2O_4 nanoparticles. In inset: TEM of these nanoparticles.

the CoFe₂O₄-filled CNTs is significantly larger than that of the CoFe₂O₄ nanoparticles ($T_B = 224$ K). As one can see clearly in **Fig. 9b**, the saturation magnetization ($M_S = 37.1$ emu/g) of the CoFe₂O₄-filled CNTs is slightly larger compared with that of the CoFe₂O₄ nanoparticles ($M_S = 36$ emu/g). These results indicate that inter-particle interactions are stronger in the CoFe₂O₄-filled CNTs than in the CoFe₂O₄ nanoparticles.

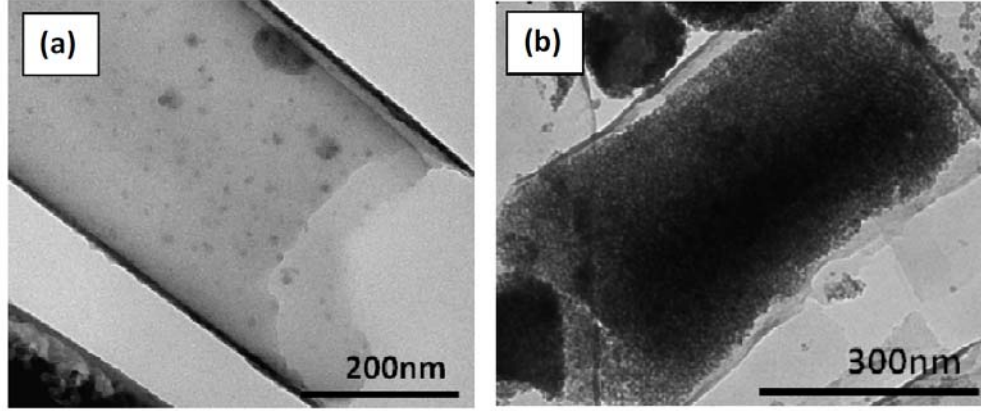


Fig. 8 TEM images of (a) As-synthesized CNT; (b) CoFe₂O₄-filled CNT.

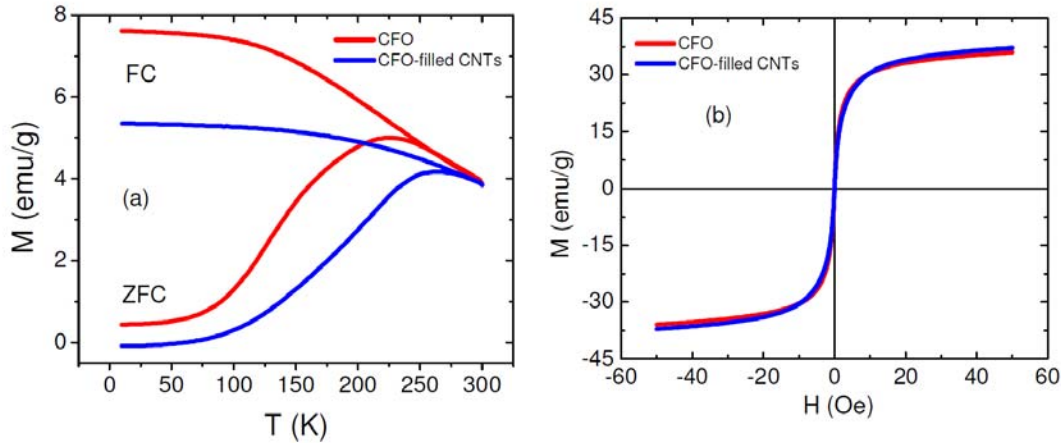


Fig. 9 (a) Temperature dependence of zero-field-cooled (ZFC) and field-cooled (FC) magnetization of CoFe₂O₄ nanoparticles and CoFe₂O₄-filled CNTs; (b) M-H curves taken at 300 K.

In the ferromagnetic regime ($T < T_B$), we have found that the saturation magnetization (M_S) increases and the coercivity (H_C) decreases as temperature decreases (**Fig. 10**). The temperature dependence of H_C , as extracted from the M-H curves, can be described by

$$H_C = H_{co} \left[1 - \left(\frac{T}{T_B} \right)^{\frac{1}{2}} \right], \quad (1)$$

where $T_B = K_u V / 25 k_B$ and $H_{co} = 2\alpha K_u / M_S$ with $\alpha = 0.48$ being a phenomenological constant. From fitting the $H_C(T)$ data using Eq. 4, we have determined $T_B \sim 225$ K for the 7 nm Fe₃O₄ nanoparticles. This value of T_B is consistent with that obtained from the M-T data.

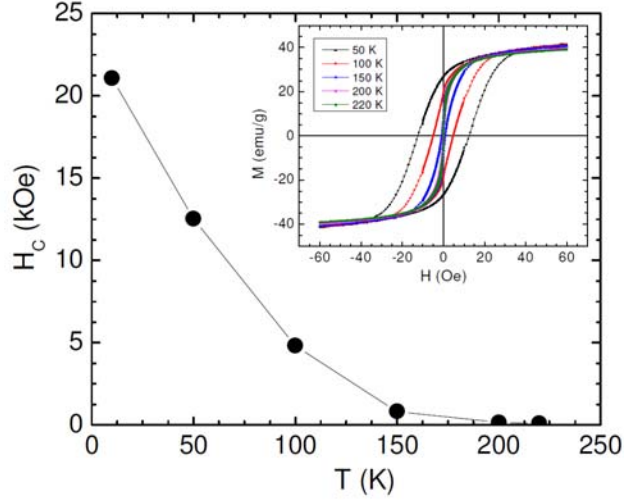


Fig. 10 Temperature dependence of coercivity (H_C) of CoFe_2O_4 nanoparticles. The insets shows M-H loops measured at different temperatures below T_B .

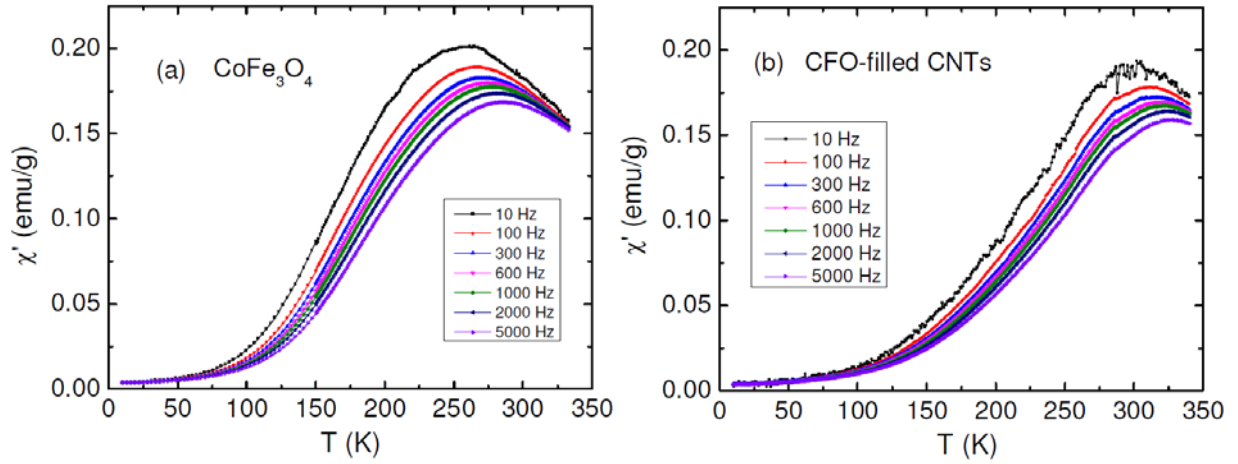


Fig. 11 (a) Temperature dependence of the real component of ac susceptibility of CoFe_2O_4 nanoparticles; (b) Temperature dependence of the real component of ac susceptibility of CoFe_2O_4 nanoparticle-filled CNTs.

Measurements of the AC susceptibility and analysis give important clues about the spin dynamics and the role of interactions between nanoparticles forming clusters or arrays. Therefore, we have conducted temperature-dependent ac susceptibility measurements at different frequencies. **Fig. 11a,b** shows these data. The magnetic relaxation processes in nanoparticle systems are studied by analyzing the frequency dependence of the peaks in $\chi'(T)$ and $\chi''(T)$ and fitting these experimental data either to the Néel-Arrhenius (NA) model,

$$\tau = \tau_o \exp(E_a / kT) \quad (2)$$

or Volgel-Fulcher (VF) scaling law,

$$\tau = \tau_o \exp[E_a / k(T - T_o)], \quad (3)$$

where τ is the relaxation time ($\tau = 1/f$; f is the frequency), τ_o is the microscopic flipping time of the fluctuating spins, E_a is the thermal activation energy, T is the temperature, and T_o is the characteristic temperature with thermal energy dominating for $T > T_o$ and interaction energy for $T < T_o$. We have found that the data of both samples fit the Vogel-Fulcher model, indicating dipolar interparticle interactions in these systems. Interestingly, the CoFe_2O_4 -filled CNTs show enhanced interparticle interactions relative to the CoFe_2O_4 nanoparticles. These results reveal the new possibility of tuning the magnetic properties of CoFe_2O_4 -filled CNTs for sensor and microwave device applications. We are planning to systematically investigate magnetic anisotropy that plays a key role in controlling the magnetic properties in nanoparticle assemblies. In addition to the standard DC and AC magnetization measurements with the PPMS, we will conduct resonant radio-frequency (RF) transverse susceptibility measurements and broadband microwave measurements using vector network analyzers on magnetic CNTs and magnetic CNTs embedded in a polymer matrix. A manuscript is being written and targeted for publication in *Applied Physics Letters*, 2011.

(d) Graphene and Magnetic Nanoparticle-Patterned Graphene Nanocomposites

Graphene is a very interesting candidate for future electronics due to its unique conduction properties, while monodisperse, single domain magnetic nanoparticles (NPs) have shown promise for applications spanning magnetic data storage to biomedical drug delivery, tagging, and hyperthermic cancer treatment [9,10]. In all cases the efficacy is directly tied to the collective magnetic behavior, or “cross-talk”, between NPs. Combining graphene and magnetic NPs together is expected to create an interesting nanocomposite with unique magnetic and electrical properties.

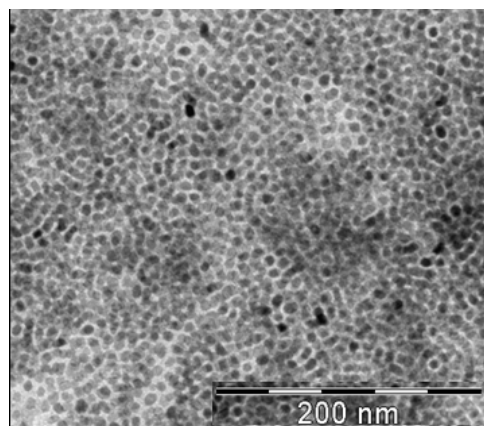


Fig. 12 TEM of monodisperse 9 nm Fe_3O_4 nanoparticles packed on graphene.

Our goals are to grow graphene over a large area and to use graphene as a functional substrate on which magnetic nanoparticle assemblies can be created using Langmuir-Blodgett (LB) deposition of monolayers and multilayers. Due to the presence of excess free electrons on a graphene surface, the possibility of graphene-mediated long-range interactions between Fe_3O_4 NPs would open up new avenues of research and device development. This work has been mainly done by a CIFM graduate student, Sayan Chandra, who is working on this system towards his Ph.D. degree. We outline below the synthesis, structural, magnetic, and neutron scattering characterization of graphene and related nanocomposites.

Synthesis:

We have successfully advanced a simple thermal decomposition synthesis method [11] for growth of high quality graphene. In this method, methane is passed over a thin film of Ni on a SiO_2/Si substrate at 900 °C, and as the methane molecules break at such high temperatures, the carbon diffuses into the Ni. During the cooling process, carbon precipitates out as graphene. We have optimized that cooling at 10°C/s produces high quality graphene. Graphene was then patterned with magnetic nanoparticles (e.g. Fe_3O_4 , CoFe_2O_4) using LB method.

Results and discussion:

We produced continuous sheets of $1 \times 1 \text{ cm}^2$ of graphene with layer variation up to 10 layers. Monolayers up to a few microns in length were achievable. It is challenging to get larger monolayer sheets because its size is limited by the size of the Ni grains which acts as the substrate. Ripples and stacking of layers were observed at the grain boundaries because of the difference in thermal expansion co-efficient of graphene and nickel. Raman spectroscopy studies also confirmed the quality of the fabricated graphene. **Fig. 12** shows the TEM image of 10 layer Fe_3O_4 nanoparticles deposited on graphene using LB method. AFM images revealed flat regions with mean roughness of 6.5 nm in the selected area and distribution of Fe_3O_4 NPs except accumulation at the grain boundaries. One distinct advantage of the LB method is that the average spacing between NPs, particularly in monolayer form, is controllable – allowing us to extract the role that the graphene plays in long-range interactions under circumstances where dipolar coupling is minimal and study the effect of size of nanoparticles.

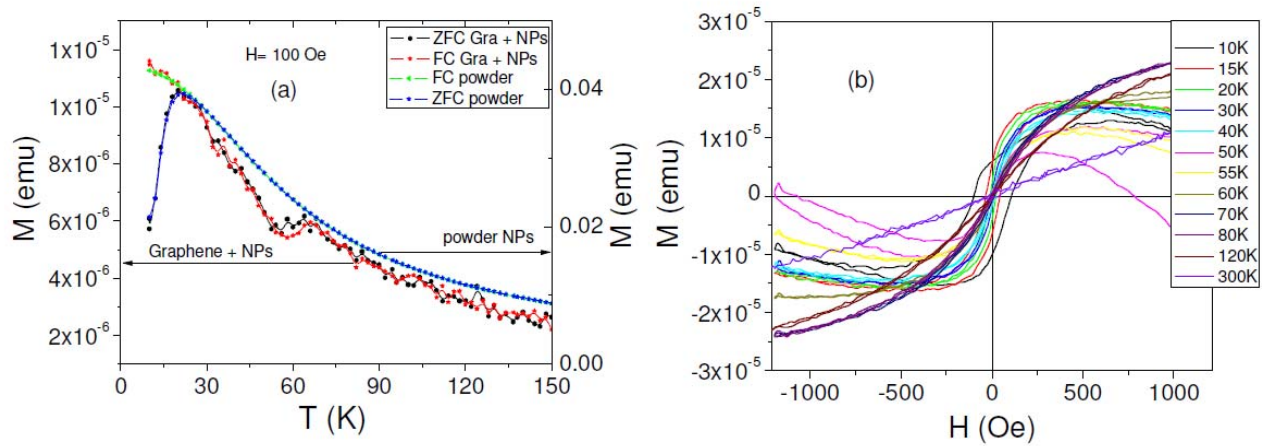


Fig. 13 (a) Temperature dependence of zero-field-cooled (ZFC) and field-cooled (FC) magnetization for 6nm powder Fe_3O_4 NPs and graphene-NPs composite; (b) the evolution of magnetization vs. field for the composite with temperature.

In **Fig. 13a** we present the M-T behavior for the powder and graphene-NPs (6nm) composite. We observe a blocking peak T_B at about 20 K for both the powder and nanocomposite, and another peak is observed at a higher temperature of 65 K for the nanocomposite sample. We observe a change in the shape of the M-H (**Fig. 13b**) curves from saturating to non-saturating at the temperature of 65 K. We believe the high temperature peak is due to formation of long-range ordering in the graphene-NPs sample which is absent in the bare powder sample. The long-range ordering disintegrates above 75 K and we observe a gradual decrease in magnetization. Identical features are observed for the 9 nm set of samples too (see **Fig. 14a,b**).

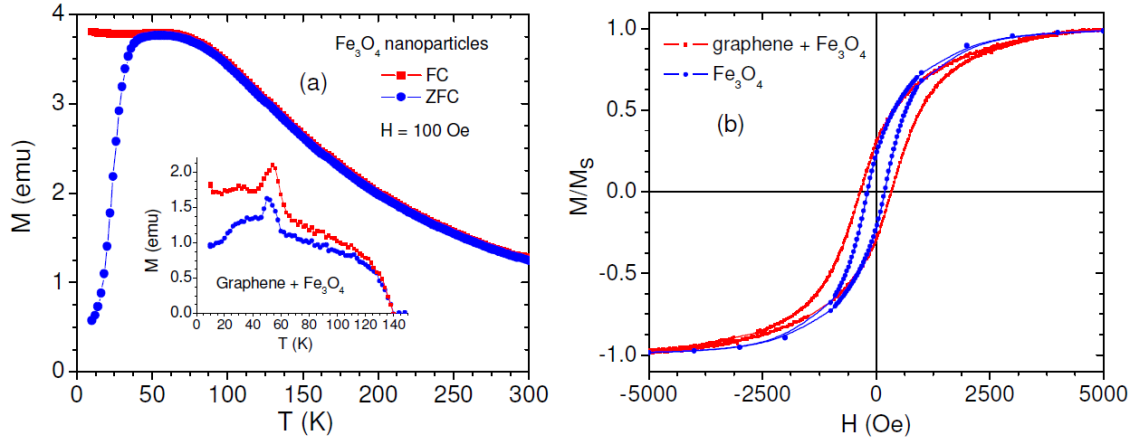


Fig. 14 (a) Temperature dependence of magnetization and (b) Magnetic field dependence of magnetization taken at 10 K for Fe_3O_4 NPs and graphene- Fe_3O_4 composite.

To investigate the extent of long range ordering within the NPs and its temperature dependence, we have used off-specular neutron scattering, which is generally more sensitive by orders of magnitude to magnetic moments than x-rays, as the most appropriate ensemble probe. We turn to off-specular neutron scattering (position-sensitive detector) [12] to determine the long-range in-plane domain formation as a function of field between remanence and saturation (5 kG). Preliminary data on our 8 nm NP on graphene sample suggest that the domain formation

observed from zero-field cooling compared with saturation (measured at 7500 G) are much longer-ranged, on the order of several microns, presumably mediated by the graphene (**Fig. 15**).

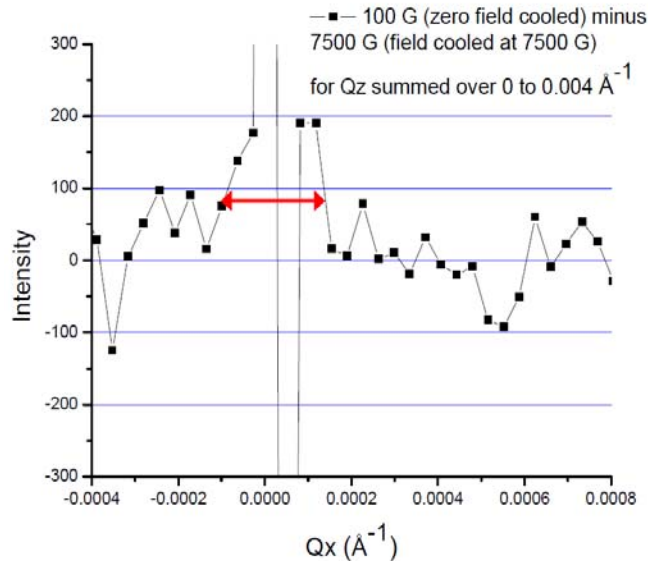


Fig. 15 Intensity vs. Q_x plot indicating the difference in off-specular scattering in case of 100 Oe and 7500 Oe. The FWHM of the Gaussian fit gives us an estimate of the extent of long range ordering in the nanoparticles.

These new findings point to the enhancement of graphene-mediated magnetic interactions in the nanocomposites. We have been extensively investigating the influences of particle size and shape on the graphene-mediated magnetic interactions in the nanocomposites. Our systematic studies on the underlying mechanism of magnetic interactions between graphene-mediated nanoparticles, and proximity effects at the interface between the nanoparticles and graphene that likely influences the magnetic anisotropy and also exchange bias in the graphene-

nanoparticle composites will yield transformative new insights into carbon based composite magnetic structures for a wide range of sensor and spintronic device applications.

(e) Nanocomposites with Giant Magneto-Impedance Effect for Sensor Applications

The goal of our research is to explore GMI effect in a variety of magnetic materials for applications ranging from magnetic sensors to bio-molecular detection. A graduate student, Mr. Anurag Chaturvedi, worked on this project and just successfully defended his PhD degree in June. Another graduate student, Ms. Kristen Stojak, and undergraduate students Mr. Ramon Ruiz and Nick Laurita have also worked on this project.

Introduction:

GMI is a large change in the ac impedance of a ferromagnetic conductor subject to a dc magnetic field [13]. The impedance (Z) of a ferromagnetic ribbon can be calculated by

$$Z = R_{dc} \cdot jka \coth(jka), \quad (4)$$

where a is half of the thickness of the ribbon, R_{dc} is the electrical resistance for a dc current, j =imaginary unit, and $k = (1+j)/\delta_m$. It is related to the skin effect characterized by the skin depth (δ_m), which, in a magnetic medium, is given by

$$\delta_m = \sqrt{\frac{\rho}{\pi \mu_T f}}, \quad (5)$$

where ρ is the electrical resistivity, μ_T is the transverse magnetic permeability, and f is the frequency of the ac current. The application of a dc magnetic field H_{dc} changes μ_T , and consequently δ_m and Z . A large GMI effect should exist in soft ferromagnetic materials, such as Co-based amorphous and Fe-based nanocrystalline ribbons.

A new area of study in nanocomposite materials has been in Co-rich alloys in which 2- or 3- nanocrystalline phases have been seen simultaneously within an amorphous matrix. The mechanism for induced magnetic anisotropy in these alloys has been an area of active inquiry. Recently, Ohodnicki Jr et al. [14] reported on the large field-induced anisotropies in $(\text{Co}_{1-x}\text{Fe}_x)_{89}\text{Zr}_7\text{B}_4$ ($0 \leq x \leq 0.1$) nanocrystalline ribbons, which were obtained by annealing the corresponding amorphous ribbons at 540 °C for 1 hour in a large field of 2 T applied perpendicular to the ribbon axis. Since the magnitude of the field-induced anisotropy field significantly varies with Fe doping, these materials are of potential interest for GMI studies.

Experiment:

$(\text{Co}_{1-x}\text{Fe}_x)_{89}\text{Zr}_7\text{B}_4$ ($x = 0, 0.025, 0.05, \text{ and } 0.1$) nanocrystalline ribbons were obtained by annealing the corresponding amorphous ribbons at 540 °C for 1h in a field of 2 T applied perpendicular to the ribbon axis. Magneto-impedance measurements were conducted along the ribbon axis in dc magnetic fields up to 120 Oe over a frequency range of 0.1 ~ 10 MHz with a constant ac current of 5 mA [15]. The GMI ratio and the magnetic field sensitivity of GMI ratio are defined as $\Delta Z/Z = 100\%(Z(H)-Z(H_{\max}))/Z(H_{\max})$ and $\eta = d/dH(\Delta Z/Z)$, where $Z(H)$ and $Z(H_{\max})$ represent the impedance in a magnetic field H and in the maximum field ($H_{\max} = 120$ Oe) respectively.

Results and Discussion:

We have demonstrated the possibility of tuning magnetic anisotropy and hence the GMI effect and its field sensitivity (η) in nanocomposite $(\text{Co}_{1-x}\text{Fe}_x)_{89}\text{Zr}_7\text{B}_4$ ribbons with $x = 0, 0.025, 0.05$, and 0.10 (see **Fig. 16**). We have found that for the amorphous samples the GMI ratio tends to decrease with Fe doping, while the largest value of η is achieved for the $x = 0.025$ composition. For the nanocrystalline samples, the GMI ratio and η first decrease with increase of Fe-doped content from $x = 0$ to $x = 0.05$ and then increase for $x = 0.1$. The field annealing significantly enhances the GMI ratio and η in the nanocrystalline samples with $x = 0$ and 0.1 , but decreases the η in the nanocrystalline samples with $x = 0.025$ and 0.05 . The variations of the GMI ratio and the field-induced magnetic anisotropy field (H_K) upon Fe doping are correlated with the microstructural changes in the nanocrystalline samples. These results have been published in *Journal of Applied Physics*, 2011.

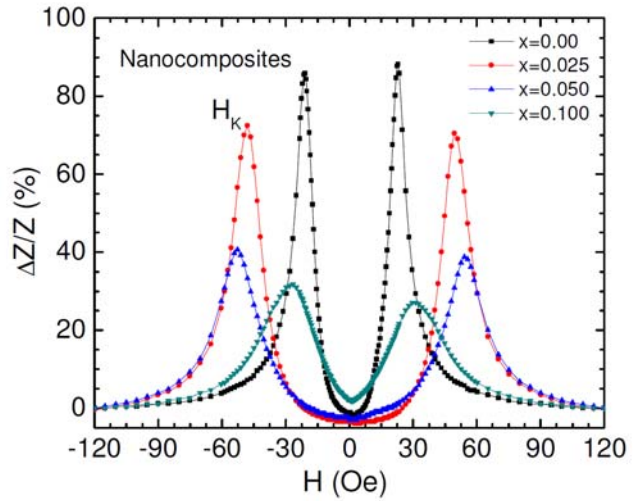


Fig. 16 Magnetic field dependence of GMI ratio ($\Delta Z/Z$) at 0.5 MHz for $(\text{Co}_{1-x}\text{Fe}_x)_{89}\text{Zr}_7\text{B}_4$ ($x = 0, 0.025, 0.05, 0.10$) nanocomposites.

(f) Enhanced GMI Effect and Field Sensitivity in Soft Ferromagnetic Ribbons with Co Coating

Introduction:

Since GMI is observed at high frequencies (> 1 MHz), the skin effect is significant enough to confine the ac current to a sheath close to the surface of the conductor; GMI is therefore a surface-related magnetic phenomenon. As such, the surface roughness of a material is important and can considerably reduce the GMI magnitude if the surface irregularities exceed the skin depth [13]. Here, we have demonstrated that the presence of the Co coating layer enhances both the GMI effect and field sensitivity in the Co-coated ribbons. The largest values of the GMI effect and field sensitivity are achieved in the sample coated with Co on the free ribbon surface having the smaller surface roughness as compared to that coated with Co on the wheel-side ribbon surface with the larger surface roughness. Our findings are therefore of practical importance, demonstrating a way to tailor the GMI effect and field sensitivity in surface-modified ferromagnetic ribbons for use in highly sensitive magnetic sensors.

Experiment:

$\text{Co}_{84.55}\text{Fe}_{4.45}\text{Zr}_7\text{B}_4$ amorphous ribbons with a width of 2 mm and a thickness of 30 μm were prepared by the melt-spinning method. X-ray diffraction confirmed the amorphous nature of the ribbons. The surfaces of the ribbons were then coated with 50 nm-thick Co layers using magnetron sputtering. The surface morphology of the samples was analyzed using atomic force microscopy (AFM). We denote the free surface of the ribbon as that which had no contact with the surface of the copper wheel and the wheel-side ribbon surface as that which had direct contact with the surface of the copper wheel. Magnetic measurements were performed at room temperature using a VSM. Magneto-impedance measurements were conducted along the ribbon axis following the same procedures outline above.

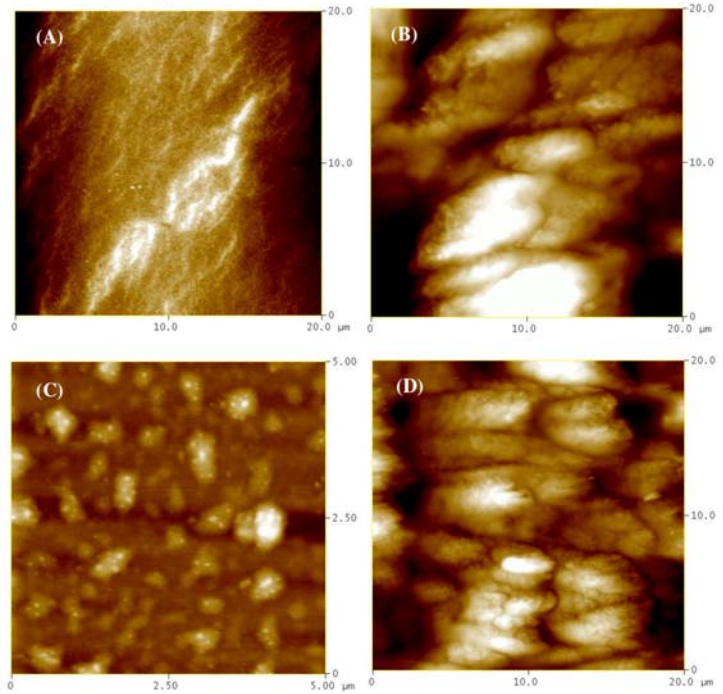


Fig. 17 2D topography images of (a) the free ribbon surface of the uncoated ribbon (Sample #1), (b) the wheel-side surface of the uncoated ribbon (Sample #2), (c) the free ribbon surface of the Co-coated ribbon (Sample #3), and (d) the wheel-side surface of the Co-coated ribbon (Sample #4).

Results and Discussion:

First we studied the surface topography of the uncoated and Co-coated ribbon samples using AFM. **Fig. 17** shows the AFM images of these samples for both surfaces. The AFM image indicates the distribution of protrusions with very high and uniform density for the free surface of the ribbon, unlike in the case of the wheel-side surface of the ribbon. The root mean squared (rms) surface roughness

($R_q = \frac{1}{n} \sqrt{\sum_{i=1}^n z_i^2}$, where z is the average amplitude of the topographical feature) was determined

from the corresponding topographical data of **Fig. 17** to be about 5.6 nm, 147 nm, 3.2 nm, and 61 nm for the free surface of the uncoated ribbon (Sample #1), the wheel-side surface of the uncoated ribbon (Sample #2), the free ribbon surface coated with Co (Sample #3), and the wheel-side ribbon surface coated with Co (Sample #4), respectively. Since Sample #1 and Sample #2 are both uncoated control samples, they have the same magnetic properties and GMI effect; we discuss below the M-H and GMI results of only samples #1, #3, and #4.

Fig. 18a,b shows the dc magnetic field dependence of GMI ratio ($\Delta Z/Z$) for samples #1, #3, and #4 at two representative frequencies $f = 5$ MHz and 10 MHz. The frequency dependence of maximum GMI ratio ($[\Delta Z/Z]_{\max}$) and the maximum field sensitivity of GMI (η_{\max}) of these samples are displayed in **Fig. 18c,d**, respectively. It can be observed in **Fig. 18a,b** that a double-peak structure in GMI profile is present for all samples investigated, with a more pronounced dip at zero field in Samples #3 and #4 than in Sample #1. From a sensor application perspective, it is very interesting to note that in the frequency range of 0.1 to 10 MHz, larger values of $[\Delta Z/Z]_{\max}$ and η_{\max} are achieved in Sample #3 and Sample #4 when compared to Sample #1. At $f = 2$ MHz,

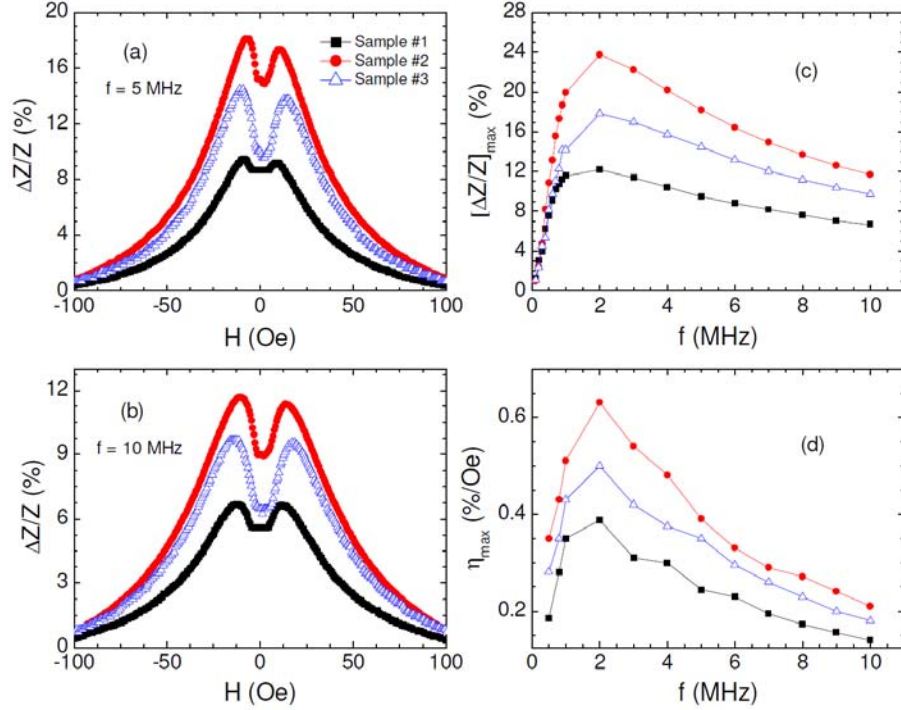


Fig. 18 (a,b) Magnetic field dependence of GMI ratio ($\Delta Z/Z$) at 5 MHz and 10 MHz for Sample #1, Sample #3, and Sample #4; (c,d) Frequency dependence of the maximum GMI ratio ($[\Delta Z/Z]_{\max}$) and the field sensitivity of GMI (η) for these samples.

$[\Delta Z/Z]_{\max}$ and η_{\max} reach the largest values of 12.18% and 0.39%/Oe for Sample #1, 23.71% and 0.74%/Oe for Sample #3, and 17.85% and 0.50%/Oe for Sample #4. This clearly indicates that the Co coating enhances the GMI ratio and field sensitivity. Depositing the Co on the free ribbon surface with the smaller surface roughness ($R_q \sim 6$ nm) results in the larger $[\Delta Z/Z]_{\max}$ and η_{\max} when compared to that on the wheel-side ribbon surface having the larger surface roughness ($R_q \sim 147$ nm). Our studies have shown that the presence of the Co coating layer enhances both the GMI effect and field sensitivity in the Co-coated ribbons, demonstrating a new way to tailor the GMI effect and field sensitivity in surface-modified ferromagnetic ribbons for use in highly sensitive magnetic sensors. These results have been published in *Journal of Applied Physics*, 2011.

(g) Impact of Field-induced Exchange Anisotropy on GMI in Ribbon/FeMn Bilayers

We report how the GMI of a Co-based amorphous ribbon is affected by tuning the surface anisotropy of the ribbon by capping it with an antiferromagnetic material FeMn in the presence of a 200 Oe field applied in the longitudinal or transverse directions. We find that the orientation of the deposition field greatly impacts the GMI of the bilayer structures. Our studies provide further guidance for tailoring GMI in surface modified soft ferromagnetic ribbons as well as optimizing specific frequency ranges for particular sensors.

Experiment:

Cobalt based Metglas® Inc 2705M ribbons of width 2mm and thickness of 30 μm were coated with 150 Å of FeMn by using magnetron sputtering. X-ray diffraction confirmed the amorphous structure of the ribbons pre-deposition. During the deposition, a field of 200 Oe was applied either perpendicular or parallel to the sample length. The samples were also rotated 90 degrees so that the applied DC field was perpendicular to the sample length before impedance measurements were again carried out. Magnetic measurements were performed at room temperature using a VSM. Magneto-impedance measurements were conducted along the ribbon axis.

Results and Discussion:

Fig. 19a,b shows the magnetic field dependence of GMI ratio at a representative frequency of 1 MHz and the maximum GMI ratio as a function of frequency for the plain ribbon, FeMn/ribbon bilayer in an applied transverse field of 200 Oe (conf. 1), and FeMn/ribbon bilayer in an applied longitudinal field of 200 Oe (conf. 2).

As one can see from **Fig. 19a**, the GMI profiles with a double-peak structure have been obtained for all samples investigated. At 1 MHz, the sample with conf. 1 has the largest value of GMI ratio among the three samples. It is very interesting to note in **Fig. 19b** that while the sample with conf. 1 has larger values of GMI ratio compared with those of the plain ribbon in the whole frequency range of 0.1-10 MHz, the sample with conf. 2 possesses smaller values of GMI ratio at $f < 4$ MHz, but larger values of GMI ratio for $f > 4$ MHz. This clearly indicates the important impact of exchange bias on the GMI profile in the FeMn/ribbon bilayer structures.

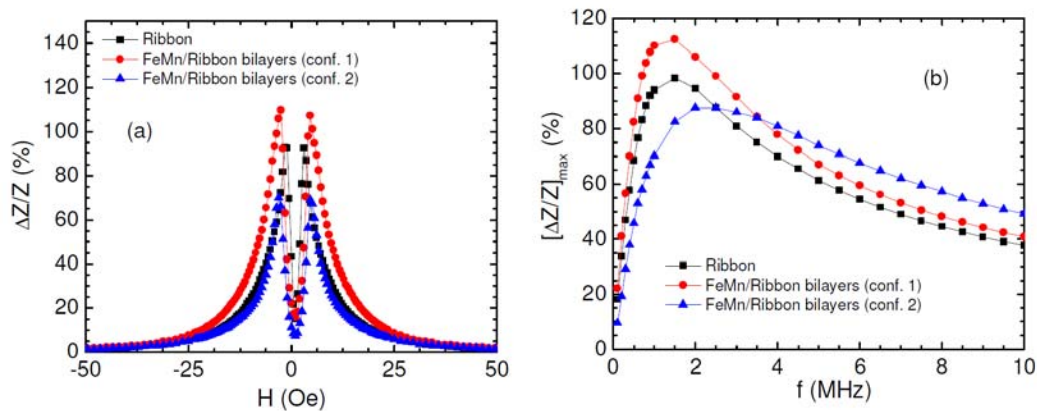


Fig. 19 (a) Magnetic field dependence of GMI ratio and (b) frequency dependence of maximum GMI ratio for the plain ribbon, the FeMn/ribbon bilayer in a transverse magnetic field of 200 Oe and the FeMn/ribbon bilayer in a longitudinal magnetic field of 200 Oe.

To understand the frequency dependence of maximum $\Delta Z/Z$ of the plain ribbon, the FeMn/ribbon bilayer in a transverse magnetic field of 200 Oe and the FeMn/Ribbon bilayer in a longitudinal magnetic field of 200 Oe, we have studied the frequency dependence of maximum $\Delta R/R$ and $\Delta X/X$ ratios for these samples (**Fig. 20**). In the frequency range 0.1 – 10 MHz the $\Delta R/R$ ratio is largest for the FeMn/ribbon bilayer in a transverse magnetic field of 200 Oe (the sample with conf. 1). The $\Delta R/R$ ratio of the FeMn/ribbon bilayer in a longitudinal magnetic field of 200 Oe (the sample with conf. 2) is smaller than that of the plain ribbon. However, the $\Delta X/X$ ratio is largest for the sample with conf. 2 at high frequencies ($f > 1$ MHz). These relative contributions of $\Delta R/R$ and $\Delta X/X$ to $\Delta Z/Z$ allow us to interpret the frequency dependence of maximum $\Delta Z/Z$ in these three samples.

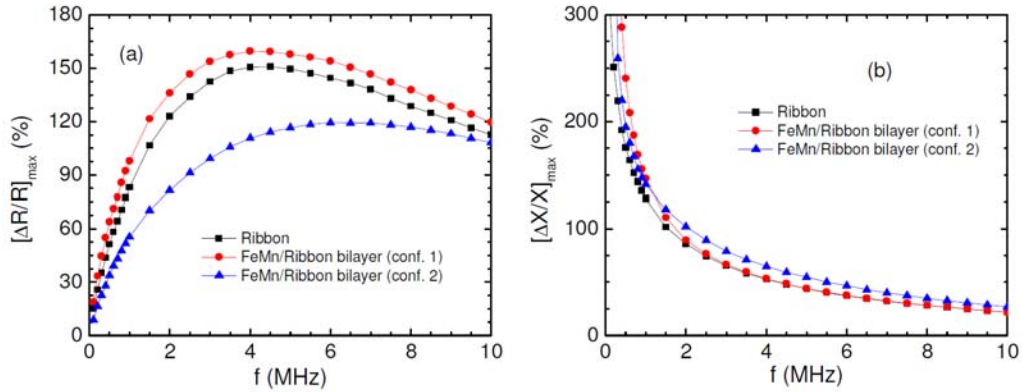


Fig. 20 Frequency dependence of (a) maximum $\Delta R/R$ and (b) $\Delta X/X$ ratios for the plain ribbon, the FeMn/ribbon bilayer in a transverse magnetic field of 200 Oe and the FeMn/ribbon bilayer in a longitudinal magnetic field of 200 Oe.

Overall, we have systematically studied the GMI effect in field grown FeMn/Metglas[®] Inc bilayer structures. Both the FeMn layer and the direction of the field during deposition have a substantial impact on the GMI. Depending on the frequency range and field range desired, we have shown that it is beneficial to use a bilayer structure over a control sample. These improvements could be used for improving the sensitivity and functionality of highly sensitive magnetic sensors.

(h) Carbon Nanotube-based Gas Sensors using The Magneto-impedance Effect

Carbon nanotubes (CNTs) based gas sensors with high sensitivity and selectivity (where sensing is achieved by the DC resistance change upon adsorption of analytic molecules) are critically needed for leakage detections of explosive gases such as hydrogen, and for real-time detections of toxic or pathogenic gases in industries [16]. Due to the extremely high surface-to-volume ratio, CNTs are ideal for gas molecule adsorption and storage. However, these resistive sensors possess limited sensitivities ($\Delta\rho/\rho \sim 2\text{-}10\%$). Therefore it is essential to develop alternative techniques that allow detecting gases with a higher degree of sensitivity. Our studies have shown that detecting field-induced impedance change (known as the GMI effect) in CNTs deposited on magnetic ribbons would be a radically new concept which would lead to developing a new class of gas sensors with improved sensitivity. We present below some of the main results of this research.

Experiment:

Carbon nanotubes were grown in commercial porous alumina templates using the chemical vapor deposition (CVD) method without using metal catalysts. The alumina templates were etched away leaving free standing CNTs. The resulting CNTs were between 250 and 300 nm in diameter on average (see inset of **Fig. 21**). The CNTs were then drop-casted onto a Metglas ® 2714A ribbon before measuring GMI. Three different concentrations were used and compared to a plain ribbon with no CNTs. Magneto-impedance measurements were conducted along the ribbon axis in dc magnetic fields up to 120 Oe over a frequency range of 0.1 ~ 10 MHz with a constant ac current of 5 mA.

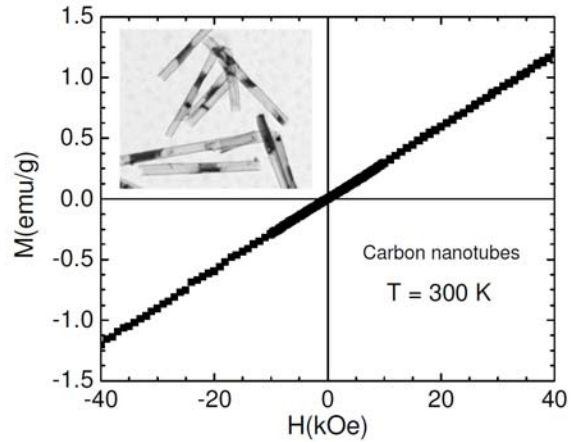


Fig. 21 M-H loop of CNTs at 300 K. In inset: TEM of CNTs synthesized using CVD.

Results and Discussion:

Figure 22 shows that the presence of CNTs increased the $\Delta Z/Z$ ratio in the case of the sample with CNTs. The $\Delta Z/Z$ ratio increased from 34% for the ribbon to 40% for the ribbon with CNTs. With increasing CNT concentration, the $\Delta Z/Z$ ratio first increased, reached a maximum, and decreased as the CNT concentration was saturated. Interestingly, the large $\Delta Z/Z$ ratio was achieved only high frequencies ($f > 1$ MHz), where the skin effect is strong and the surface effect becomes important.

To elucidate this further, we measured the M-H loop of CNTs at 300 K and the result obtained is shown in **Fig. 21**. It is evident that CNTs showed a paramagnetic behavior. Therefore, the physical mechanism leading to the observed increase of the $\Delta Z/Z$ ratio in the ribbons with CNTs must be different from what has been proposed for the case of supermagnetic nanoparticles. To elucidate this, we have investigated the influence of CNTs on the electrical resistance R and reactance X response ($Z = R + jX$). **Figure 23(a-c)** shows the magnetic field dependence

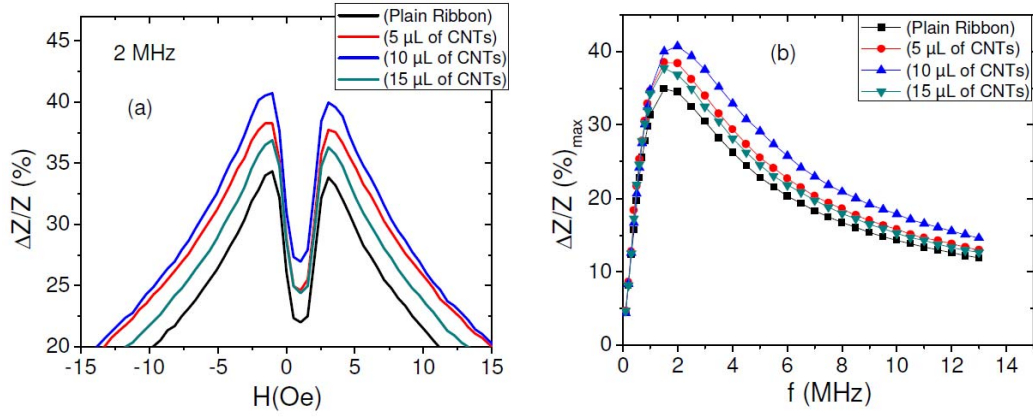


Fig. 22 (a) GMI profiles at 2 MHz for the magnetic ribbon with and without CNTs and (b) Frequency dependence of maximum GMI ratio for these samples.

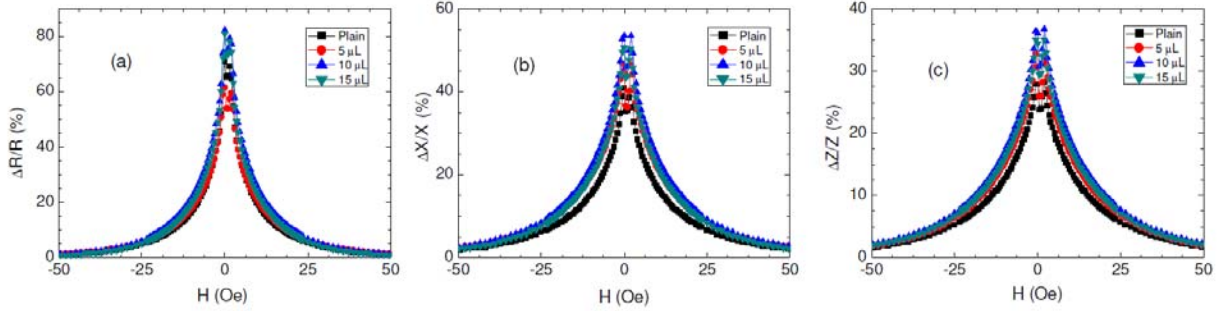


Fig. 23 Magnetic field dependence of $\Delta R/R$, $\Delta X/X$ and $\Delta Z/Z$ ratios taken at 5 MHz for the ribbon with and without CNTs.

of $\Delta R/R$, $\Delta X/X$, and $\Delta Z/Z$ ratios for all the samples at $f = 5$ MHz. At this frequency both $\Delta R/R$ and $\Delta X/X$ are larger for the ribbon coated with CNTs. The double-peak feature significantly varied at low magnetic fields in the samples with CNTs. This pointed to the important fact the presence of CNTs could compensate stray fields due to surface irregularities that are present on the surface of the ribbon and consequently increased the GMI effect. The relative contributions of $\Delta R/R$ and $\Delta X/X$ to $\Delta Z/Z$ are different in the investigated frequency range 0.1 – 10 MHz.

As shown in **Fig. 24a,b**, the presence of CNTs strongly changed $\Delta X/X$ in the low frequency range ($f < 3$ MHz) and $\Delta R/R$ in the high frequency range ($f > 3$ MHz). These findings provide important clues towards a complete understanding of the enhanced GMI effect in the ribbons coated with CNTs. From a practical application perspective, it is very interesting to note that the $\Delta R/R$ ratio (the magnetic field-induced AC resistance change) increases up to 35% for the ribbon coated with CNTs with respect to the plain ribbon. This reveals the new possibility of developing CNT-based gas sensors operating based on the principle of the MI effect with higher field sensitivity compared with current state-of-the-art sensors based on the DC resistance change. Our plans are to investigate the effect of CNTs filled with magnetic nanoparticles on the

GMI for possible applications in nanomedicine. A manuscript has been submitted for publication in *Journal of Applied Physics*, 2011.

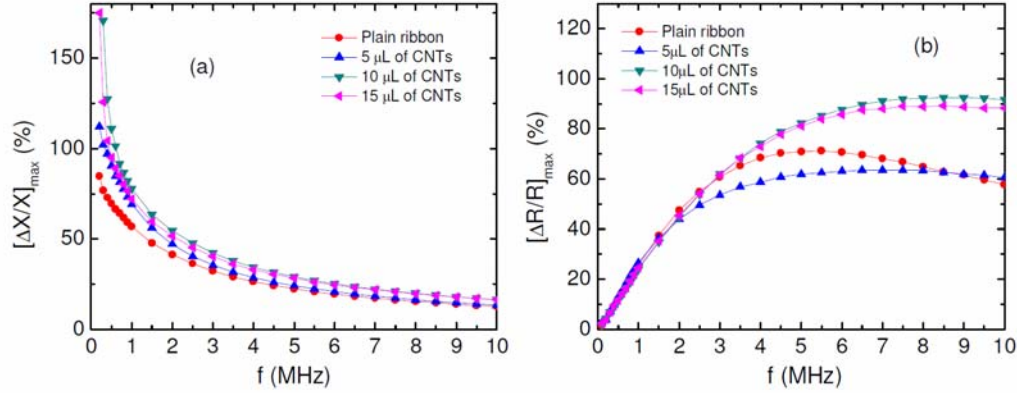


Fig. 24 (a) Frequency dependence of (a) maximum $\Delta X/X$ and (b) $\Delta R/R$ ratios for the magnetic ribbon with and without CNTs.

(i) Detecting Magnetic Nanoparticles-Functionalized Biomolecules with GMI Biosensors

While GMI effect has long been explored for high performance sensor applications [13], it has recently been developed as a highly sensitive biosensor for biomolecular detection [18]. The goal of our research is to investigate the mechanisms of sensing magnetic nanoparticles at different concentrations, size, magnetic moments distributions of the particles, signal-to-noise ratio as a function of an active sensor area, temperature, and to check the ability of binding affinity measurements in living systems starting in the beginning with synthetic bioreceptors as a model system. We present here some representative results of a detailed study of the influences of different concentrations of magnetic nanoparticles on the GMI effect of the Co-based ribbon.

Experiment:

Fe_3O_4 nanoparticles with different concentrations were deposited on Co-based magnetic ribbons in a controllable fashion so that the number of the deposited nanoparticles (corresponding to the number of the functionalized cells) could be detected through the change in GMI of the ribbon. Different concentrations of Fe_3O_4 nanoparticles were also dispersed in a polymer matrix. Magneto-impedance measurements were conducted along the ribbon axis in dc magnetic fields up to 120 Oe over a frequency range of 0.1 ~ 10 MHz with a constant ac current of 5 mA.

Results and Discussion:

Fig. 25 shows the magnetic field dependence of GMI ratio and the frequency dependence of maximum GMI ratio for the cases with and without Fe_3O_4 nanoparticles. It is shown that the presence of Fe_3O_4 nanoparticles increases the GMI effect in the ribbon and the GMI effect increases with increasing the concentration of the nanoparticles. It is worth mentioning that there is a significant difference in GMI only at high frequencies above 1 MHz, where the skin effect is strong and the ribbon surface is very sensitive to magnetic signals of Fe_3O_4 nanoparticles. We believe that in this frequency range, the movement of magnetic domain walls in the ribbon is strongly damped, and the magnetization process is purely caused by rotation of magnetic

moments. The application of a dc magnetic field could align simultaneously the magnetic moments of the magnetic nanoparticles and the magnetic ribbon in the dc magnetic field direction, leading to an overall enhancement of the GMI effect. In addition, the difference in GMI is mainly observed at low magnetic fields. These findings are of practical importance in selecting the optimal working conditions (magnetic field and frequency) for GMI biosensors.

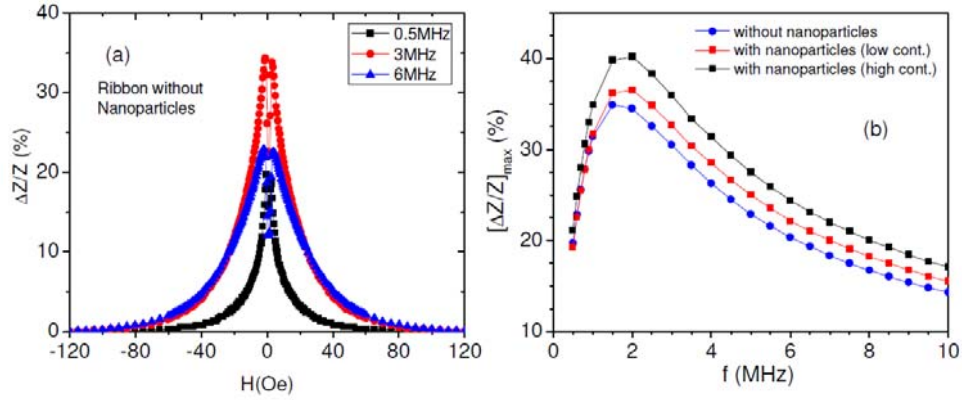


Fig. 25 (a) GMI profiles at different frequencies for the plain ribbon and (b) Frequency dependence of maximum GMI ratio and the inset shows GMI profiles at 2 MHz for the ribbons with and without 9 nm Fe_3O_4 nanoparticles with different concentrations (5 μL and 15 μL).

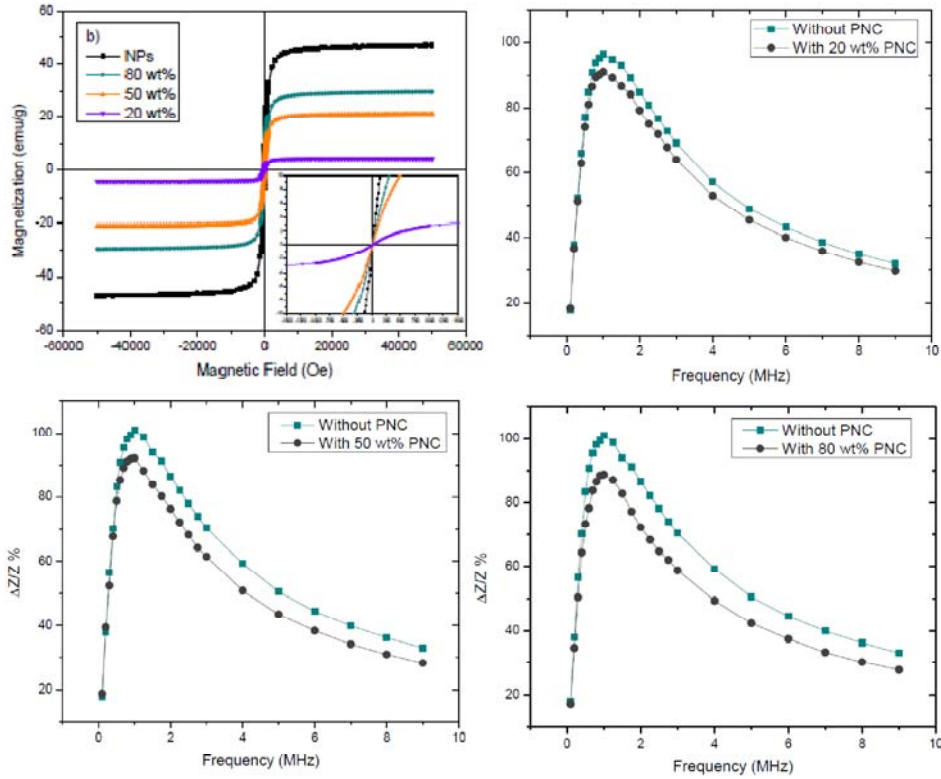


Fig. 26 GMI results with and without PNC layered on top for a) 20 wt% PNC, b) 50 wt% PNC, and c) 80 wt% PNC.

Figure 26 shows the M-H and GMI data of the Fe_3O_4 nanoparticles and the polymer nanocomposite (PNC) samples with different concentrations of the nanoparticles. It can be observed that the difference in GMI between the ribbon with PNC and without PNC increased with increasing concentrations of NPs. For the 20, 50, and 80 wt% PNCs, there is an approximate 5% decrease in GMI with the 20 wt% PNC, an approximate 9% decrease in GMI with the 50 wt% PNC, and an approximate 13% decrease in GMI with the 80 wt% PNC. To find out what caused the change in impedance, the data was broken down into separate graphs of resistance and reactance. We have found the change in impedance came from a change in resistance which has to do with the electrical properties of the PNC. The reactance, which has to do with the magnetic properties of the PNC, does not change noticeably. One possible explanation is that the PNCs are conductive, so adding another path for the current to flow through reduces the total resistance. However, when the PNCs were tested for electrical conductivity, none of the composites were found to be conductive.

Overall, the high sensitivity of the GMI signal with magnetic nanoparticles demonstrates the possibility of sensing magnetic nanoparticle-functionalized biomolecules. We are investigating the influences of different nanoparticles (Fe_3O_4 , CoFe_2O_4 , and NiFe_2O_4) and particle size and shape on the GMI effect of the Co-based ribbon. We are also in process of developing the GMI technology to detect the presence of cancer cells loaded with different types of the magnetic nanoparticles. Since the GMI of the ribbon changed when different percent loadings of PNC were layered on top, we conclude that GMI is indeed sensitive to the presence of NPs, and therefore could be used in bio-sensing applications. Further work is in progress to determine what caused the change in impedance, specifically why the resistance of the sample changed with the presence of a PNC while the reactance did not, and how the distance between the ribbon and the nanoparticles affects the GMI.

(j) Synthesis and characterization of $\text{La}_{0.5}\text{Sr}_{0.5}\text{MnO}_3$ nanowires for sensor applications

Class of manganese oxide compounds $\text{R}_{1-x}\text{A}_x\text{MnO}_3$ (R= trivalent rare earth, A= divalent alkaline earth) are interesting to study because of the structural, magnetic and electrical properties are closely inter-related. These materials exhibit the so-called colossal magneto-resistive (CMR) and magneto-caloric effect (MCE), which form the bases for developing magnetic sensor and energy-efficient refrigeration devices [18,19]. We have conducted the first studies of the impact of nanostructuring on the magnetism, CMR and MCE in the half-doped $\text{La}_{0.5}\text{Sr}_{0.5}\text{MnO}_3$ manganite. Our preliminary results have revealed that the properties of the $\text{La}_{0.5}\text{Sr}_{0.5}\text{MnO}_3$ nanowires are largely different from their bulk counterpart. These nanowires can be attractive candidates for developing multifunctional sensors. A graduate student, Mr. Sayan Chandra, has primarily worked on this system. Some of the results are reported below.

Experiment:

The hydrothermal synthesis of $\text{La}_{0.5}\text{Sr}_{0.5}\text{MnO}_3$ was done using a hydrothermal synthesis technique as follows. High purity KMnO_4 , $\text{MnCl}_2 \cdot 4\text{H}_2\text{O}$, $\text{La}(\text{NO}_3)_3 \cdot x\text{H}_2\text{O}$ and $\text{Sr}(\text{NO}_3)_2$ were used as the starting materials, and KOH served as mineralizer. The reaction reagents were dissolved in deionized water maintaining the initial mole ratios of 0.6 KMnO_4 :1.4 $\text{MnCl}_2 \cdot 4\text{H}_2\text{O}$:1.0 $\text{La}(\text{NO}_3)_3 \cdot x\text{H}_2\text{O}$:1.0 $\text{Sr}(\text{NO}_3)_2$: 400 H_2O :70 KOH. The reaction mixture was magnetically stirred for 3-4 hours and poured into a Teflon vessel till 80% of its volume was filled. The hydrothermal treatment was performed at 270°C for 30 hours. The autoclave was

cooled and depressurized to obtain the black precipitate which was washed with deionized water to remove alkalinity from the sample. It was then dried overnight on a hot plate to obtain a black powder. The prepared sample was characterized using XRD, TEM, high resolution TEM (HRTEM) and scanning electron microscopy (SEM). The structural phase determination was done using an X'PertPRO PANalytical x-ray diffractometer using a Cu K α source. The size and shape of the nanowires was characterized using a FEI QUANTA 200 scanning electron microscope and Tecnai TF 20 ST HRTEM. Standard magnetic measurements such as the temperature dependence of zero-field cooled (ZFC) and field cooled curves (FC), M-H hysteresis measurements were performed using a Quantum Design MPMS XL squid from central facility at DAE-UGC.

Results and discussion

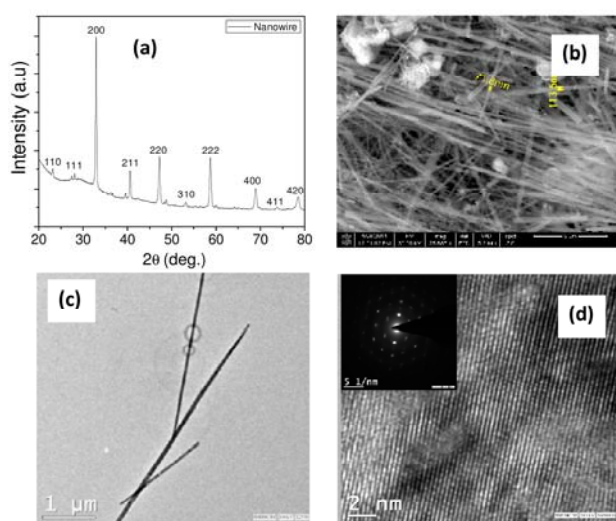


Fig. 27 XRD, SEM, TEM of the LSMO nanowire. The inset of Fig. 27d shows electron diffraction pattern.

Figure 27a shows the XRD pattern of the nanowire sample. Relative to the bulk form, identical peaks were also observed for the nanowires thus confirming the formation of a cubic perovskite structure. **Figure 27b,c** displays SEM image and EDS of the as synthesized nanowires. The nanowires were found to have a length distribution from 1 to 10 μm and diameter ranging from 50 to 300 nm. EDS confirmed the elemental purity of both samples. Each nanowire had uniform diameter along its entire length. We found some other structures that were formed along with the nanowires, but in negligibly small quantities. The formation of other structures could be due to the variation of pressure within the hydrothermal cell. HRTEM images at 200 kV were taken after the powder sample was sonicated and then

dispersed on a Cu grid. **Figure 27** shows the dispersed nanowires on the left and lattice fringes on the right. The inset shows the electron diffraction pattern which suggests the polycrystalline nature of the nanowires. The HRTEM images reveal that surface of the nanowires are clean without any sheathed amorphous phase.

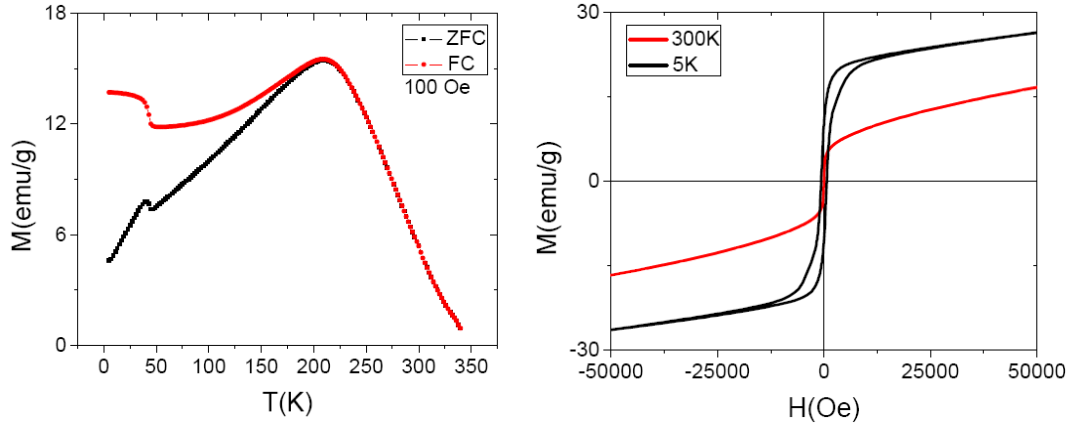


Fig. 28 (Right panel) magnetization vs. temperature (ZFC/FC) curves and (Left panel) magnetization vs. dc field curves for the nanowire sample at 5K and 300K.

The M-H curves taken at 300K and 5K indicate that the nanowires are ferromagnetic up to 300 K. It is worth noting that the magnetic moments remain unsaturated even at high fields of 5T (Figure 28). The coercive field at 300 K was less than 5 Oe which falls within the field increment step of the measurement and the coercivity at 5K is 650 Oe. The M-T measurement for the ZFC and FC cases was performed at applied fields of 100 Oe in the temperature range 5K to 310K. The Curie temperature (T_c) was found to be above room temperature. As the temperature was decreased below the T_c , the magnetization was found to increase until 220 K for the measurement field of 100 Oe and then it decreased which can be attributed to the spin freezing in the material. A jump was observed in the ZFC/FC curves for the 100 Oe data at 40K, which may be due to the spin canting.

In this project, $\text{La}_{0.5}\text{Sr}_{0.5}\text{MnO}_3$ nanowires were successfully synthesized using the hydrothermal technique. The synthesized nanowires were several microns long and had a width variation of 50nm to 300 nm. Magnetic measurements indicated ferromagnetism at room temperature. Spin freezing ($\sim 220\text{K}$) and spin canting ($\sim 40\text{K}$) was observed from the M-T curves. We are in process of investigating the magneto-transport properties, CMR and MCE in these nanowires. The temperature and field dependences of effective magnetic anisotropy of the nanowires will be studied by our radio-frequency transverse susceptibility.

(k) Functional Materials for Affecting Cell Proliferation and Locomotion

Polyelectrolyte multilayer films are of interest in fundamental research and technology development [20-23]. Applications of these films include optical coatings, coatings for cell patterning, drug delivery vehicle coatings and various other film technologies[22-28]. The use of polyelectrolytes to fabricate functional nano-composite coatings has attracted considerable attention worldwide [20-23,29-31].

Here, we report results of an initial test of a buildup hypothesis on which exponential growth involves the formation of dendritic structures on the film surface. The number of polymer binding sites will increase in successive adsorption steps on this view because the number of incompletely charge-compensated polyelectrolyte molecules increases, giving an exponential rise in the amount of material deposited, at least in the range where such growth

occur; growth may become linear after some number of layers are deposited. Peptides were adopted as model polymers. Dendrimeric forms of poly(L-lysine) (PLL) were designed and synthesized, and multilayer films of these species and poly(L-glutamic acid) (PLGA) were made. The dendrimeric PLL molecules had 4 or 8 branches, each having a nominal degree of polymerization (DP) of 30. Ultraviolet spectroscopy (UVS) and circular dichroism spectroscopy (CD) were utilized to monitor film buildup and polymer structure in films, quartz crystal microbalance (QCM) to measure mass deposited and atomic force microscopy (AFM) to characterize film surface morphology and roughness. Taken together, the data from different methods form a consistent perspective.

UVS. In usual cases, the intrinsic chromophores in peptides that make the largest net contribution to absorbance in the 190-320 nm range are peptide bonds, which have a peak maximum near 200 nm. Figure 29 displays representative spectra of 20-layer films made of the polymeric species indicated in Table 1. The systems studied were 4-K₃₀/PLGA-L, 4-K₃₀/PLGA-M, 4-K₃₀/PLGA-S, 8-K₃₀/PLGA-L, 8-K₃₀/PLGA-M and 8-K₃₀/PLGA-S, where in each case the polycation is given first. For instance, 4-K₃₀/PLGA-L signifies the film system consisting of 4-branched, 30-residue PLL and “large” PLGA. As expected, all six systems showed a maximum absorbance near 200 nm. Films built with 8-branched PLL consistently displayed greater absorbance than the respective 4-branched PLL films in the 190-240 nm range in multiple trials involving the same peptide species. A representative spectrum of PLL-M/PLGA-L, in which both polymers were linear, is shown for comparison.

Changes in photon absorption can be used to monitor film buildup and study its character. In the present work, film growth rate correlated with the number of branches in the cationic dendrimeric polymers and, as expected, the DP of the anionic linear polymers. Figure 32 focuses on film absorbance at 217 nm. This wavelength approximates the location of an extremum in the corresponding CD spectra (presented below). Least-squares regression showed that the UV signal grew approximately exponentially during film buildup in each case. Fits to data points for films containing dendrimeric peptides are shown as solid lines. For comparison, buildup data for all-linear polymer systems are shown as broken lines; the values are from the same spectra as the data in Figure 29A of ref. 32. Cationic dendrimers having 8 branches yielded more rapid film buildup than dendrimers having 4 branches.

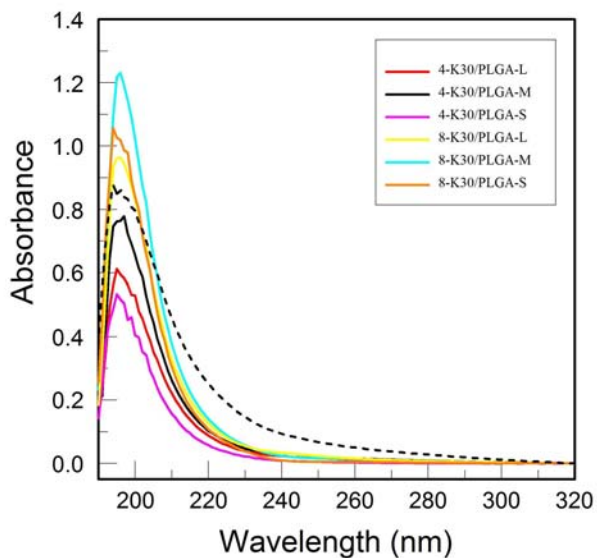


Fig. 29. UVS spectra of hydrated 20-layer films. Overlaid spectra after baseline subtraction are shown. Dashed line, PLL-M/PLGA-L.

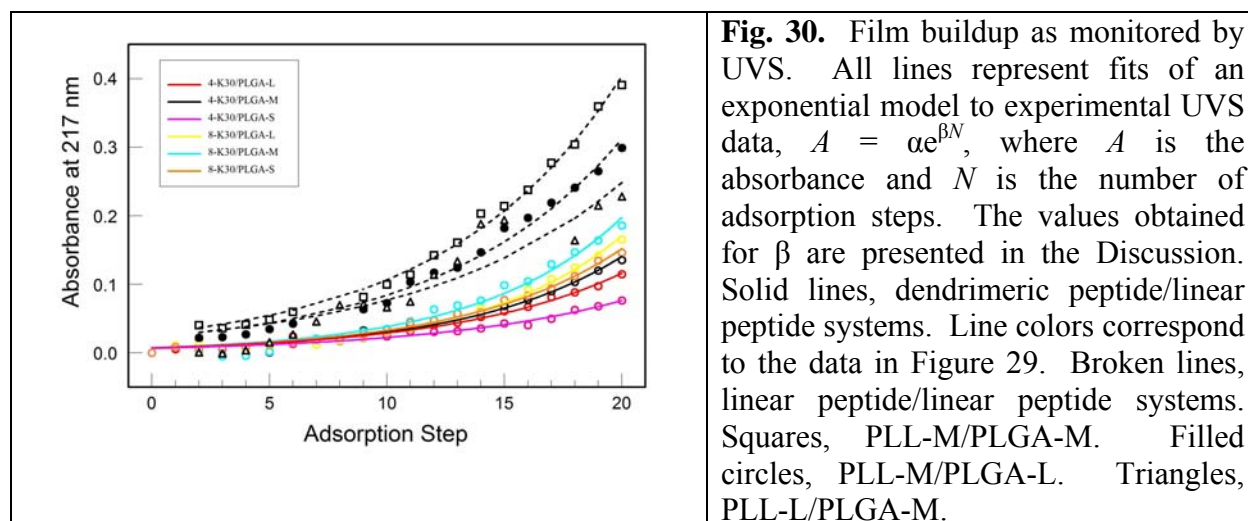


Fig. 30. Film buildup as monitored by UVS. All lines represent fits of an exponential model to experimental UVS data, $A = \alpha e^{\beta N}$, where A is the absorbance and N is the number of adsorption steps. The values obtained for β are presented in the Discussion. Solid lines, dendrimeric peptide/linear peptide systems. Line colors correspond to the data in Figure 29. Broken lines, linear peptide/linear peptide systems. Squares, PLL-M/PLGA-M. Filled circles, PLL-M/PLGA-L. Triangles, PLL-L/PLGA-M.

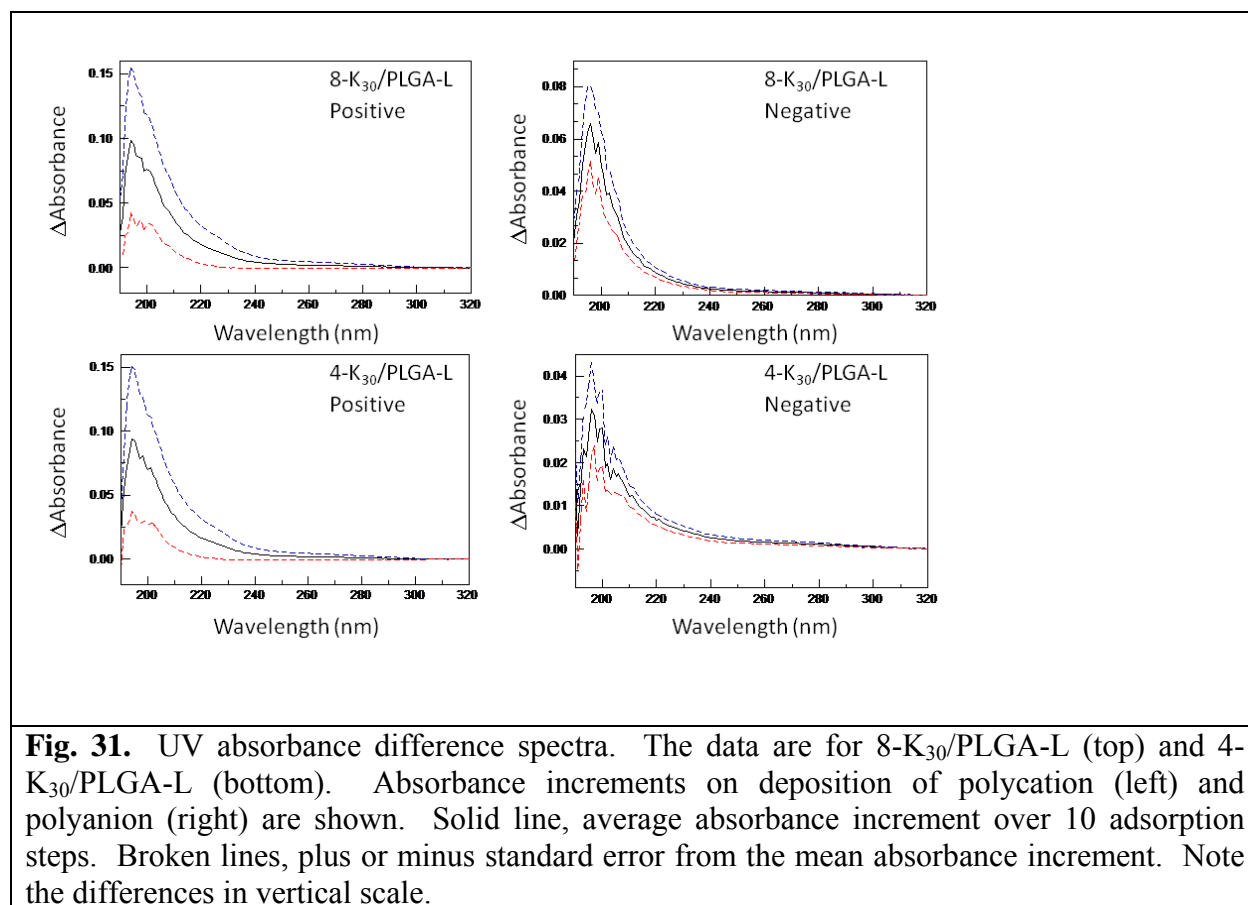


Fig. 31. UV absorbance difference spectra. The data are for 8-K₃₀/PLGA-L (top) and 4-K₃₀/PLGA-L (bottom). Absorbance increments on deposition of polycation (left) and polyanion (right) are shown. Solid line, average absorbance increment over 10 adsorption steps. Broken lines, plus or minus standard error from the mean absorbance increment. Note the differences in vertical scale.

The contributions of polycations and polyanions to film buildup are compared in Figure 31 and in Figures S1-S3 in Supporting Information. In the case of 8-K₃₀/PLGA-L, for example (Figure 32), the spectral maximum in the average optical density increment for dendritic polycation adsorption was 0.10 ± 0.05 , whereas for linear polyanion adsorption the same quantity was 0.065 ± 0.015 , more than 30% smaller. The trend was similar for 4-K₃₀/PLGA-L (0.09 ± 0.06 and 0.032 ± 0.02 , respectively; Figure 32), though the optical density increment was nearly 60% smaller for the polyanion relative to the polycation. The polycation increment was about the same for 8-K₃₀/PLGA-L and 4-K₃₀/PLGA-L, but the polyanion increment was 2-fold greater for the 8-branched than the 4-branched system. The data corroborate what is already apparent from Figure 30: the 8-K₃₀ films grew fastest.

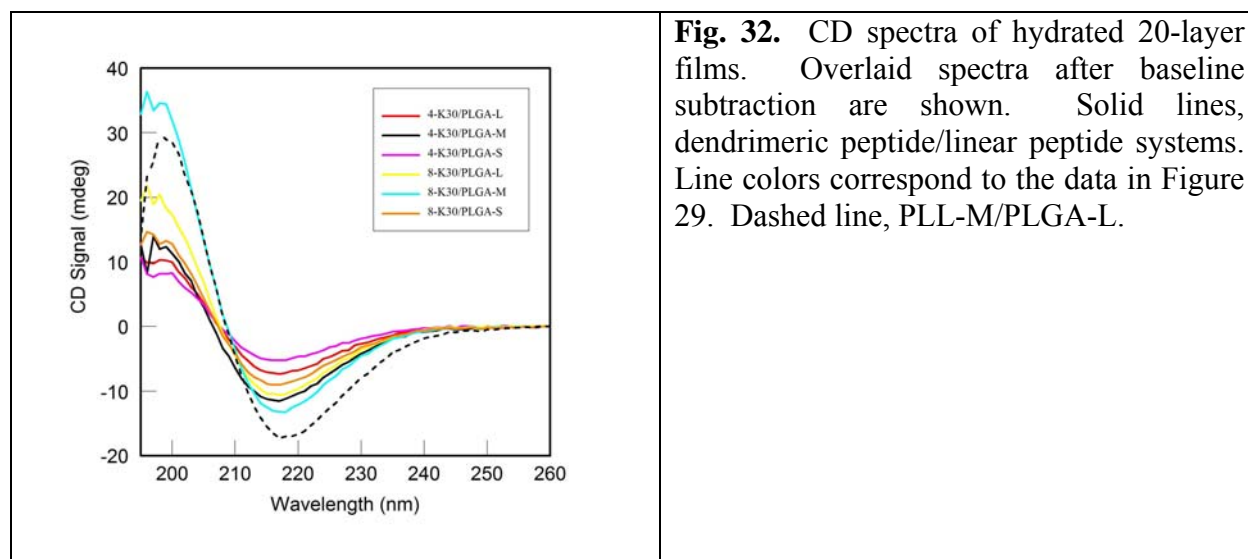


Fig. 32. CD spectra of hydrated 20-layer films. Overlaid spectra after baseline subtraction are shown. Solid lines, dendrimeric peptide/linear peptide systems. Line colors correspond to the data in Figure 29. Dashed line, PLL-M/PLGA-L.

CD. The difference in absorption of right- and left-circularly polarized light is measured, and the shape of the spectrum of a peptide in the far UV can provide information on the average backbone conformation. The film spectra of present study (Figure 32) suggest the same conclusion as the UVS data presented above: The 8-branched system grew faster than the 4-branched. The greater the UV absorbance at 217 nm, the greater the amplitude of the CD signal at the same wavelength. The shape of the CD spectra of films containing dendrimers resembles that of PLL-M/PLGA-M, also shown in Figure 32.

The spectral minimum ranged from 216 nm for 4-K₃₀/PLGA-S to 218 nm for 8-K₃₀/PLGA-M; it was 217 nm for PLL-M/PLGA-M. The various spectra cross the horizontal axis near 208 nm, though at somewhat different points. This suggests that the average polymer backbone conformation was basically the same in all films but that the average conformation varied slightly with film architecture or thickness. Corresponding spectral differences are evident in the UV absorbance data (Figure 29). The signal shape throughout the far-UV range, and particularly the broad band with a minimum near 217 nm, reflects a large percentage of residues in a β sheet conformation, as found in previous studies by Fourier-transform infrared spectroscopy and CD [33-38]. “Random coil” peptides in solution, by contrast, show a deep minimum near 200 nm [39]. It seems likely that the thinner films of the present study had a larger percentage of residues in an irregular conformation than did the thicker films, possibly due to a greater influence of the substrate surface on polymer behavior.

QCM. Utilized to determine the amount of material deposited during or after an adsorption process, QCM is a common method of monitoring multilayer film buildup and, in special cases, measuring viscoelastic properties of deposited materials [39, 40-44]. In the present study, film resonant frequency increment was measured at selected points during buildup. The cumulative frequency shift was to our surprise less than 5 Hz for all six dendrimeric film systems; very little material became deposited at any point in the process (see Figure 33A). Essentially the same results were obtained on repeating the QCM buildup assay with the same peptides but different

solutions. A positive control experiment, by contrast, carried out with different polycations but otherwise under identical conditions, yielded clear evidence of film buildup (see Figure 33B).

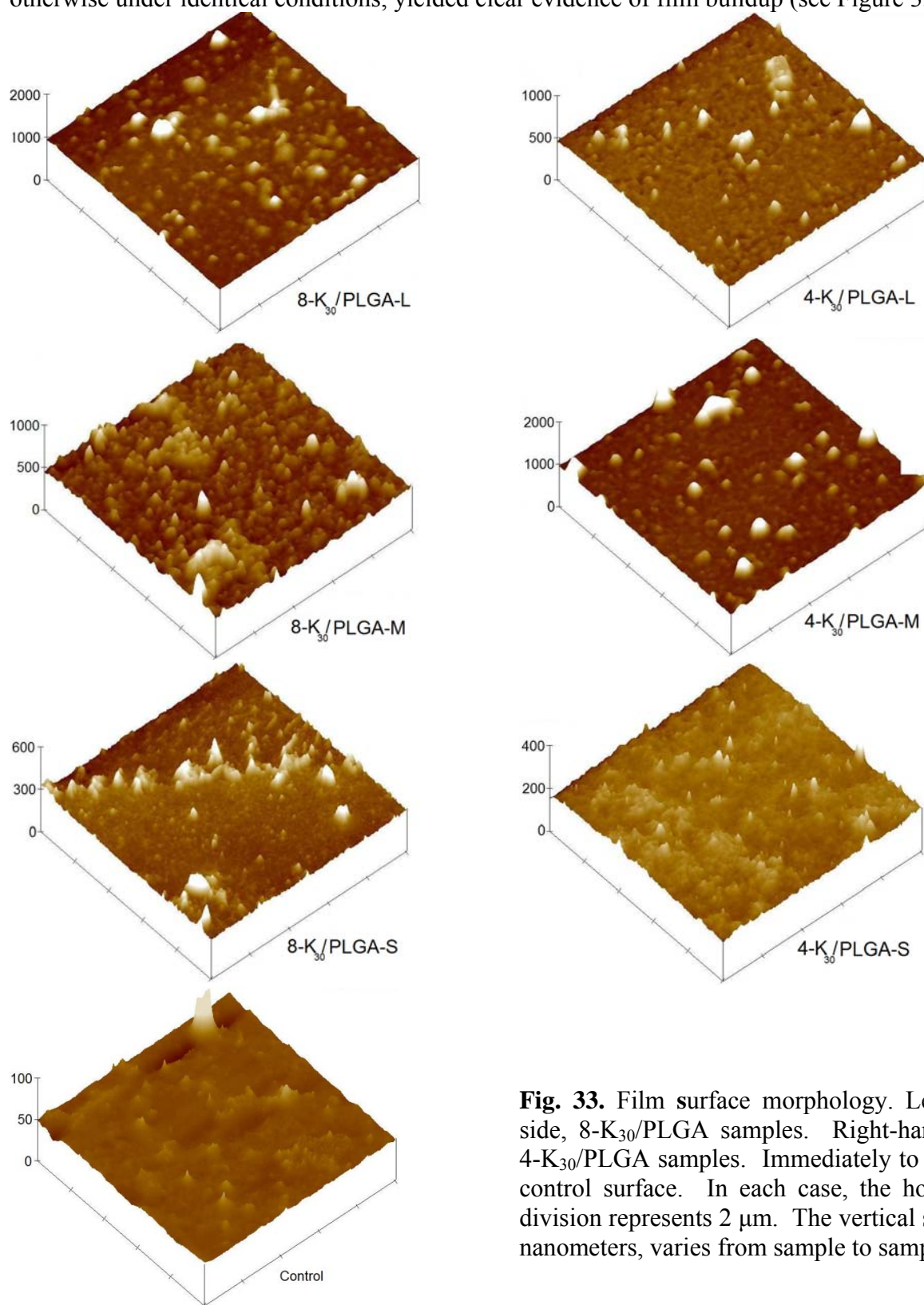


Fig. 33. Film surface morphology. Left-hand side, 8-K₃₀/PLGA samples. Right-hand side, 4-K₃₀/PLGA samples. Immediately to the left, control surface. In each case, the horizontal division represents 2 μm. The vertical scale, in nanometers, varies from sample to sample.

AFM. AFM can provide detailed information on the surface topography of a material. In the present study, height measurements were made for all six dendrimer-containing film systems following dehydration (Figure 35). Note that the z-scale varies from image to image. Surface roughness and the apparent surface feature size tended to be greater for the 8-K₃₀ than the 4-K₃₀ films. For instance, the z-scale is twice as great for 8-K₃₀/L as 4-K₃₀/L, and the lateral dimensions of the surface features are larger. All film samples were considerably thicker and rougher than the cleaned but otherwise unmodified surface (control). Quantitative analysis of the AFM data is provided in the Discussion.

Data consistency. The multilayer systems of this study have been analyzed by UVS, CD, QCM and AFM. All aspects of the determined behavior of these polymer systems were basically reproducible. Key data points for the results presented in Figures 29-33 are tabulated in Table 1. Graphical comparisons of the data sets are shown in Figure 34. It is evident that RMS surface roughness, CD signal at 217 nm and the fitting parameter β from UV analysis showed similar trends with respect to 8-branched versus 4-branched systems.

Table 1. Summary of the results of UVS, CD and AFM experiments for 20-layer films						
Number of K ₃₀ branches	DP of PLGA		UV absorbance at 217 nm $\times 10^{-1}$	β [(layers) ⁻¹] $\times 10^{-1}$	-CD signal at 217 nm (mdeg)	RMS surface roughness (nm)
4	L	330-660	1.14	1.4	7.3	6.1
	M	99-330	1.3	1.5	11.5	9.5
	S	20-99	0.76	1.2	5.2	5.2
8	L	330-660	1.7	1.7	11	13
	M	99-330	1.9	1.7	13	20
	S	20-99	1.5	1.5	9.0	4.4
Control	N/A	N/A	0	0	0	0.5

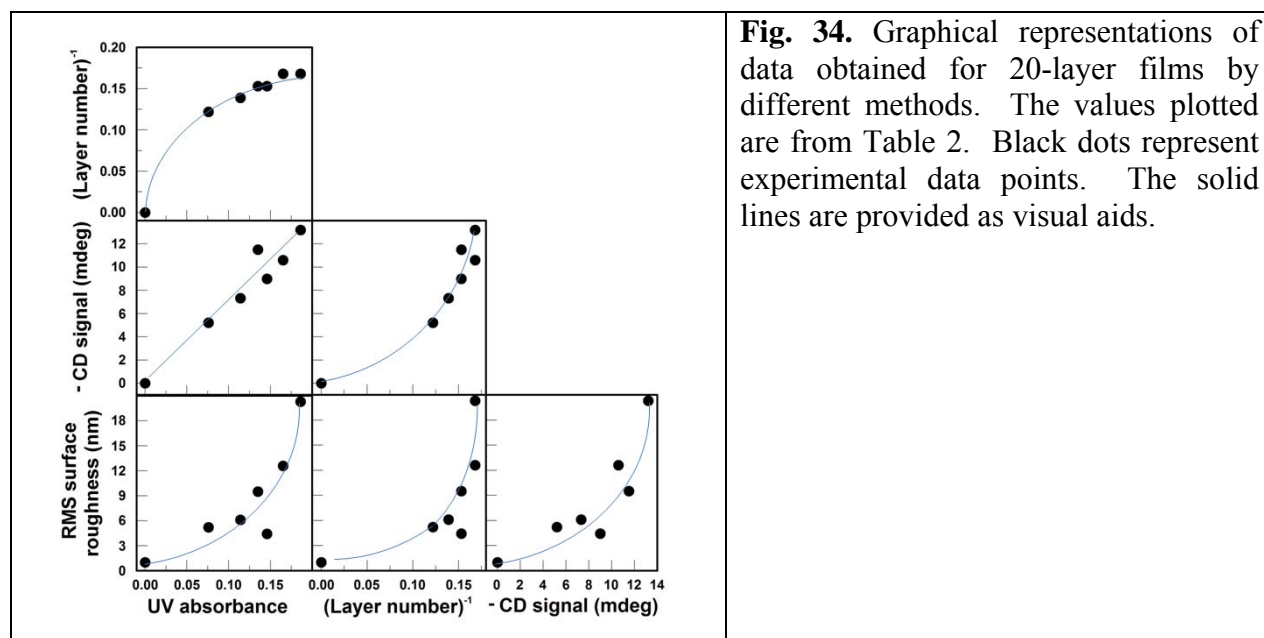


Fig. 34. Graphical representations of data obtained for 20-layer films by different methods. The values plotted are from Table 2. Black dots represent experimental data points. The solid lines are provided as visual aids.

Conclusions: Polyelectrolyte nanofilms made of different dendrimeric poly(L-lysine) molecules and linear poly(L-glutamic acid) molecules of different DP have been studied by CD, UVS, QCM and AFM. 8-branched films grew faster than 4-branched films. Buildup rate correlated with the number of branches. Twice as much linear polyanion became deposited when the dendrimeric species had 8 versus 4 branches. Increased material deposited correlated with increased film surface roughness. Peptides in all films tended to adopt a β sheet conformation. Several film buildup models, including the “dendritic model”, agree with the experimental results. Further analysis of dendrimeric polymers may provide insight into the mechanism of film buildup for linear polyelectrolyte systems.

Research plans: *Nanostructured materials for clinical applications (to be conducted in 2011-2012)*

Magnetic nanoparticles (Fe_3O_4 , $\gamma\text{-Fe}_2\text{O}_3$, core/shell $\text{Fe}/\text{Fe}_2\text{O}_3$, Fe-Co and soft ferrites) are technologically important materials for sensor and biomedical applications. A shape and size controlled synthesis of monodisperse nanoparticles with good magnetic properties has always been a great challenge to the materials scientist. Here we plan to use our newly setup for the chemically synthesize these nanoparticles by thermally decomposing organometallic compounds at high temperature. This technique has been well proven to control particle size and shape by varying reaction parameters like temperature, precursor and surfactant concentrations and refluxing time, and etc. [45,46]. Dr. Hafsa Khurshid, who has just been hired as a postdoctoral researcher, will directly work on this project.

Synthesis of magnetic nanoparticles

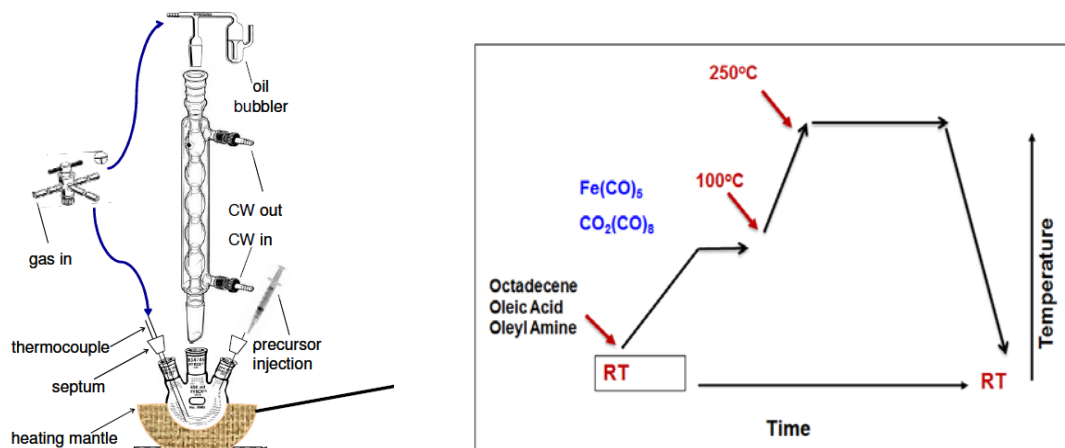


Fig. 35 Schematic view of the system that would be used for chemical synthesis (left) and reaction route (right).

Nanoparticles synthesis will be performed using oleic acid (OA), oleylamine (OY) and Octadecene as surfactants and solvents in a three neck flask. Iron, Co precursors (metallic carbonyls and acacs) would be injected at higher temperature under vigorous stirring and the solution will be refluxed at high temperature for subsequent amount of time. The dark nanoparticles solution will be precipitated by the addition of absolute ethanol and separate by a rare earth laboratory magnet and dispersed in hexane (Figure 35). Being coated with organic surfactants, these particles will be dispersible only in organic solvents. The water dispersibility will be achieved by ligand exchange using PEGylated-phospholipids (PEG: polyethylene glycol). A commercial phospholipid, DSPE-PEG(2000)

Biotin, will be applied to interact with the original OA/OY surfactant layer of nanoparticles to give a robust double layer structure. Such biotinylated nanoparticles have biotin-functionalized surface and are suitable for streptavidin/avidin attachment through the well known specific binding of biotin-avidin.

Relaxometry Studies (MRI):

Relaxometry measurement of the transverse relaxation (T_2) and longitudinal (T_1) relaxation rates using these nanoparticles solution will be done with collaborations to Dr. Mohapatra's group at Moffit Cancer Centre at University of south Florida using 3 T clinical MRI scanners.

Magnetic Fluid Hyperthermia:

Magnetic fluid hyperthermia involves the localized heating of magnetic nanoparticles in the vicinity of cancer cells. The Hyperthermia studies will be done using magnetic nanoparticles described in synthesis employing a home build induction heating system at the Functional Materials Laboratory. The heating efficiency of nanoparticles with different average sizes and composition would be explored to evaluated optimum size and properties required for their in-vivo use to destroy cancer cells in body. Further, the water cooled Cu coil with different physical parameters (no. of turns, length, and diameter) would be used to optimum value of AC magnetic field at the center of coil and hence obtain optimum temperature to heat cancer cells.

Chemically synthesized magnetic nanorods and Nanocomposites for Sensor and Microwave Device Applications:

During the chemical synthesis of CoFeO and NiFeO nanoparticles, their shape would be tailored to obtain nanorods with aspect ratio > 2 . These rods would be embedded in Rogers corporation polymer to make polymer-nanorods composites following the similar method described in our earlier reports [7,46] for sensor and RF microwave device applications. The rods would embed in polymer while aligning them along their long axis to obtain high attenuation and resonance frequency by incorporating shape anisotropy.

Task II: Multifunctional composites for communication and energy applications

We have been investigating CoFe₂O₄ (CFO) and PZT thin films for multiferroic coupling that may lead to the development of a sensitive biosensor. This study involved the growth and characterization of thin film heterostructures as well as doping of the PZT-COF interface with MnO for possible enhancement in magnetoelectric coupling. Results of this study within the last four quarters are presented below.

Magnetic properties of CoFe₂O₄ thin films grown on Si (100) and Al₂O₃ (0001) substrates using pulsed laser deposition

A comparative study of the structure and magnetic properties of CFO films of three different thicknesses ($t = 200$ nm, 100 nm, and 50 nm) that were grown on Si (100) substrates is presented. The CFO films of 200 nm thickness were also grown on Al₂O₃ (0001) substrates for the purpose of comparison. We observed that the 200 nm and 100 nm thick CFO-Si films possessed both (311) and (111) orientations and exhibited out-of-plane anisotropy, whereas the 50 nm thick CFO-Si film showed only a (111) texture and an in-plane anisotropy. The CFO film grown on an Al₂O₃ substrate was also found to possess only a (111) texture and an in-plane anisotropy. These observations pointed to the importance of the crystalline orientation on the observed magnetic anisotropy in the CFO thin films.

CFO thin films were grown on single crystal Si (100) and c-cut sapphire (Al₂O₃) substrates using pulsed laser deposition (PLD) technique. An excimer laser of wavelength 248 nm was used to ablate a compressed powder target of cobalt ferrite. The chamber was kept at 10 mTorr pressure of oxygen during the growth while heating the substrate to 450°C . The repetition rate of the laser pulse was kept at 10 Hz and the fluence at the target surface was $2\text{J}/\text{cm}^2$. The distance between the substrate and the target was 6 cm. Under these growth conditions, the rate of growth was measured to be around 0.1 Å/pulse. The film crystallinity and orientation were assessed by conventional θ - 2θ x-ray diffraction (XRD) (Bruker D 8 Focus and Philips X'pert Diffractometer). Peak shifts due to sample misalignment was taken care of while performing the XRD scans. The surface morphologies of the films were studied using Atomic Force Microscope (AFM, Digital Instruments). Magnetic measurements were conducted for in-plane and out-of-plane configurations of the films in magnetic fields up to 50 kOe using a commercial Physical Property Measurement System (PPMS) from Quantum Design.

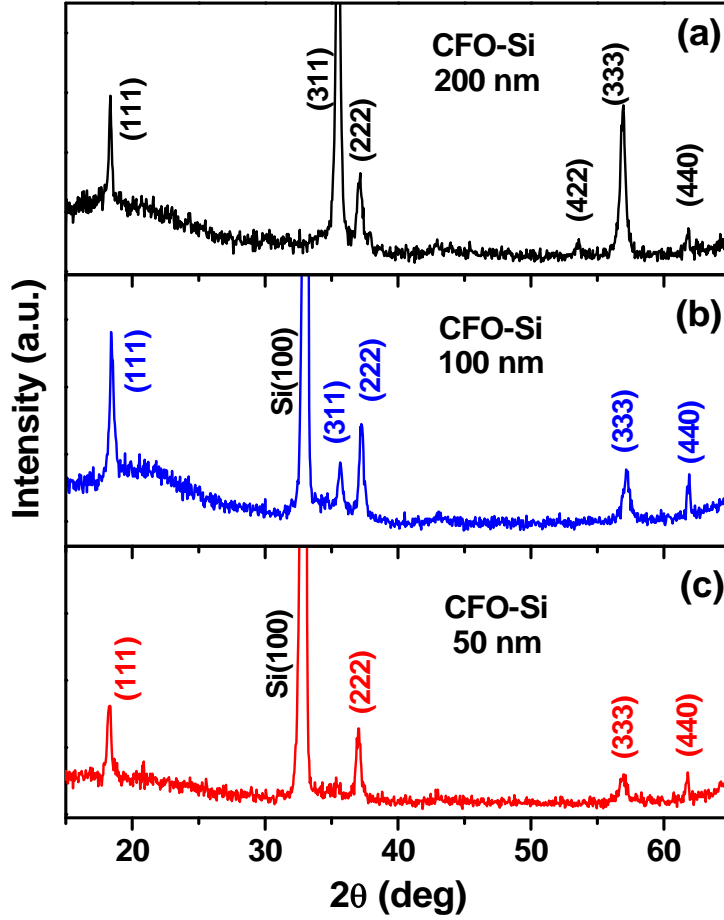


Fig 36. XRD patterns for (a) 200 nm, (b) 100 nm and (c) 50 nm thick films of CFO grown on Si (100) substrate, respectively.

Fig. 36 shows the XRD θ - 2θ scans of CFO films grown on Si substrates under the same conditions for different thicknesses of 200 nm, 100 nm, and 50 nm, respectively. The XRD pattern of the 200 nm thick film demonstrates a bulk-like polycrystalline nature (Fig. 36a). The observed peaks are indexed to the face-centered cubic phase of CFO with a space group of $Fd\bar{3}m$ (227) and lattice parameter $a = 8.391 \text{ \AA}$. While the (111) peak was present in all films investigated, the intensity of the (311) peak strongly varied with film thickness. It can be seen that the (311) peak of high intensity was observed for the 200 nm thick film (Fig. 36a), which became largely suppressed for the 100 nm thick film (Fig. 36b) and disappeared for the 50 nm thick film (Fig. 36c). Clearly, the XRD pattern of the 50 nm

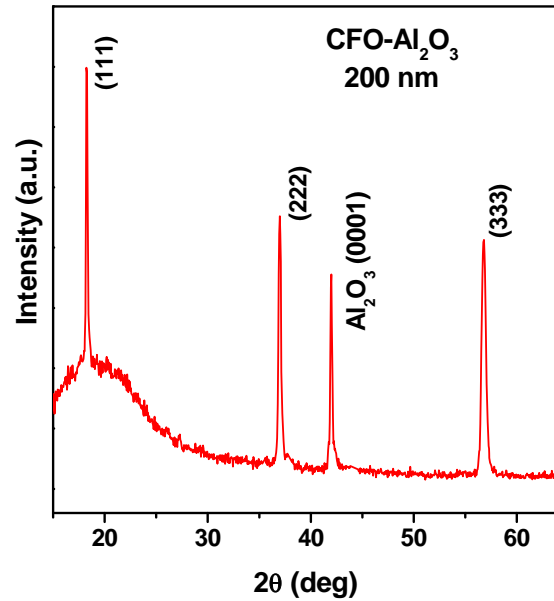


Fig. 37. XRD θ - 2θ scan of the 200 nm thick CFO film grown on an Al_2O_3 substrate.

thick film showed a complete (111) texture (Fig. 36c). This could be recoiled with the perspective that below a critical film thickness, the (111) orientation was the preferred growth direction for CFO-Si thin films [47].

To better understand this, CFO films of 200 nm thickness were grown on Al₂O₃ (0001) substrates for comparison. As one can see clearly in Fig. 37, the XRD θ -2 θ scan of this sample showed a strong (111) texture with no additional (311) orientations of CFO. This is consistent with previous observations that showed that spinel-type ferrite thin films grew with a strong (111) orientation on Al₂O₃ substrates [48,49]. The hexagonal surface unit cells of an Al₂O₃ substrate could actually provide triangular lattice nucleation sites for the CFO (111) plane. This gave a small lattice mismatch of 2.8 % between CFO and Al₂O₃ along the (111) direction. Our results presented here clearly indicate that the crystal orientation in CFO films can change depending upon film thickness and/or substrate used.

From the broadening of the XRD peaks shown in Fig. 36, the average crystallite sizes (D) in the CFO films were calculated using the Scherrer formula [50,51]. The Scherrer formula allows one to estimate D assuming spherical crystallites as $D = 4/3L$, with L given by where L is the coherence length of reflected X-rays, κ is the particle shape factor (for spherical particles, $\kappa = 0.94$), λ is the wavelength of X-rays (for CuK α , $\lambda = 1.54439$ Å), B is the FWHM of θ -2 θ peak, and θ is the angle of diffraction.

$$L = \frac{\kappa\lambda}{B\cos\theta} \quad (6)$$

Table 2 summarizes the values of D calculated using Eq. (6) for all the films. The lattice parameters (a), calculated from the XRD peaks, are also listed in Table 2. It can be seen in this table that the lattice parameters for the 200 nm and 100 nm thick CFO-Si films are very close to that for the CFO target (or bulk powder). The unchangeable lattice parameters suggest that there were no detectable stresses related to lattice distortions in these films. However, the lattice parameter of the 50 nm thick CFO-Si film was larger than that of the CFO powder (Table 2), implying that this film was under a tensile stress. A similarity was observed for the 200 nm thick CFO film grown on an Al₂O₃ substrate. It is worth mentioning in Table 2 that the crystallite size

Table 2
Lattice parameter (a) and crystallite size (D) calculated using Scherrer formula from the XRD patterns for CFO target and the deposited films on Si and sapphire substrates.

Sample	Film Thickness (nm)	Lattice parameter a (Å)	Crystallite size D (nm)
CFO target	-	8.391 ± 0.004	62 ± 9
CFO-Si	200	8.402 ± 0.014	35 ± 7
CFO-Si	100	8.391 ± 0.05	35 ± 10
CFO-Si	50	8.423 ± 0.003	28 ± 5
CFO-Al ₂ O ₃	200	8.429 ± 0.009	43 ± 17

of the 50 nm thick CFO-Si film ($D \sim 28$ nm) was smaller than those of the 200 nm and 100 nm

thick CFO-Si films ($D \sim 35$ nm). The crystallite sizes of the CFO-Si films (28-35 nm) were smaller than that of the 200 nm thick CFO film grown on an Al_2O_3 substrate ($D \sim 43$ nm) and especially of the critical single domain size for CFO (~ 40 nm) [52]. The difference in grain size of these samples would also contribute to their different magnetic properties as shown below.

To investigate the influence of film thickness on the surface morphologies of the CFO-Si films, AFM measurements were conducted on these samples. Fig. 38 shows the AFM scans (both the real and phase images) of the CFO-Si films grown for different thicknesses ($t = 100$ nm and 50 nm, respectively). Phase images offer better contrast for their infinite depth of focus. The surfaces look similar with compact and uniform grain distribution. The root mean square roughness (R_{rms}) values for the 50 nm and 100 nm thick CFO-Si films were 11.518 nm and 9.401 nm, respectively for a scan area of $10 \mu\text{m} \times 10 \mu\text{m}$. It is interesting to note that while there was a difference in crystal orientation in

the CFO-Si thin films, their surface morphologies remained similar. Such a change in the crystal orientation in these films upon thickness variation is expected to alter their magnetic properties (i.e. anisotropy direction) [53]. To verify this, magnetic measurements were conducted on these thin films using PPMS. Fig. 39 shows the in-plane and out-of-plane M-H loops at room temperature for CFO-Si films with different thicknesses of 200 nm (Fig. 39a), 100 nm (Fig. 39b) and 50 nm (Fig. 39c), and also for the 200 nm thick CFO film grown on an Al_2O_3 substrate (Fig. 39d).

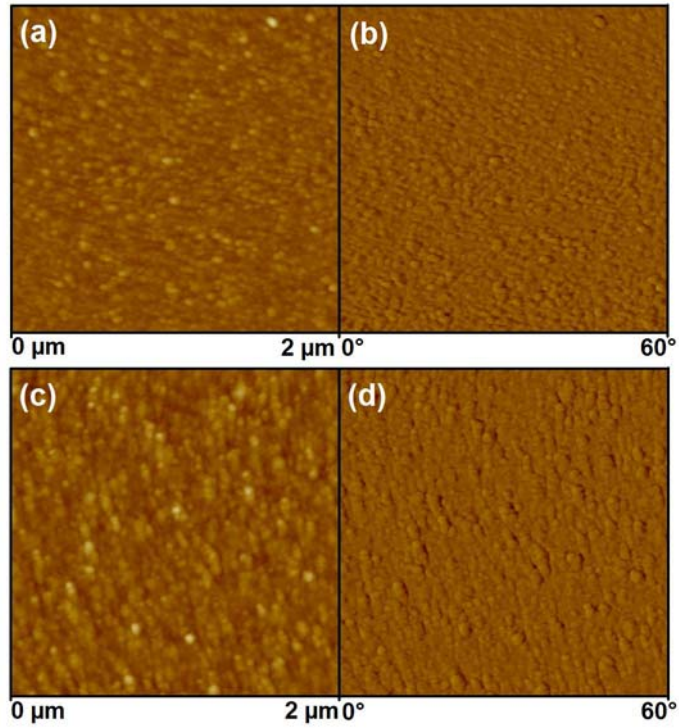


Fig. 38. AFM images showing real (a, c) and phase images (b, d) for 50 nm (a, b) and 100 nm (c, d) thick films of CFO grown on Si (100) substrates, respectively. The z-height is 40 nm.

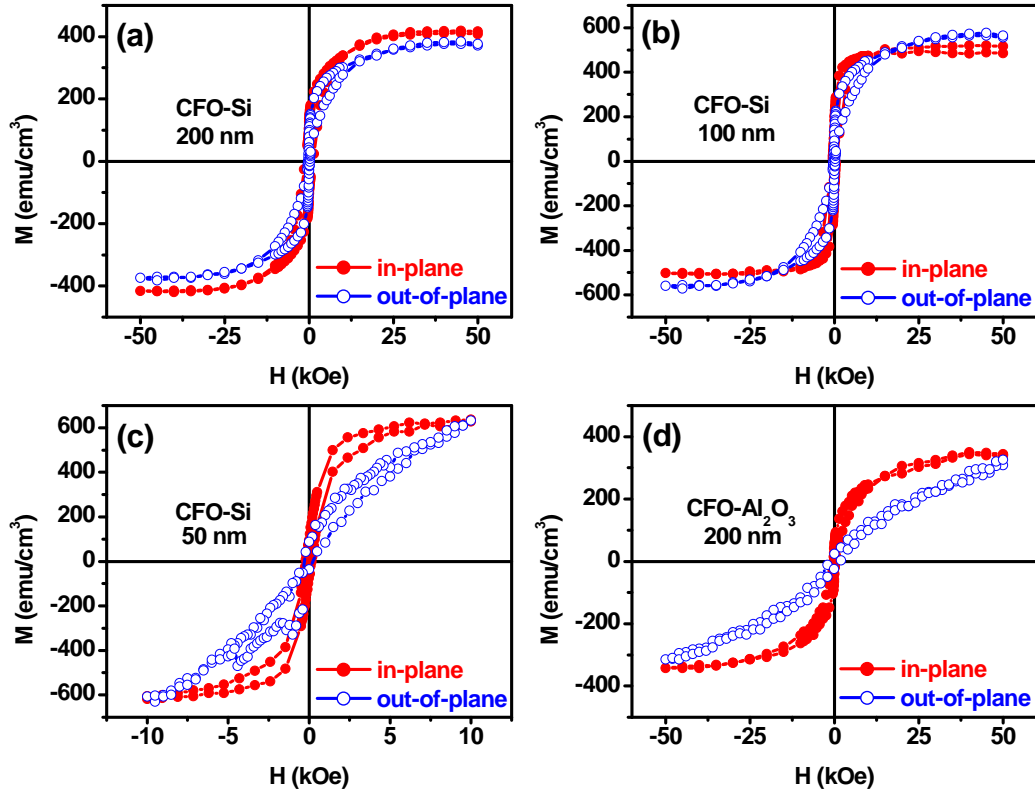


Fig. 39. M-H loops measured at 300 K for CFO films grown on Si (100) substrates at (a) 200 nm, (b) 100 nm, and (c) 50 nm thicknesses and (d) that grown on an Al_2O_3 (0001) substrate for in-plane and out-of-plane configurations.

The M-H curves presented in Fig. 39 were obtained after subtracting the diamagnetic contribution from the substrates. From this figure, the important magnetic parameters, such as

Table 3

Saturation magnetization (M_s), remnant magnetization (M_r) to saturation magnetization (M_s) ratio, and coercive field (H_c) extracted from the room temperature M-H loops for in-plane and out-of-plane configurations for 200 nm, 100 nm and 50 nm thick CFO films on Si substrates, and the 200 nm thick film of CFO on sapphire substrate. The symbols \square and \perp denote the in-plane and out-of-plane configurations, respectively.

Sample	$M_{s\parallel}$ (emu/cm^3)	$M_{s\perp}$ ($\mu\text{B}/\text{Co}^{2+}$)	$M_r/M_{s\parallel}$ (%)	$H_{c\parallel}$ (kOe)	$M_{s\perp}$ (emu/cm^3)	$M_{s\perp}$ ($\mu\text{B}/\text{Co}^{2+}$)	$M_r/M_{s\perp}$ (%)	$H_{c\perp}$ (kOe)
CFO-Si (200nm)	416 ± 2	3.3	27.6	1.2	371 ± 4	3	15.7	0.3
CFO-Si (100nm)	502 ± 12	4.0	30.1	0.5	564 ± 6	4.5	15.8	0.4
CFO-Si (50nm)	616 ± 14	4.9	13.8	0.2	631	5.3	13.7	0.3
CFO- Al_2O_3 (200nm)	342 ± 5	2.7	12.2	0.3	325	2.6	7.6	0.1

saturation magnetization (M_s), coercivity (H_c), and remanent magnetization to saturation magnetization ratio (M_r/M_s) for in-plane and out-of-plane configurations, are summarized in Table 3. It can be seen in Table 3 that for CFO films grown on Si substrates M_s increased with decrease in film thickness for both in-plane and out-of-plane configurations. The value of M_s was 416 emu/cm³ ($\sim 3.5 \mu_B$ per Co site) for the 200 nm thick CFO-Si film, which significantly increased up to 616 emu/cm³ ($\sim 4.9 \mu_B$ per Co site) for the 50 nm thick CFO-Si film. These values are higher than that of bulk CFO ($3 \mu_B$ per Co site), which could be attributed to the textured growth and smaller grain sizes as confirmed by XRD crystallite size calculation (Table 2). This is expected as the grain sizes of the CFO-Si films are smaller than the critical single domain size for CFO (~ 40 nm). The textured growth and reduced grain sizes could also cause H_c to decrease in the CFO-Si films, as the thickness of the films decreased from 200 nm ($H_c = 1.2$ kOe) to 50 nm ($H_c = 0.2$ kOe).

It is worth noting that for the 200 and 100 nm thick CFO-Si films the values of H_c were smaller for the out-of-plane configuration than for the in-plane configuration, while an opposite trend was observed for the 50 nm thick film (Table 3). This revealed that decreasing thickness of CFO-Si films changed the anisotropy direction from the out-of-plane direction to the in-plane one [53]. As one can see clearly in Fig. 40c, the M-H loop for the 50 nm thick CFO-Si film shows strong in-plane anisotropy. We recall that the 200 nm and 100 nm thick CFO-Si films grew with both (111) and (311) orientations under no stress, whereas the 50 nm thick CFO-Si film showed only an (111) orientation and was under a tensile stress. This clearly suggested that the variation in the easy axis of magnetization with film thickness in the CFO-Si films was associated with the crystal orientation and stress [53-55]. The in-plane anisotropy for the 50 nm thick CFO-Si film could thus be attributed to the crystal growth in the (111) direction and the presence of a tensile stress. This was further supported by our structural and magnetic studies on the CFO film grown on an Al₂O₃ substrate that showed that this film, which was under a tensile stress, exhibited only an (111) orientation (Fig. 38) and an in-plane anisotropy (Fig. 40d). The smaller value of M_s for the CFO film grown on an Al₂O₃ substrate, when compared to those of the CFO-Si films, could be due to the larger grain size and the presence of a tensile stress. These results clearly pointed to the importance of the crystal orientation and stress on the anisotropic magnetic properties of the CFO films. In a recent study we also showed that in CFO films strain induced by lattice mismatch between the substrate and deposited material was important in determining the magnetic anisotropy. CFO films grown epitaxially on MgO (100) with a lattice mismatch of 0.35% showed out-of-plane anisotropy, whereas the films on STO (100) with a lattice mismatch of 7.4% showed in-plane anisotropy.

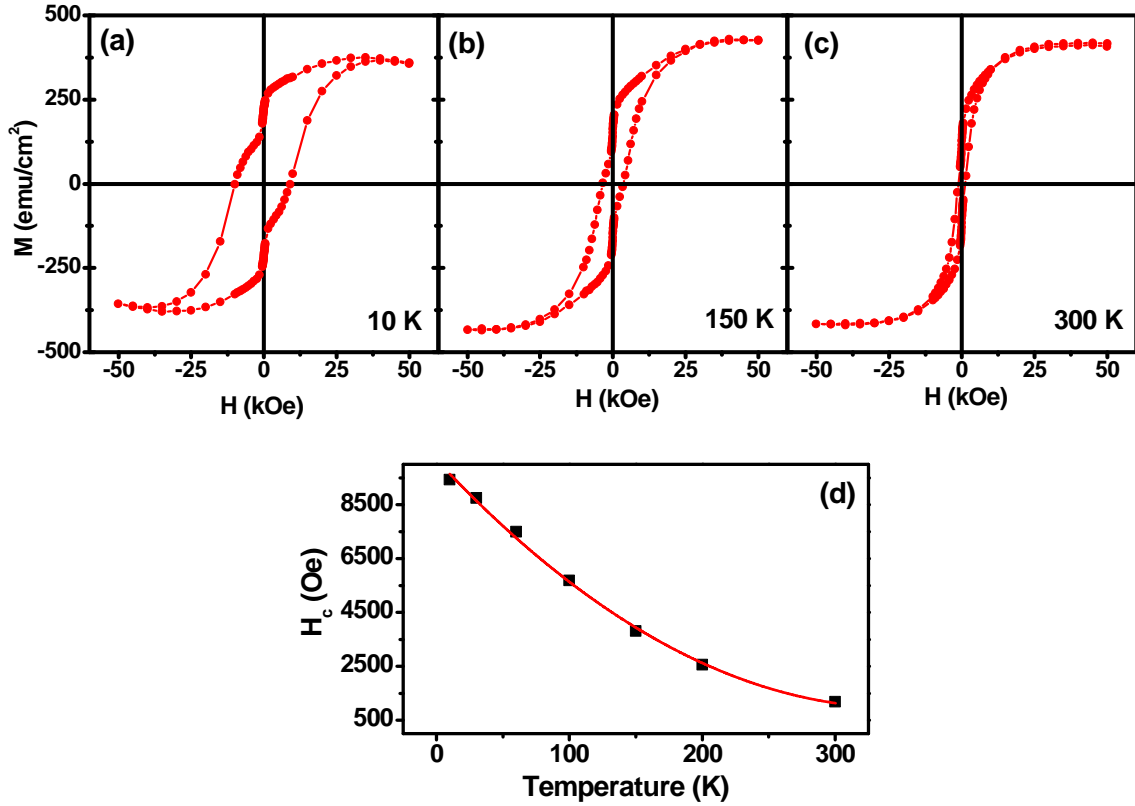


Fig. 40. M-H loops measured at (a) 10 K, (b) 150 K, and (c) 300 K for the 200 nm thick CFO film grown on a Si (100) substrate. (d) The coercivity (H_c) versus temperature.

Finally, the temperature dependence of magnetization for the CFO films grown on Si substrates was investigated. Fig. 40 (a, b, c) shows the in-plane M-H loops for the 200 nm thick CFO-Si film measured at different temperatures from 10 K to 300 K, and the temperature dependence of H_c (the values of H_c are extracted from the M-H curves) is displayed in Fig. 40d. As expected for ferrimagnetic materials, H_c increased with decreasing temperature. The increase of H_c with lowering temperature was also observed for the case of the 100 nm and 50 nm thick films (not shown here). As also shown in Fig. 40d, the temperature dependence of H_c was fitted to the following relation [56],

$$H_c(T) = H_c(0) \left[1 - \left(\frac{T}{T_B} \right)^{\frac{1}{2}} \right], \quad (7)$$

where $H_c(T)$ is coercivity at certain temperatures and T_B is the blocking temperature. From the slope of the fit shown in Fig. 40d, the T_B is deduced to be about 355 K, which is consistent with earlier reports for CFO (~390 K) [57]. The best fit of Eq. (7) to the $H_c(T)$ data also revealed the fact that the grain size of the 200 nm thick CFO film (~35 nm) was below the critical single domain size for CFO (~40 nm), which was fully consistent with the XRD data and analysis.

The influence of film thickness on the structure and magnetic properties of CoFe_2O_4 thin films grown on Si (100) and Al_2O_3 (0001) substrates using pulsed laser deposition was investigated. The CFO-Si films of 200 nm and 100 nm thickness possessed both (111) and (311) orientations and showed out-of-plane anisotropy, whereas the CFO-Si film with a thickness of 50 nm exhibited only an (111) orientation and an in-plane anisotropy. Similar to the case of the 50 nm thick CFO-Si film, the 200 nm thick CFO film grown on an Al_2O_3 substrate exhibited a complete (111) orientation and a strong in-plane anisotropy. These observations pointed to the importance of the crystalline orientation on the observed magnetic anisotropy in the CFO thin films.

Interfacial magnetoelectric coupling in epitaxial LSMO and Mn doped PZT heterostructures

We have reported the growth and characterization of $\text{CoFe}_2\text{O}_4/\text{PZT}$ layered structures which are of great interest for multiferroic devices. In this project multiferroic materials are investigated for the possible fabrication of bio sensors. In this report we are presenting the incorporation of a Mn_3O_4 layer between the LSMO and PZT layers in order to enhance the magnetoelectric coupling.

Epitaxial $\text{La}_{0.7}\text{Sr}_{0.3}\text{MnO}_3/\text{PbZr}_{0.52}\text{Ti}_{0.48}\text{O}_3$ (LSMO/PZT) bilayer thin films were deposited on single crystal SrTiO_3 (STO) (100) substrates. The aim was to investigate the ferromagnetic-ferroelectric interface of LSMO-PZT heterostructures for potential multiferroic applications. Besides studying the multiferroic properties of the heterostructures, the ferromagnetic metallic oxide $\text{La}_{0.7}\text{Sr}_{0.3}\text{MnO}_3$ (LSMO) can also be used to reduce fatigue in PZT capacitors [58-62]. Fatigue is caused by the defects due to oxygen vacancies in the PZT films. [58]. It has been suggested that the oxide electrodes act as a sink for oxygen vacancies so that they do not pile-up at the film-electrode interface [59]. Further, LSMO thin films have also has attracted great interest recently due to their colossal magnetoresistance [63].

The LSMO thin films were first deposited on STO (100) substrates prior to the PZT layer deposition. The LSMO target was purchased from Kurt J. Leskar Company with a composition of $\text{La}_{0.7}\text{Sr}_{0.3}\text{MnO}_3$. The LSMO films were deposited at 700 °C under oxygen pressure $p\text{O}_2$ of 10 mT using a laser fluence of 2 J/cm². The similar crystal structure between LSMO (pseudo-cubic, $a = 0.387$ nm) and STO (cubic, $a = 0.3905$ nm) and the extremely small lattice mismatch (0.009 %) allow for the growth of almost perfectly epitaxial LSMO films on STO substrates. Figures 41 (a, and b) shows the XRD patterns for LSMO-STO film and STO substrate.

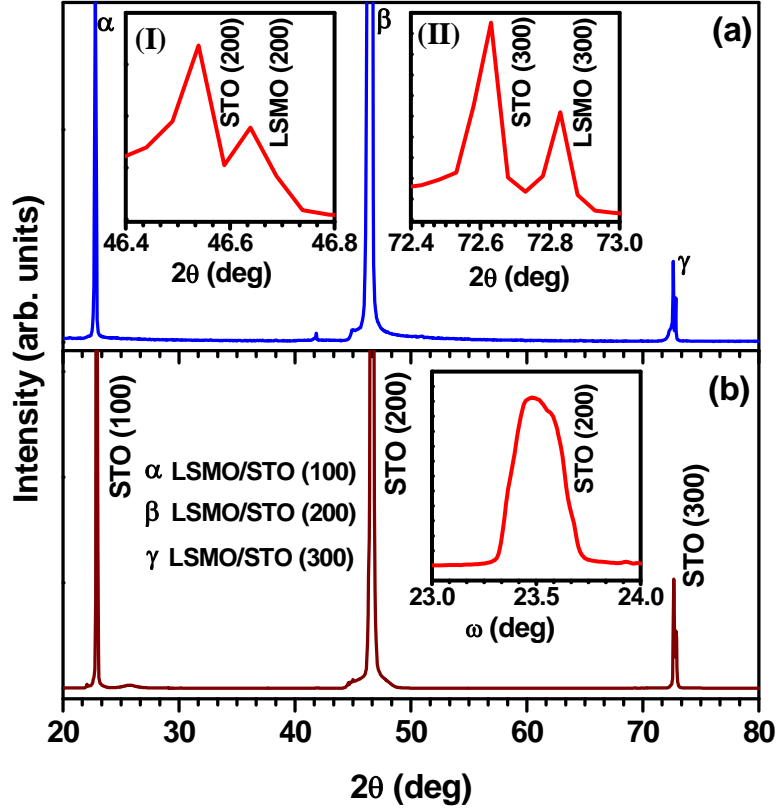


Fig. 41 XRD patterns of (a) LSMO film on STO substrate and (b) STO substrates, respectively. The insets (I) and (II) to (a) shows the details of the STO(200)/LSMO(200) and STO(300)/LSMO(300) peaks. The inset to (b) shows the rocking curve performed about the STO (200) plane.

The XRD patterns are almost identical indicating the highly epitaxial nature of the film. The insets (I) and (II) to Figure 41 (a) shows the details of the STO(200)/LSMO(200) and STO(300)/LSMO(300) peaks. The inset to Figure 41 (b) shows the rocking curve performed about the STO (200) plane. The FWHM of the rocking curve is 0.268° which confirms the high degree of in orientation in STO. For the PZT-LSMO heterostructure, the structural characterization performed using XRD confirmed the high degree of in-plane orientation and epitaxial relationship between the layers. Figure 42 shows the XRD patterns for PZT-LSMO heterostructures and single layer LSMO thin films. Only the (100) planes of PZT were observed, indicating a highly textured nature in the films.

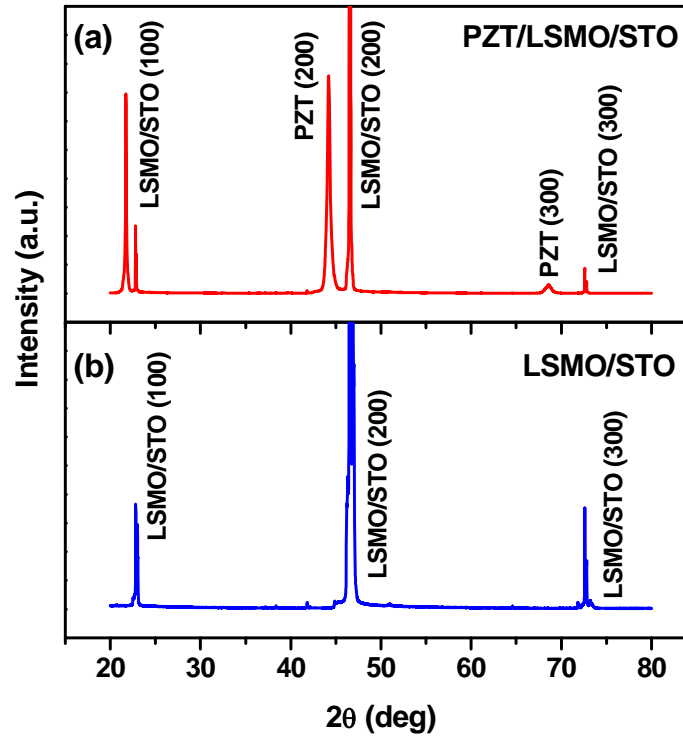


Fig. 42 XRD patterns of (a) PZT-LSMO bilayer film on STO substrate and (b) LSMO single layer film on STO substrates, respectively.

Magnetization measurements at 300 K exhibited a strong in-plane magnetic anisotropy with well saturated in plane magnetization (M_s) values of 431 emu/cm^3 and 433 emu/cm^3 for the LSMO single layer and PZT-LSMO bilayers on STO substrates. The out of plane magnetization showed an unsaturated behavior even at high fields. From the M-H loop it was observed that the easy axis of magnetization was along the film plane. It is to be noted that the bulk saturation magnetization for LSMO has been reported to be around 600 emu/cm^3 . Figure 43 (a, and b) shows the in plane and out of plane M-H loops for PZT-LSMO bilayers and LSMO single layers on STO substrates, respectively.

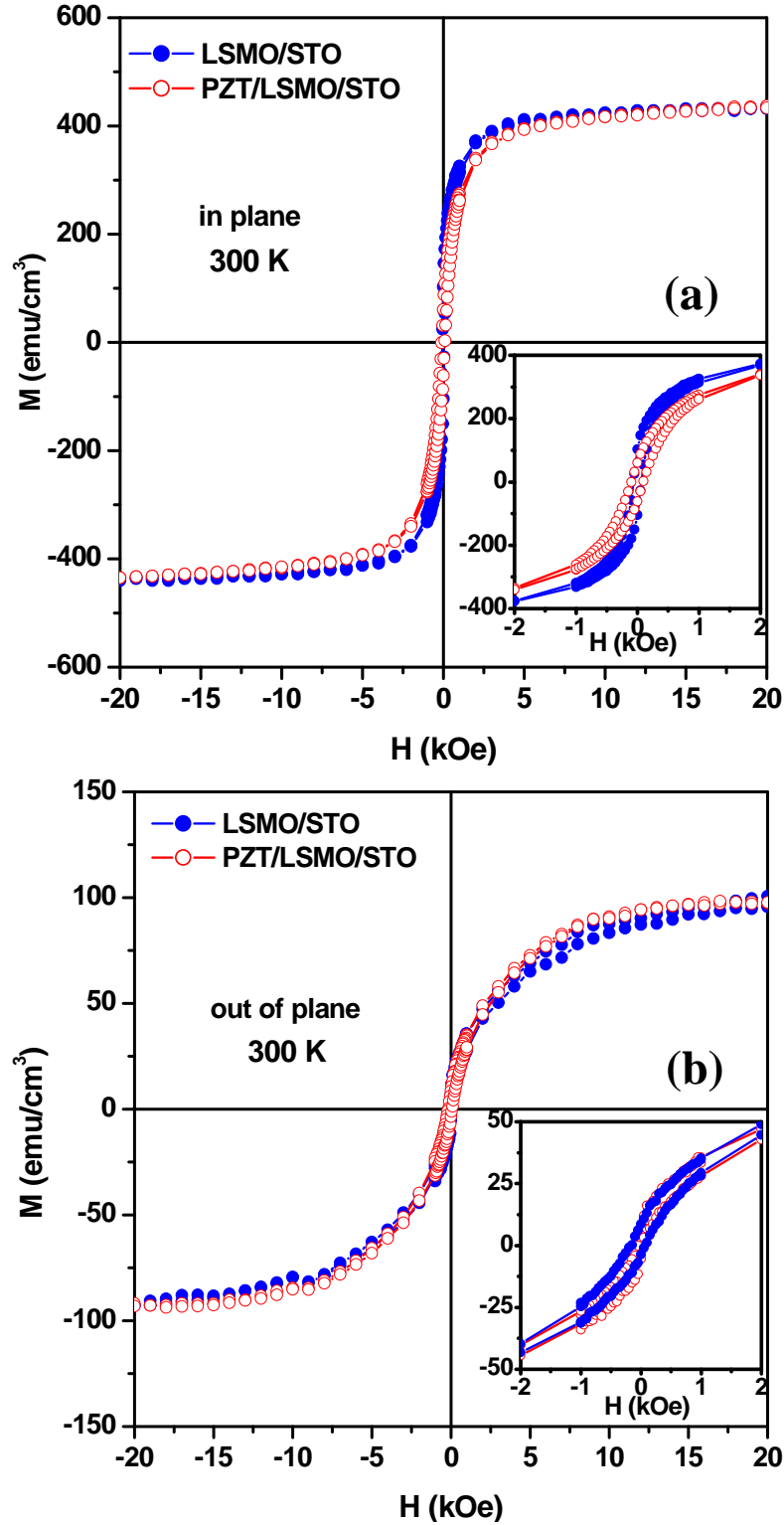


Fig. 43. M-H loops at 300 K for PZT-LSMO bilayers and LSMO single layers on STO substrates for (a) in plane and (b) out of plane configurations.

In order to determine the easy axis of magnetization, effective magnetic anisotropy measurements were performed using the RF transverse susceptibility technique for LSMO/PZT

bilayer on STO substrate. The RF transverse susceptibility technique is based on a sensitive, self-resonant tunnel diode oscillator (TDO) incorporated into the Physical Property Measurement System (PPMS) and has been validated over the years to be an excellent technique for probing magnetic anisotropies in nano-structured materials. Figure 44 shows the in plane TDO measurements for PZT/LSMO/STO structure for both increasing and decreasing magnetic fields (H). When H is applied parallel to the film plane the experimentally observed peaks occur at very low fields of 6.13 Oe and 19.14 Oe. This is a clear indication that the easy axis of magnetization is along the film plane.

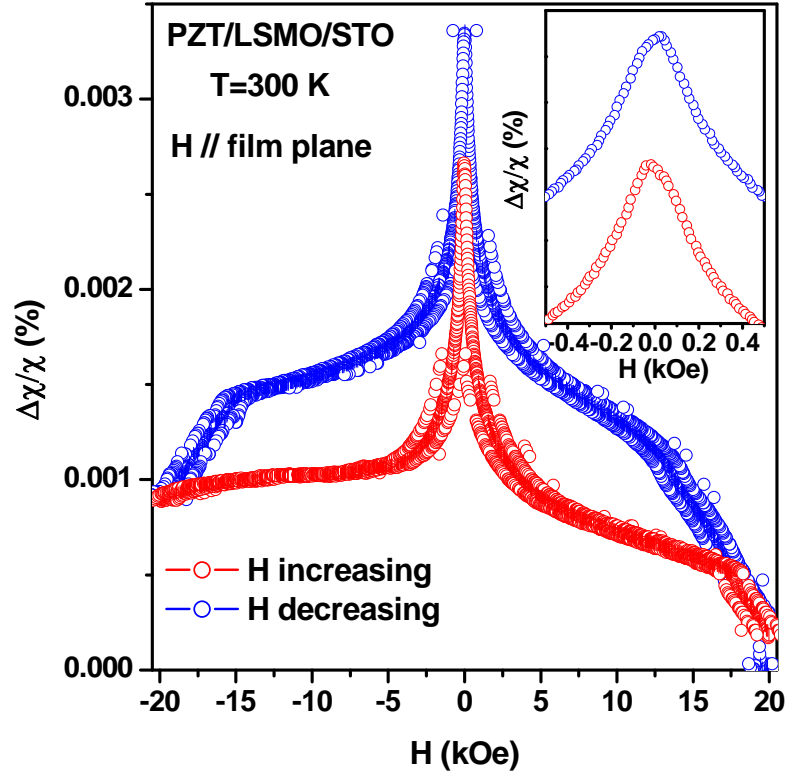


Fig. 44 Measured room temperature transverse susceptibility with H applied parallel to the film plane for PZT/LSMO/STO heterostructure.

In an attempt to manipulate the magnetic behavior in the bilayers, an ultra-thin buffer layer of Mn_3O_4 was deposited at the interface of LSMO and PZT heterostructure. Mn_3O_4 is a ferrimagnetic insulating oxide with a much lower Curie temperature (T_c) as compared to that of LSMO. It is chemically compatible with LSMO and does not effect the stoichiometry of the manganite phase in the nanocomposites films [64]. Further with the deposition of the PZT layer it could lead to the possibility of a double exchange interaction across the interface between the Mn^{4+} in PMZT layer and Mn^{3+} in LSMO layer. Figure 45 shows the M-H loops for LSMO- Mn_3O_4 heterostructures on STO substrates with varying thicknesses of the Mn_3O_4 layer. The LSMO layer thickness has been kept constant at 100 nm. It was observed that the M_s values decreased as the Mn_3O_4 layer thickness was increased. The single Mn_3O_4 film grown on STO showed a M_s value of about 150 emu/cm^3 which is lower than that of the bulk value of 174 emu/cm^3 .

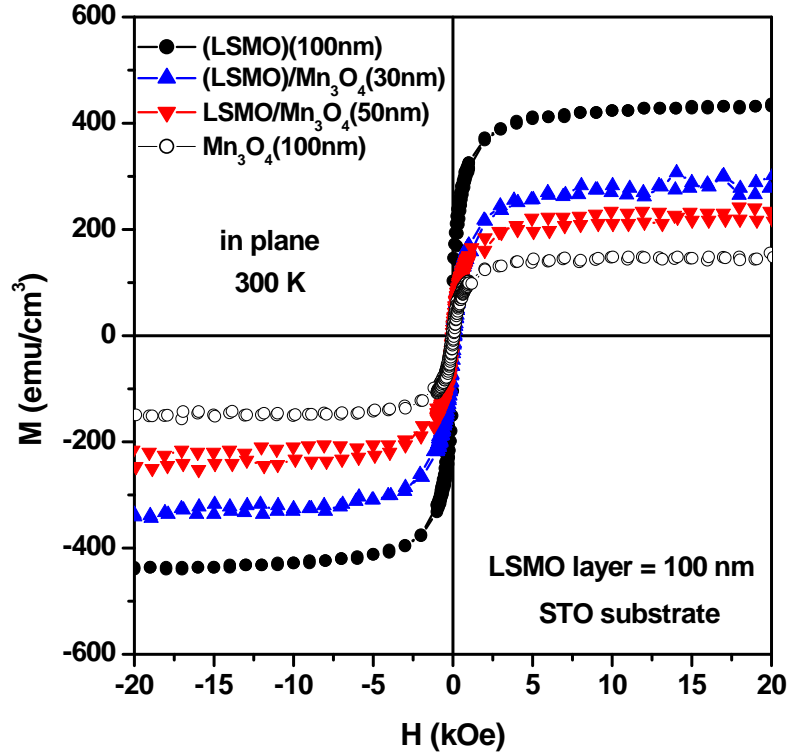


Fig. 45. *M-H loops at 300 K for LSMO-Mn₃O₄ heterostructures on STO substrates with varying thicknesses of the Mn₃O₄.*

Strain-influenced Ferromagnetism in Epitaxial Mn₃O₄/La_{0.7}Sr_{0.3}MnO₃ Thin Films grown on MgO (100) and SrTiO₃ (100) substrates

Apart from the colossal magneto-resistance (CMR) effect that has potential applications in data storage devices [44, 45], the ferromagnetic half-metal LSMO is an interesting material for other applications such as in multiferroic devices [65-70] and magnetic tunnel junctions [71, 72]. All these applications require LSMO thin films and their performance depends of the quality of the thin films. However, the optimization of the growth parameters for high quality LSMO thin films is not a trivial task. Precipitation of the chemically compatible insulating oxide Mn₃O₄ on the surface of La_{0.7}Sr_{0.3}MnO₃ (LSMO) thin films during their pulsed laser deposition (PLD) has been an emerging issue for fabricating high quality devices [73]. A recent study has shown that the room temperature magnetic properties of (La_{0.7}Sr_{0.3}MnO₃)_{0.7}:(Mn₃O₄)_{0.3} nanocomposite thin films strongly depend on the microstructure and lattice distortion due the presence of different domains and grain boundary structures [74]. In order to addresses these issues we studied strain mediated ferromagnetism in of epitaxial LSMO thin films and Mn₃O₄/LSMO bilayer thin films, which were deposited in-situ at 750°C on single crystal MgO (100) and SrTiO₃ (STO) (100) substrates using PLD technique.

Fig. 46 (a, and b) shows the XRD θ -2 θ symmetric scans for LSMO thin films grown on single crystal STO (100) and MgO (100) substrates, respectively. The insets to Fig. 46 shows the

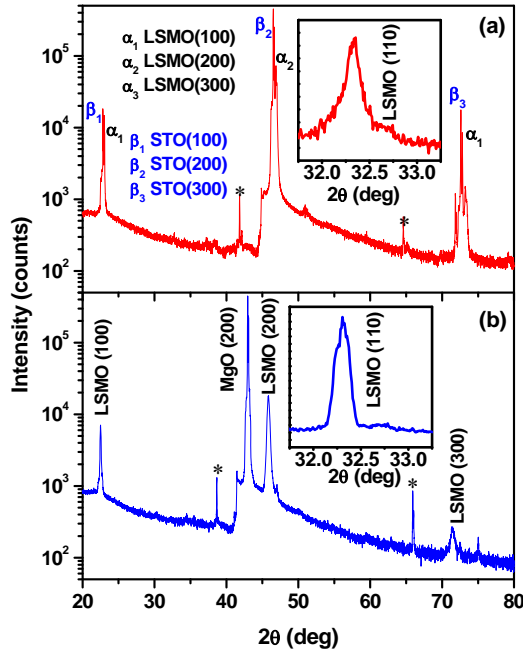


Fig. 46 XRD θ - 2θ symmetric scans for LSMO thin films grown on single crystal (a) STO (100) and (b) MgO (100) substrates, respectively. The insets to Fig. 1 shows the corresponding asymmetric scans about the LSMO (110) planes.

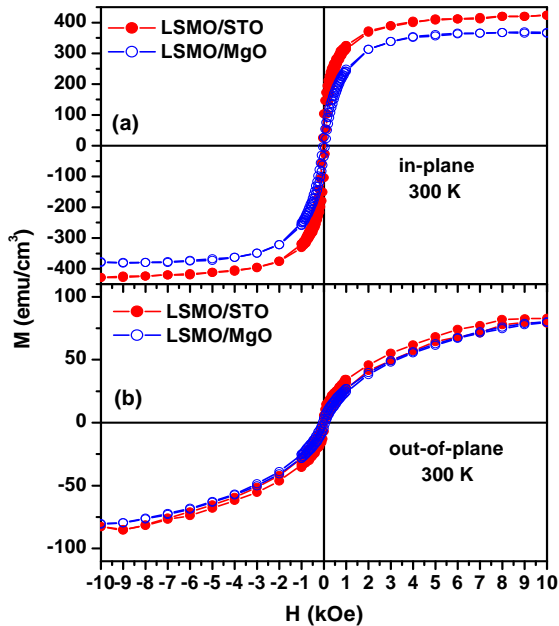


Fig. 47 M-H loops measured at 300 K for LSMO thin films on STO and MgO substrates for (a) in-plane and (b) out-of-plane configurations, respectively.

corresponding asymmetric scans about the LSMO (110) planes. Both the scans revealed the single crystalline nature and the epitaxial relationship between the film and the substrate. The out-of-plane lattice parameter (a_{\perp}) and the in-plane lattice parameter (a_{\parallel}) for LSMO thin films were calculated from the symmetric and asymmetric scans, respectively. The out-of- and in-plane lattice parameters for LSMO film on STO were $a_{\perp}=3.895 \text{ \AA}$ and $a_{\parallel} = 3.903 \text{ \AA}$. The almost same lattice parameters in LSMO-STO film confirmed the (pseudo)cubic unit cell of LSMO and cube-on-cube growth morphology due the very small lattice mismatch (1 %) between LSMO and STO. On the other hand, the out-of- and in-plane lattice parameters for LSMO film on MgO were $a_{\perp}=3.955 \text{ \AA}$ and $a_{\parallel} = 3.910 \text{ \AA}$. The smaller in-plane lattice parameter indicated an in-plane compression of the LSMO unit cell due to the larger lattice mismatch (8 %) between LSMO and MgO.

The strain influenced ferromagnetism of LSMO films was observed in the magnetization (M-H) hysteresis loops of LSMO films. Fig. 47 (a, and b) shows the M-H loops measured at 300 K for LSMO thin films on STO and MgO substrates for in-plane and out-of-plane configurations, respectively. From the figure it is evident that the preferred direction of magnetization for LSMO is along the film plane for both STO and MgO substrates. Due to the larger lattice mismatch between LSMO and MgO ($\sim 8\%$), the M_s (372 emu/cm^3) of the LSMO film grown on an MgO (100) substrate was found to be smaller than that (436 emu/cm^3) of the LSMO film grown on a SrTiO_3 (100) substrate (lattice mismatch $\sim 1\%$). In order to investigate the effect of Mn_3O_4 layers on the strain and magnetic properties of LSMO, epitaxial Mn_3O_4 /LSMO bilayer films were grown with varying thicknesses of the

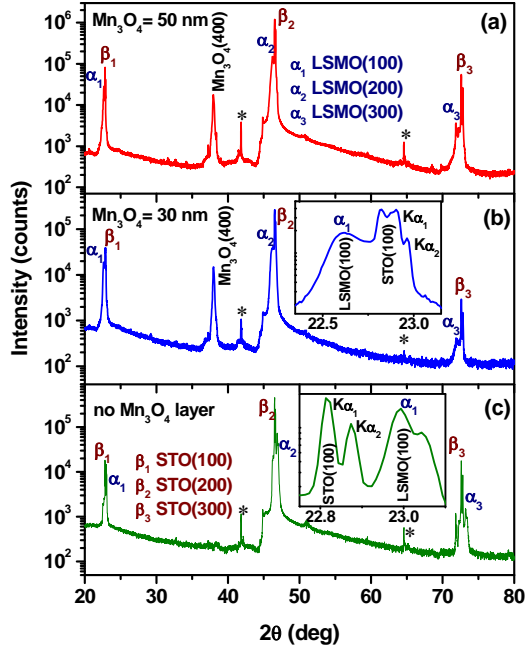


Fig. 48 XRD θ - 2θ symmetric scans for $\text{Mn}_3\text{O}_4/\text{LSMO}$ bilayer thin films grown on STO (100) substrates with varying thicknesses of the Mn_3O_4 layer as (a) 50 nm, (b) 30 nm, and (c) 0 nm, respectively. The insets to (b) and (c) show the details of the LSMO (100) and STO (100) peaks.

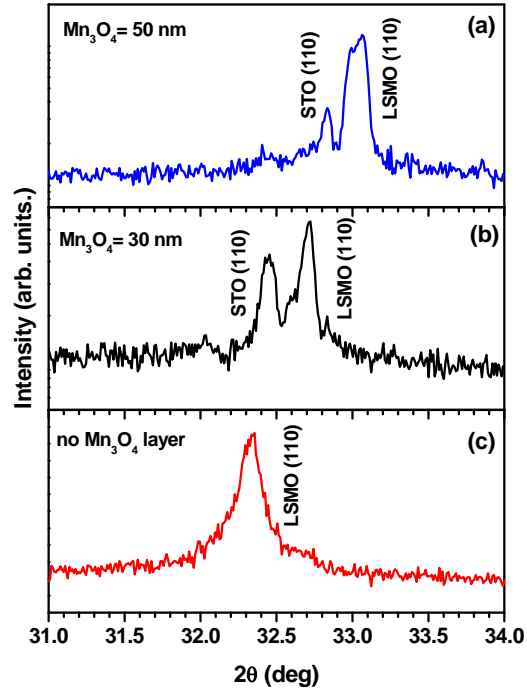


Fig. 49 XRD asymmetric scans of LSMO (110) planes for $\text{Mn}_3\text{O}_4/\text{LSMO}$ bilayer thin films grown on STO (100) substrates with varying thicknesses of the Mn_3O_4 layer as (a) 50 nm, (b) 30 nm, and (c) 0 nm, respectively.

Mn_3O_4 layer. Fig. 48 shows the XRD θ - 2θ scans for $\text{Mn}_3\text{O}_4/\text{LSMO}$ bilayer films grown on STO substrates with the thickness of the Mn_3O_4 layer varying from 0 to 50 nm. The XRD scans revealed the single crystalline nature and the epitaxial relationship between the layers. Fig. 49 shows the XRD asymmetric scans of LSMO (110) planes for $\text{Mn}_3\text{O}_4/\text{LSMO}$ bilayer thin films grown on STO (100) substrates with varying thicknesses of the Mn_3O_4 layer as (a) 50 nm, (b) 30 nm, and (c) 0 nm, respectively. From the figure the peak shift for the LSMO (110) plane for $\text{Mn}_3\text{O}_4/\text{LSMO}$ bilayers compared to LSMO single layer is evident. This indicated of an in-plane compression of the LSMO unit cell with deposition of Mn_3O_4 layer. The out-of- and in-plane lattice parameters for $\text{Mn}_3\text{O}_4/\text{LSMO}$ film on STO with 30 nm thickness of the Mn_3O_4 layer were $a_{\perp}=3.905 \text{ \AA}$ and $a_{\parallel} = 3.82 \text{ \AA}$. The much smaller in-plane lattice parameter indicated a highly compressed state of the LSMO unit cell along the film plane.

Magnetization measurements showed a gradual decrease in the saturation magnetization (M_s) of the $\text{Mn}_3\text{O}_4/\text{LSMO}$ bilayers with increasing the thickness of the Mn_3O_4 layer, keeping the same LSMO thickness of 100 nm for the samples. The M_s decreased from 436 emu/cm^3 for single LSMO-STO films to 240 emu/cm^3 and 166 emu/cm^3 for $\text{Mn}_3\text{O}_4/\text{LSMO}$ -STO bilayer films with 30 nm and 50 nm thick Mn_3O_4 layers, respectively, as shown in Fig. 50.

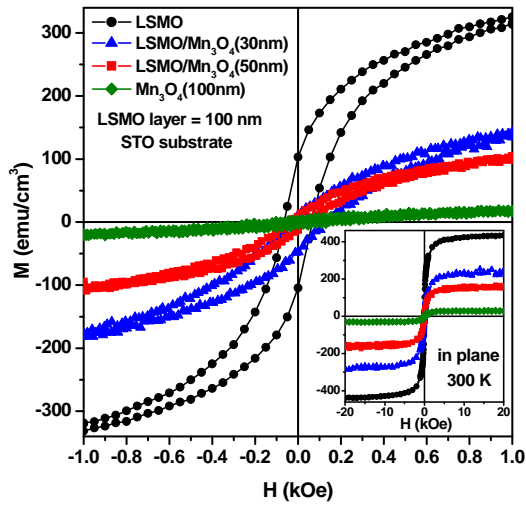


Fig. 50 M-H loops at 300 K for LSMO and Mn₃O₄ single layers and Mn₃O₄/LSMO bilayers for varying thicknesses of Mn₃O₄ layer as 30 nm and 50 nm. Inset shows the M-H saturation loops at higher magnetic fields.

Cross-sectional high resolution transmission electron microscopy (HRTEM) was used to view the interfacial atomic structure in the Mn₃O₄/LSMO bilayer films. Fig. 51 (a, and b) shows the HRTEM images of the Mn₃O₄-LSMO interface and the LSMO-STO interface for Mn₃O₄/LSMO bilayer film with Mn₃O₄ layer thickness of 30 nm. From the figures it is clearly evident that the interface between Mn₃O₄ and LSMO is zig-zag as opposed to the atomically sharp and flat interface between LSMO and STO substrates.

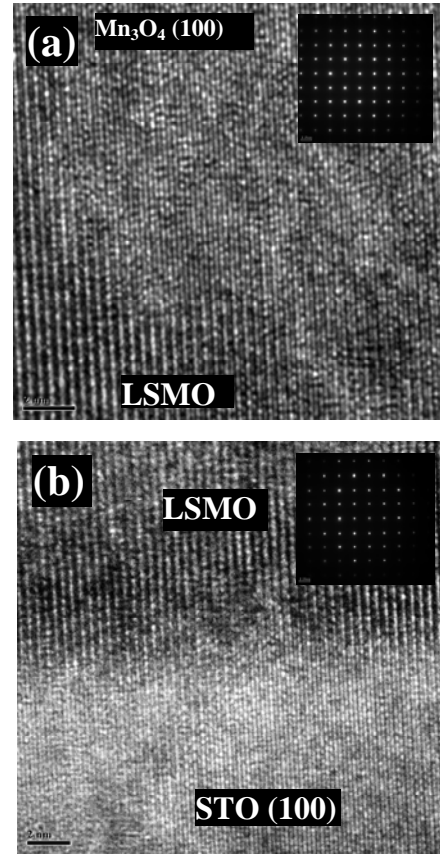


Fig. 51 HRTEM images of the Mn₃O₄-LSMO interface and the LSMO-STO interface for Mn₃O₄/LSMO bilayer film with Mn₃O₄ layer thickness of 30 nm. The inset show the SAED patterns for the top (a) Mn₃O₄ layer and (b) LSMO layer, respectively.

These above results revealed that the intrinsic growth morphology of Mn₃O₄ layers on LSMO thin films significantly changed the lattice strain of LSMO and hence the magnetic properties of the material.

Growth of Pb(Zr_{0.52}Ti_{0.48})O₃ nano-wires through a hydrothermal process

Nanopillar and nanowire structures of PZT offer the advantage of large surface area to enhance the strain mediated coupling of ferroelectric and ferromagnetic composites. One of the challenges is to fabricate PZT nanowires with the proper stoichiometry. Many groups around the world have attempted to fabricate nano-scale structures of Pb(Zr_{0.52}Ti_{0.48})O₃ (PZT) using various techniques. Of these the most successful have been chemical vapor deposition [75-77], template methods [78,79] and hydrothermal growth [80]. We have used a hydrothermal technique to grow PZT wires. The following sections outline the procedures followed and the resultant outcomes.

Experimental Procedures

As already mentioned a hydrothermal process [80] was used to fabricate PZT nano-wires. The nano-wires were grown on a titanium oxide layer formed on the surface of a titanium foil (0.1mm thick, purity>99.9%) by a thermal treatment of 600 °C for 5 min.

The hydrothermal solution was prepared in two stages. First, $\text{Zr}_{0.52}\text{Ti}_{.48}\text{O}(\text{OH})_2$ (ZTOH) was produced following the procedure outlined below and mixed with $\text{Pb}(\text{NO}_3)_2$, KOH, poly(vinyl alcohol)(PVA) and poly(acrylic acid)(PAA).

Synthesis of ZTOH

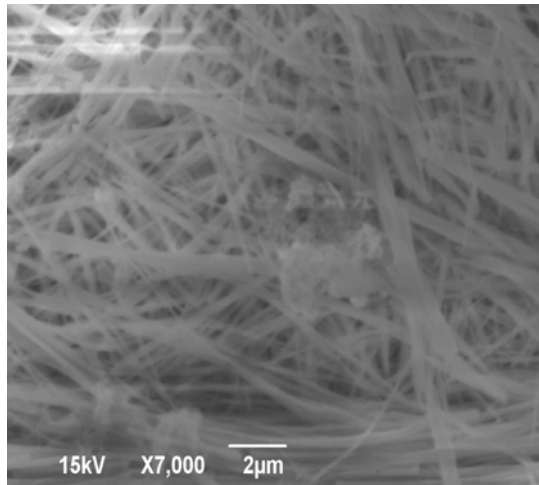
Tetrabutyl titanate ($[\text{C}_4\text{H}_9\text{O}]_4\text{Ti}$) was dissolved in ethanol to form a 0.1M solution, and zirconium oxychloride ($\text{ZrOCl}_2 \cdot \text{H}_2\text{O}$) was dissolved in deionized water to form a 0.08M solution. The Ti^{4+} solution was added into the Zr^{4+} aqueous solution in the molar ratio of 48:52 (Ti:Zr) under vigorous stirring. The mixture was introduced to an ammonia solution, which resulted in the coprecipitation of ZTOH.

Hydrothermal solution

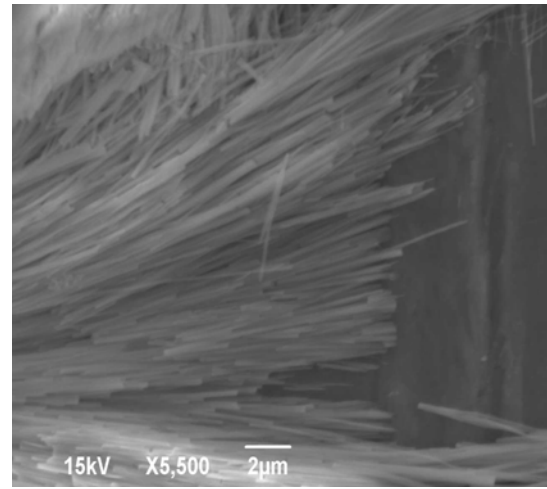
The filtered ZTOH was mixed with $\text{Pb}(\text{NO}_3)_2$ and KOH to obtain concentrations of 0.1M, 0.1M and 2M respectively. PVA and PAA were also added in the concentrations of 0.4 g/L and 7.2 g/L. The solution prepared in this manner and the TiO_2 substrate were placed inside a stainless steel autoclave with a Teflon lining having a capacity of 50ml. The autoclave was placed inside an oven (Model 30 GC Lab Oven) and heated at 175 °C for 12 h. After letting the autoclave cool down to room temperature the substrate was removed and cleaned using DI water and dried with N_2 gas.

Test Results:

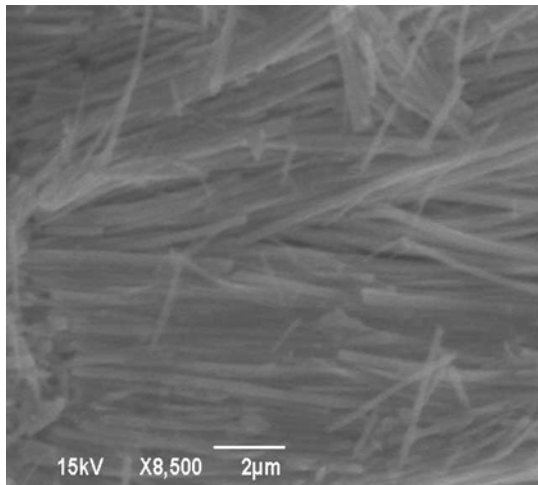
Scanning electron microscopy revealed that nano-wires were formed on the substrate as shown in Fig.52. As the figures show, the nano-wires are randomly ordered and not necessarily perpendicular to the plane of the substrate.



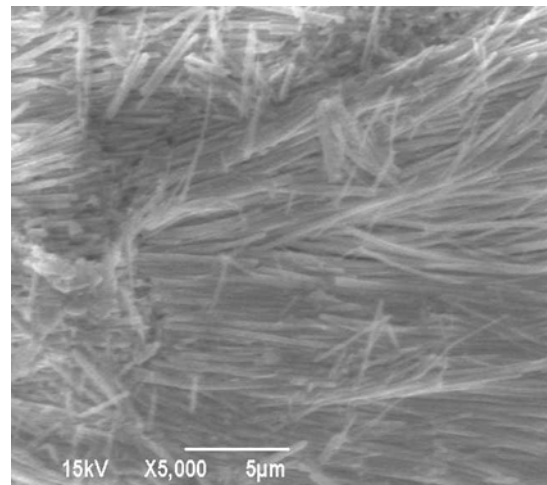
(a)



(b)



(c)



(d)

Fig.52. SEM image of PZT nano-wires grown on Ti substrate.

Conclusion

Future direction for this research would be to improve upon the results presented above, by possibly integrating the hydrothermal process with pulsed laser deposition techniques, and grow vertically aligned nano-wires on different types of substrates (e.g. MgO).

Task III : Solid-state materials for power generation and refrigeration

Growth of nanoparticulate films of $\text{Ca}_3\text{Co}_4\text{O}_9$ by a one-step microwave plasma process for heat to electric power conversion

In this work we used a microwave plasma assisted spray (MPAS) deposition process to form nanoparticle films of the thermoelectric material $\text{Ca}_3\text{Co}_4\text{O}_9$. By varying the concentration of the precursor used for forming the particles, different-sized nanoparticulates were grown. The resistivity, Seebeck coefficient, and thus power factor of a set of films grown by MPAS with varying concentrations of calcium and cobalt salts are presented. The resistivity and Seebeck coefficients of these films were measured from 300 – 700 K. The films with larger imbedded nanoparticles showed a trend toward higher power factors than those with smaller nanoparticles. The best films grown by this process were shown to have good electrical conductivities, and subsequently high power factors. Films grown by this technique had room temperature power factors as high as $220 \mu\text{W}/\text{mK}^2$.

In the MPAS process an aqueous precursor containing calcium and cobalt nitrates is atomized by a nebulizer to generate an aerosol of drop sizes in the range of $1 \mu\text{m}$. The aerosol is injected into a reaction zone with the carrier gas oxygen. Microwave energy delivered through a waveguide was coupled into the flowing gas through a quartz tube to create a plasma as shown in Figure 53. The microwave plasma heats the surrounding gas and water causing the solvent to evaporate. The droplets reduce in size and the salts react due to the plasma heat to form nanoparticles which are finally deposited onto a heated substrate ($\sim 800^\circ\text{C}$). Note that this temperature is well below the $>900^\circ\text{C}$ preferred crystallization point of $\text{Ca}_2\text{Co}_2\text{O}_5$. [81] The

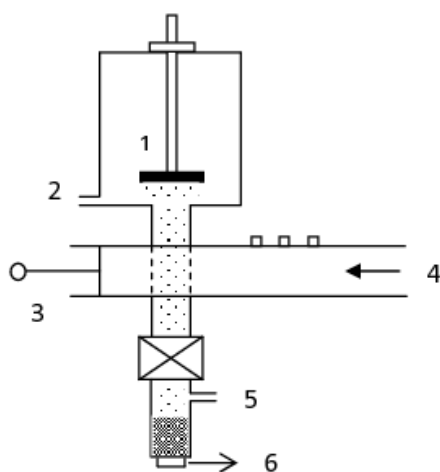


Fig. 53. Schematic of a microwave assisted spray (MPAS) system. 1. Substrate. 2. Outlet for vacuum. 3. Microwave waveguide with three tuners and a handle which can slide back and forth to adjust the length of the guide. 4. Microwave input. 5. Inlet for gas flow. 6. Nebulizer below the cylinder which contains the precursor solution.

temperature of the gas entering the deposition chamber was measured using a thermocouple. The temperature within the plasma region was previously determined by an optical emission spectroscopy technique and shown to be greater than 2000°C [82].

Films were deposited on quartz substrates with solute concentrations from 0.1M to 0.0008M. This technique was used to create films containing many nanograined particles. The nominal thickness of the films was 0.8 micron. The concentration was reduced by 50% for each successive decrease in concentration. Hereafter, the concentrations are referred to as 100, 50, 25, etc. respectively, representing the reduction from full concentration of the original precursor, of

molarity from 0.1M to 0.0008 M. The morphology and crystallinity of as-grown films were investigated by SEM and XRD. The electrical properties including resistivity and Seebeck coefficients were measured as a function of temperature using a commercially available instrument.

Film Morphology

Scanning Electron Microscope (SEM) images of a film grown by MPAS process is shown in Figure 54. Films grown with lower concentrations show a smoother surface while at higher concentrations films tend to grow with their a-b plane along the substrate. Transmissive Electron Microscope (TEM) images give more information about the smaller nano-sized grain boundaries which form in the composite films as seen in Figure 55. The left side of the figure is from a lower concentration deposition and many particles as small as 10 nm can be seen. The right side is from a medium concentration deposition, where particles are clearly much larger than on the left, the average on the order of 20 nm, an increase by a factor of 4 in the nanoparticle volume. The TEM images indicate that smaller particles with multitude of boundaries were formed at lower concentrations while larger particles with less boundaries were grown at higher concentrations. This trend of nanoparticle size correlating with precursor concentration was also seen in a previous MASP study of ZnO nanoparticles. [83]

X-Ray Diffraction (XRD) scans also support the strong crystallinity of the films (Figure 56). The scans shown were made from films of the same nominal thickness for varying molar concentrations, and shows that the strength of the peaks increases with increasing molar concentration. This indicates enhanced crystallinity of the films with increasing precursor concentration. The change in the diffraction peak width, which is indicative of different grain sizes, also confirms the ability to control the sizes of the particles grown by varying the starting precursor concentration (Figure 57).

Transport Properties.

Resistivity and Seebeck measurements were carried out using a commercial apparatus (ZEM-3, ULVAC, Inc., Methuen, MA.) This apparatus measures the electrical conductivity by a 4 point current-switching technique. In addition, the Seebeck coefficient was measured by a static dc method. Seebeck coefficient was determined from the slope of voltage difference

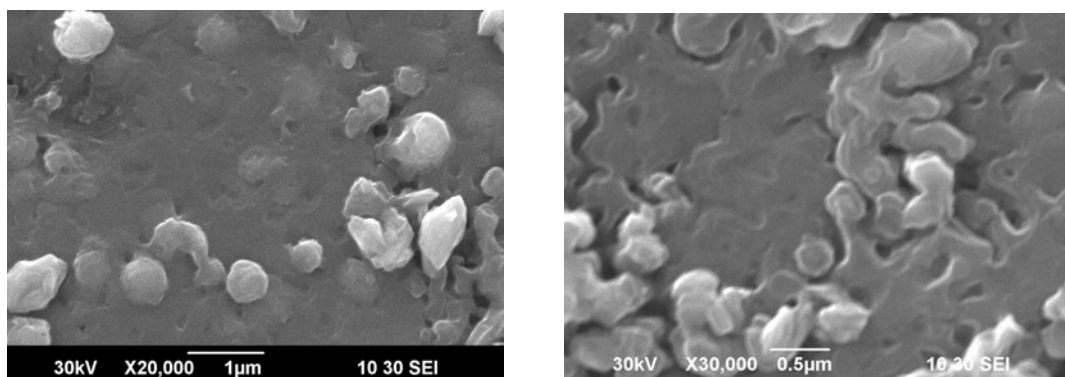


Fig. 54. SEM images of films grown with (a) low concentration precursor (left), and (b) higher concentration precursor (right)

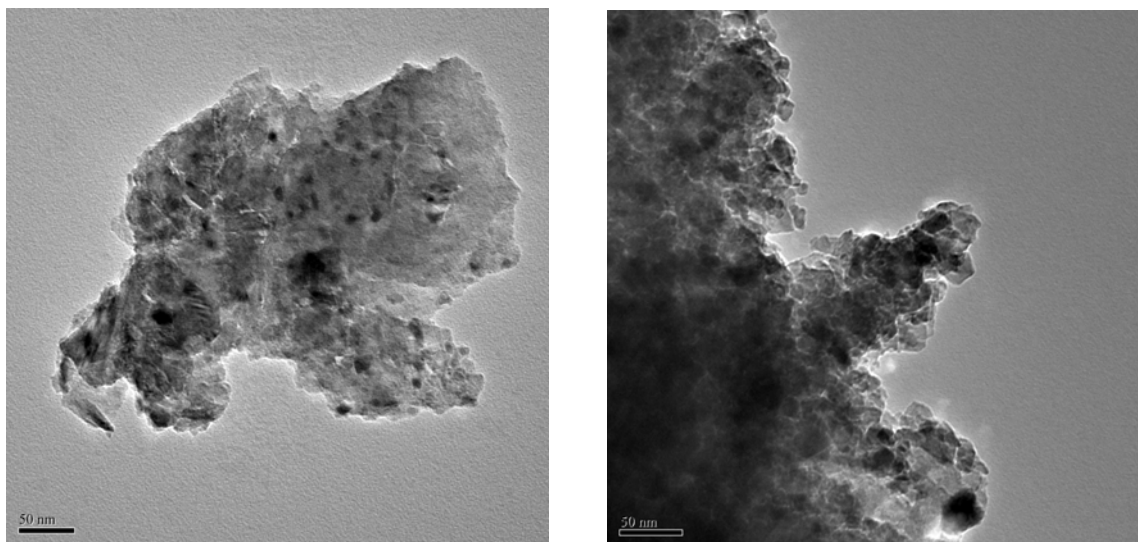


Fig. 55. TEM images of films grown with (a) lower concentration (left), and (b) higher concentrations (right). Films were peeled-off the substrate to facilitate imaging.

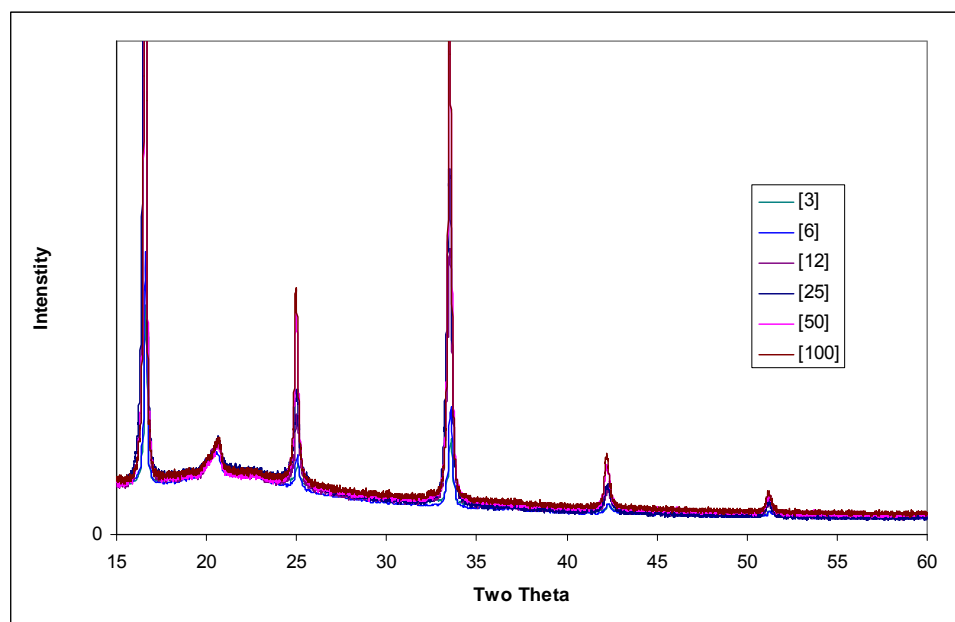


Fig. 56. XRD patterns of films deposited with different concentrations of precursors.

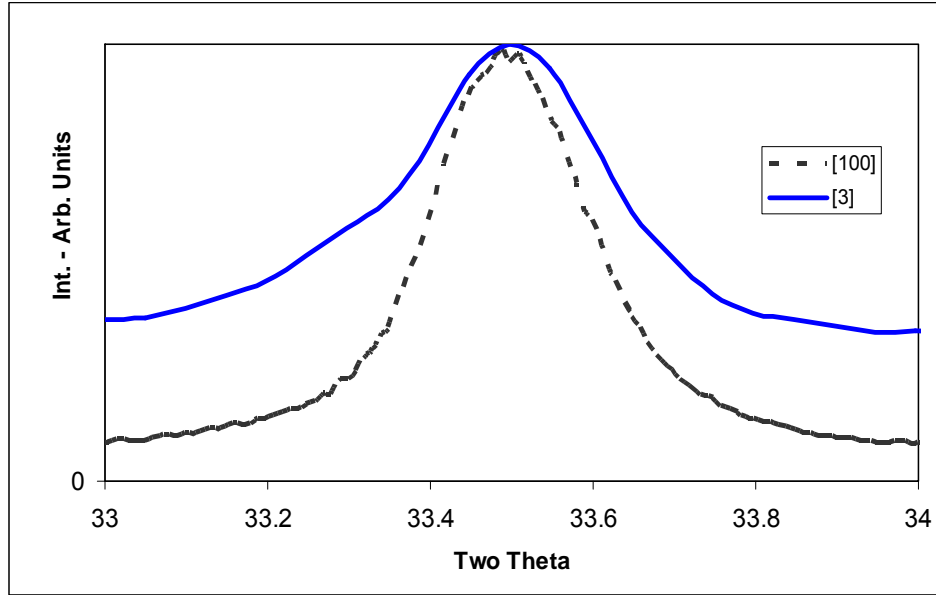


Fig. 57. Comparison of the widths of (400) XRD peaks at 25° for films deposited with high and low precursor concentrations.

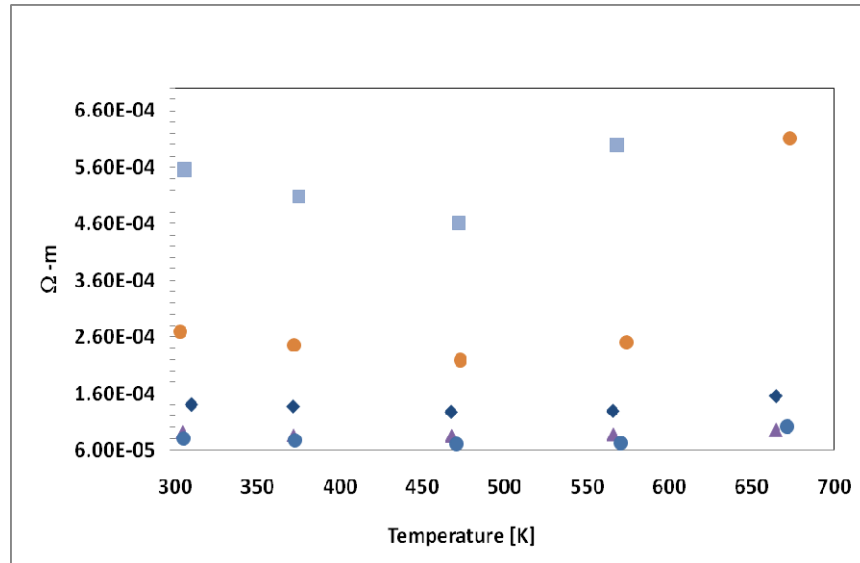


Fig. 58. Resistivity of films grown with different concentrations. . Colors and shapes refer to: Light blue square = 3, Orange circle = 6, Blue diamond = 25, Violet diamond = 50, and Blue circle = 100.

versus temperature difference curve measured by two thermocouple probes. To avoid possible oxidation, the measurement was carried out in a helium atmosphere. The accuracy of electrical resistivity and Seebeck coefficient measurements were 4 and 7%, respectively. The resistivity plots of the films are shown in Figure 58. The resistivity

decreases significantly with higher concentrations used, which correlates to larger nanoparticles incorporated in the composite films. Overall, the resistivity of the samples changed over 2 orders of magnitude. It can be seen in the inset figure that the smallest concentration was not measured over the whole range, due to the sample resistivity increasing with temperature to beyond the range of the measurement instrument.

The Seebeck coefficients of the films are shown in Figure 59. The Seebeck coefficient decreased inversely with the concentration which reflected the incorporation of larger particles. The trend, though evident, showed relatively small changes, with exception of the most resistive films, which showed large increases in the Seebeck coefficient.

Figure 60 presents the dependence of power factor on temperature for the nanoparticles films. The power factor followed the same trend as the resistivity, in that the most conductive films resulted in the highest power factors. The value of the power factors seen here for the highest concentration films, that is those greater than $200 \mu\text{W}/\text{mK}^2$, meet or exceed those prepared by using other one-step processes.

The growth of $\text{Ca}_3\text{Co}_4\text{O}_9$ and characterization of nanocomposite thin films using a microwave plasma assisted spray deposition technique has been demonstrated for the first time. The films containing larger crystals had the most desirable properties with regard to a large power factor. Films with highest power factor corresponded to higher conductivities. Typically, higher carrier densities lead to lower Seebeck coefficients. Even though the Seebeck coefficient was seen to decrease with increasing conductivity of these nanoparticle films, decrease is not very drastic to lower the power factor significantly. This may be due to scattering of low energy carriers at the multitude of boundaries that possibly can enhance the Seebeck coefficient.

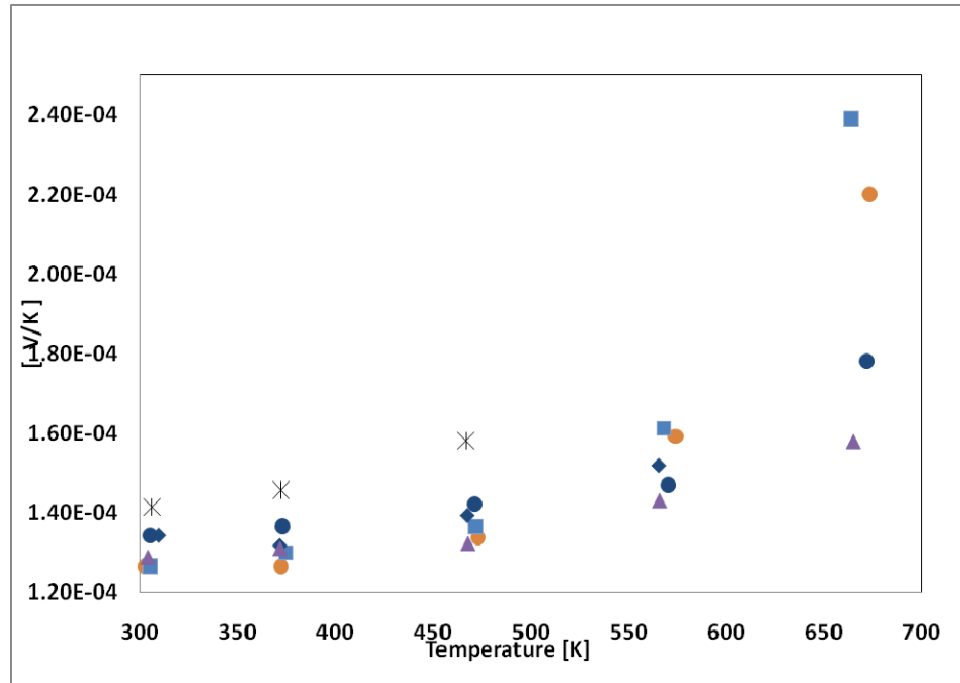


Fig. 59. Seebeck coefficient of grown films. Colors and shapes refer to: Violet star = 0.75, Light blue square = 3, Orange circle = 6, Blue diamond = 25, Violet diamond = 50, and Blue circle = 100.

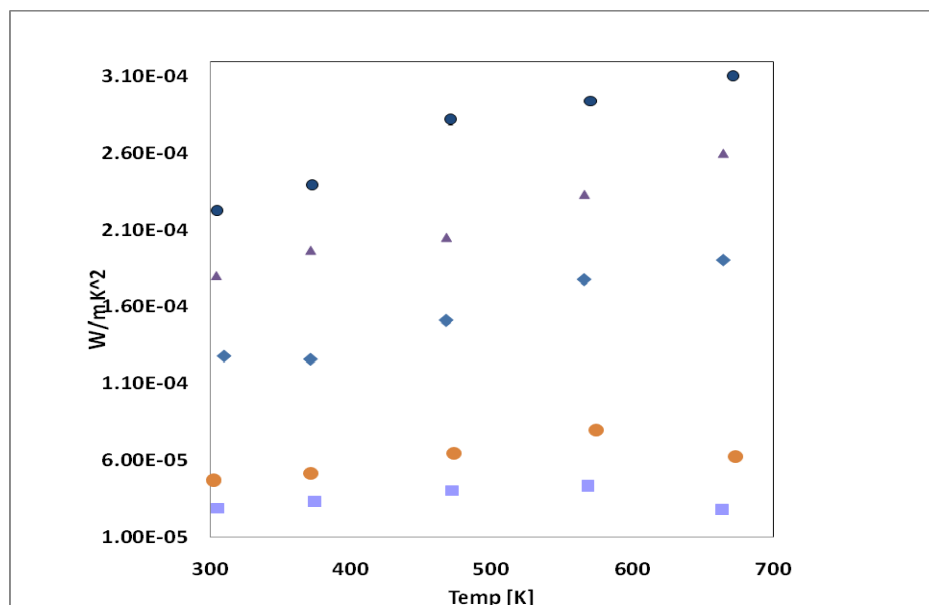


Fig. 60. Power Factor of films grown with different concentrations. Colors and shapes refer to: Violet star = 0.75, Light blue square = 3, Orange circle = 6, Blue diamond = 25, Violet diamond = 50, and Blue circle = 100.

High Performance nanofabricated thermoelectric materials for power generation

This year we focused on the following major aspects of the research tasks scheduled in the timeline of the proposal:

- (1) Structural and Calorimetric Analysis for Thermal Stability Tests of Bi and Bi-Sb Alloy Nanocrystals and Low Temperature Transport Studies of Bi and Bi-Sb Nanocomposites for Cryogenic Thermoelectric (TE) Applications; and
- (2) Core-Shell Approach Towards Optimization.

Bi and BiSb alloys:

We prepared Bi and Bi-Sb nanocrystals with different Sb concentrations by a low temperature polyol synthesis process [84]. Bismuth nitrate pentahydrate ($(\text{Bi}(\text{NO}_3)_3 \cdot 5\text{H}_2\text{O})$) was used as the Bi source, antimony trichloride (SbCl_3) was used as the antimony source, and Polyvinylpyrrolidone (PVP; Molecular Weight 40000) was used as the complexing and capping agent. Sodium borohydride (NaBH_4) was used as the reducing agent. Initially, 3 mM $\text{Bi}(\text{NO}_3)_3 \cdot 5\text{H}_2\text{O}$ and required SbCl_3 were dissolved along with 1 gm PVP in 100 mL EG until a transparent solution was obtained. A separate solution was prepared by dissolving 0.04M NaBH_4 in 30 mL water. This solution was added slowly to the $\text{Bi}(\text{NO}_3)_3 \cdot 5\text{H}_2\text{O}$ and SbCl_3 solution and refluxed at 140 °C for 2 h under continuous magnetic stirring. When the nanocrystals formed the solution turned black in color. The Bi and Bi-Sb nanocrystals were separated by centrifugation. In order to precipitate the nanocrystals from EG, the reaction mixtures were diluted with ethanol and then placed in a centrifuge at 4500 rpm for ~ 15 min. The centrifugation process was

repeated several times until the supernatant liquid was clear. Any residue of PVP, $\text{Bi}(\text{NO}_3)_3 \cdot 5\text{H}_2\text{O}$, and SbCl_3 was removed from the product by continuously washing with ethanol and water. To remove the EG and PVP from the surface of the nanocrystals, and to reduce surface oxidation, ethanol was used for washing. After thorough washing, the nanocrystal specimens were dried at room temperature under vacuum for 6 - 8 h. This process yielded approximately 1.5 gram for each synthesis run. The synthesis process is scalable and economical. This method allowed for the preparation of phase pure, highly crystalline nanocrystals of 30 - 40 nm in diameter in large yield. We performed detailed structural analysis of the Bi and Bi-Sb nanocrystals by X-ray diffraction (XRD, Bruker AXS D8, Lynx Eye PSD detector), energy dispersive x-ray spectroscopy (EDS, Oxford Instruments INCAX sight), and scanning electron microscopy (SEM, JEOL JSM 6390 LV). Transmission electron Microscopy (TEM, FEI Tecnai F20 S-Twin TEM) was used to study the atomic structure of the specimens.

In order to understand the thermal stability and melting points of the specimens, we studied the Differential Thermal Analysis (DTA, TA Instruments, Q (600)). DTA measurements were carried out with ~ 0.05 gm of Bi and Bi-Sb nanocrystals in alumina crucibles in a N_2 environment. The specimens were gradually heated to 350°C at a heating rate of 5°C min^{-1} and a N_2 flow rate of 100 mL/min . Figure 62 shows the DTA spectra of the Bi and Bi-Sb specimens with melting points shown as the dips. The melting point of the Bi nanocrystals is 260°C , which is 11.4°C lower than the melting point of bulk Bi (271.4°C) [85-90]. The lower melting point of Bi nanocrystals can be related to the size of the nanocrystals [85-87]. TEM analysis of our Bi specimens revealed the nanocrystals size of 35-40 nm. The melting point for our Bi nanocrystals is in agreement with the melting point reported for ~ 30 nm Bi [86]. With increasing Sb concentration in the Bi-Sb alloy, the melting point shifted towards higher temperatures (Figure 61). The thermograms for $\text{Bi}_{1-x}\text{Sb}_x$ were characterized by one endothermic peak with no other observed events. The shift in the melting point towards higher temperatures with increasing Sb concentration was also observed in bulk Bi-Sb semiconducting alloys and were within the range of 284°C to 301°C , depending on the alloy composition [89]. Our $\text{Bi}_{1-x}\text{Sb}_x$ nanocrystals also showed a lowering in melting point compared to these bulk values. For these $\text{Bi}_{1-x}\text{Sb}_x$ nanocrystal specimens, there was no observed secondary endotherm in the DTA spectra, suggesting these nanocrystals are stoichiometrically homogeneous.

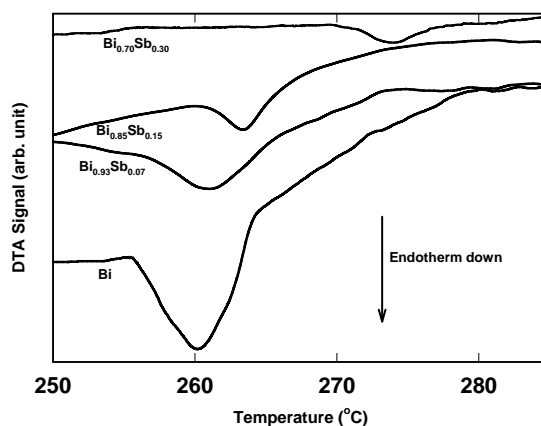


Fig. 61. DTA spectra of Bi and different compositions of Bi-Sb alloys.

After phase characterizations we prepared the Bi and Bi-Sb nanocomposites by densifying the as-synthesized nanocrystals by spark plasma sintering (SPS). In the SPS procedure, a pulsed dc current passes through both the graphite die and the specimen under pressure. This heats the specimen internally, providing uniform and rapid thermal ramping while minimizing the sintering time and temperature. At the same time rapid grain growth during a normal sintering process can be minimized using SPS process. However, different temperature and pressure of SPS may result in difference in density of the prepared bulk polycrystalline specimens. All the SPS densification runs were done at 65 MPa under vacuum. Due to the low melting points of the Bi and Bi-Sb nanocrystals (between 260 °C – 275 °C), 250 °C and 265 °C were chosen to densify Bi and Bi-Sb, respectively, with a 5 - 12 min hold time for different compositions. We densified Bi nanocrystals in three different SPS conditions; (I) 260 °C at 60 MPa with 12 min hold time, (II) 255 °C at 70 MPa with 12 min hold time, and (III) 210 °C at 400 MPa with 5 min hold time, hereby referred as Bi-I, Bi-II and Bi-III, respectively. Due to the low melting points of the Bi nanocrystals, 260 °C was chosen as the maximum SPS temperature. About 78 %, 85 %, and 92 % of the bulk theoretical densities were achieved for specimens Bi-I, Bi-II, and Bi-III, respectively. In case of Bi-Sb nanocomposites a density of only 72 % of the theoretical bulk density was achieved. The low temperature TE properties of single crystal and polycrystalline Bi and Bi-Sb bulk materials were reported to be greatly dependent on the purity of the specimens and orientation of the grains or crystals in case of single crystals. For nanostructured TE materials, densification is an essential processing step in order to make bulk polycrystalline specimen for TE properties measurements and also for practical TE applications. Electronic and thermal transport properties of TE materials are affected by the porosity in the polycrystalline bulk specimens. However, an investigation of the dependence of density on the transport properties in nanostructured TE materials such as in Bi has not been previously performed. We investigated the low temperature resistivity, ρ , Seebeck Coefficient, S , and thermal conductivity, κ properties of the prepared polycrystalline bulk specimens as described in this report.

The XRD of the densified specimens indicated phase purity of the specimens after SPS. Typical XRD spectra of a Bi and Bi₈₅Sb₁₅ nanocomposites are shown in Figure 62a. Figure 62b

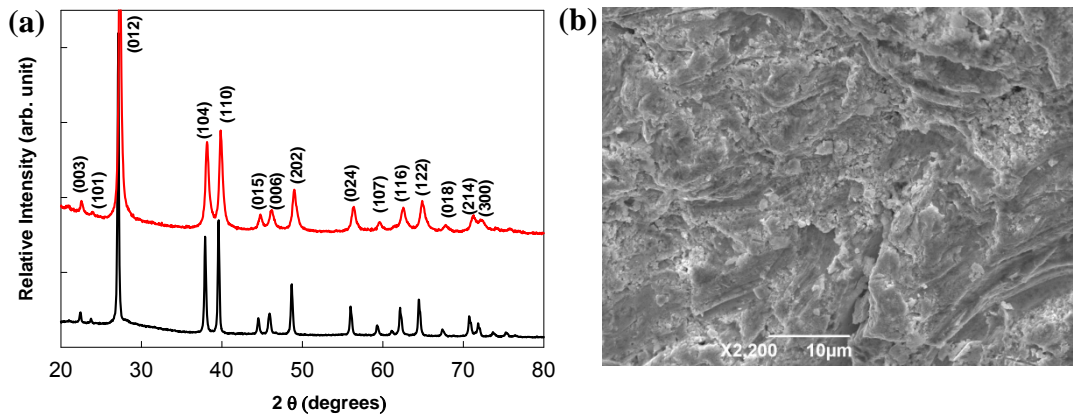


Fig. 62. (a) XRD spectra of Bi (in black) and Bi-Sb(85:15) (in red) nanocomposites. (b) A representative SEM image of Bi and Bi-Sb nanocomposites showing the presence of nanostructures after SPS.

shows a representative SEM image of the fractured surface of $\text{Bi}_{85}\text{Sb}_{15}$ nanocomposite. The SEM image indicates that after SPS the bulk polycrystalline specimen retains the nanostructural features.

The XRD of the Bi nanocrystals and SPS densified specimens are shown in Figure 63a. The XRD spectra indicated the presence of few percentages of secondary Bi_2O_3 phase in densified specimens as indicated by an asterisk (*) in Figure 63a. The impurity phase increases with higher density and is more prominent in the Bi-III specimen. Some preferred c-axis orientation was also observed in the XRD spectrum of Bi-III specimen. A SEM image of the Bi nanocrystals before SPS is shown in Figure 63b. The composition of the Bi nanocrystals was studied by EDS as shown in Figure 63c. Figures 63d and 63e show the SEM images of the fractured surfaces of the Bi-I and Bi-III dense polycrystalline bulk specimens, indicating the preservation of nanostructuring after SPS. The higher percentage of porosity in Bi-I specimen compared to the Bi-III specimen are in accordance with the density measured in these specimens. Figure 3e also indicates that at high SPS pressure Bi-III specimens retains the nanostructures more uniformly than in Bi-I specimen where grain growth increased.

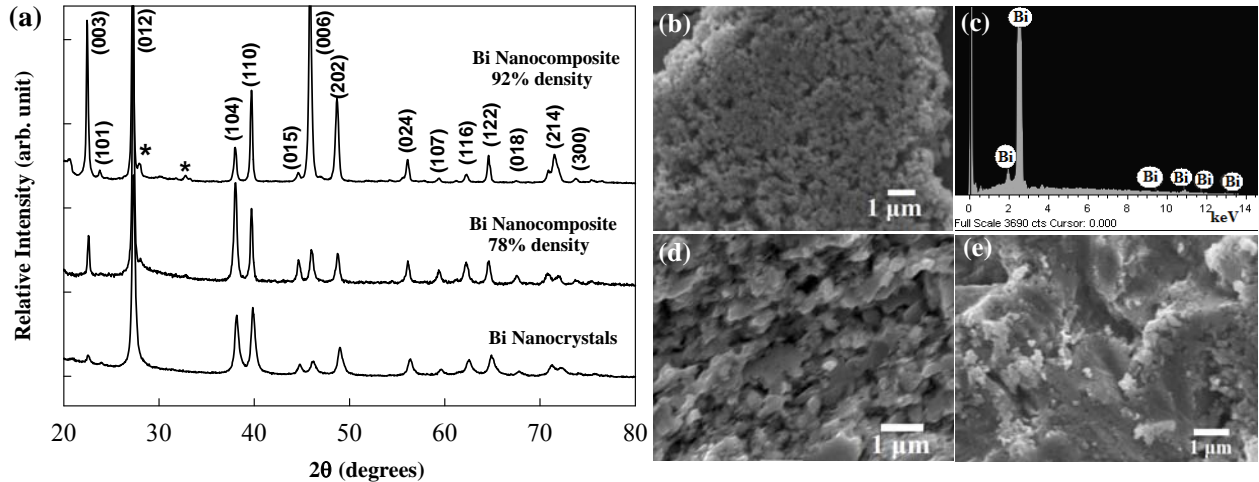


Fig. 63. (a) XRD spectra of Bi nanocrystals, polycrystalline bulk Bi nanocomposite of different densities prepared by densifying Bi nanocrystals at different SPS conditions. (*) indicates the presence of Bi_2O_3 phase in nanocomposite specimens. Relatively intense (003) and (0006) planes present in 92 % dense Bi nanocomposite specimen suggests some preferred c-axis orientation. (b) and (c) are SEM image and EDS spectrum of phase pure Bi nanocrystals prepared by polyol synthesis process. (d) and (e) are the SEM images of polycrystalline bulk Bi nanocomposites of 78 % and 92 % densities, respectively.

Bulk polycrystalline specimens were cut into 2 mm x 2mm x 5mm parallelepipeds for low temperature transport measurements [90]. Four-probe ρ , steady-state S and κ (gradient sweep method) measurements on $2 \times 2 \times 5 \text{ mm}^3$ parallelepipeds from 12 K to 300 K were conducted in a

custom radiation-shielded vacuum probe with uncertainties of 4 %, 6 %, and 8 %, respectively [90]. Figures 64a – 64c show the low temperature ρ , absolute S ($|S|$), and κ properties, respectively for Bi-I, Bi-II, and Bi-III nanostructured bulk. The results are also compared to the bulk polycrystalline specimens [91], and single crystal data both in perpendicular and parallel to the trigonal axis [92]. As Bi is anisotropic in crystal structure (crystallizes in rhombohedral symmetry) distinct orientation dependent low temperature transport properties are observed in Bi single crystals [92]. However, in the Bi nanostructured bulk specimens the orientation of the grains are random and the transport properties may be an average effect of the transport properties in all directions.

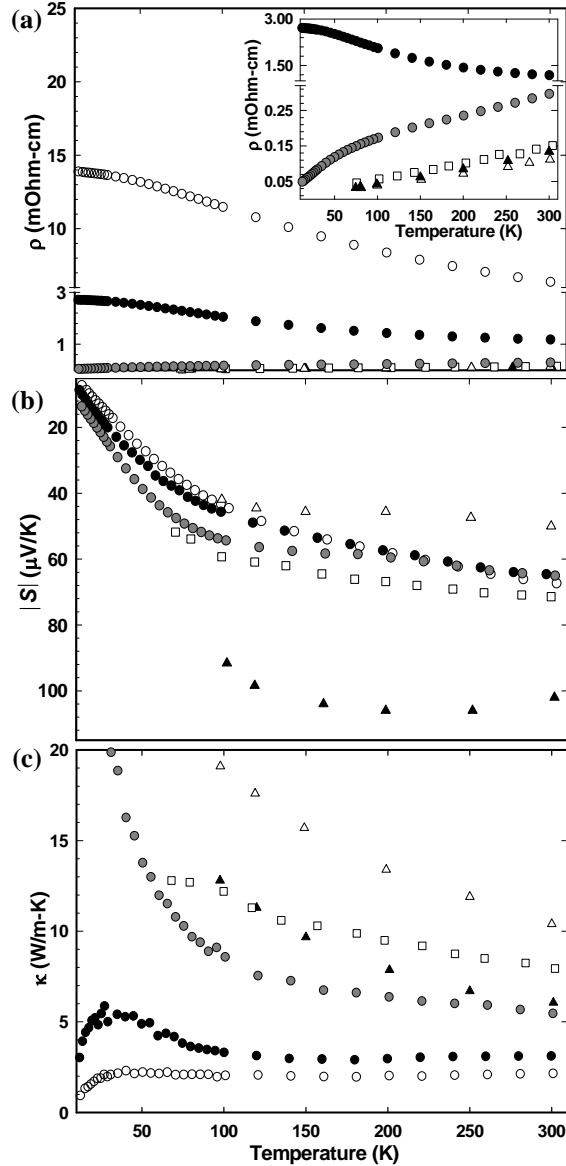


Fig. 64. (a)-(c) are the low temperature ρ , S , and κ of Bi nanocomposites with 78 % (○), 85% (●) and 92% (◐) relative theoretical densities. The data is shown in comparison to the low temperature transport properties reported for bulk Bi single crystals (Δ = perpendicular to trigonal axis [92], \blacktriangle = parallel to trigonal axis [92]) and Bi polycrystals (\square) [85].

The Bi-I and Bi-II specimens show an increase in ρ with decreasing temperature, atypical of metals (Figure 64a). However, in the case of Bi-III, ρ decreases with decreasing temperature. The inset to Figure 64a shows the temperature dependencies of ρ for the Bi-II and Bi-III specimens in comparison to that of bulk specimens. The ρ values for the nanocomposites are several times higher than that in the bulk specimens. However, for the least porous specimen, Bi-III specimen, the ρ values decreased (inset of Figure 64a). The anomalous temperature dependence in Bi-I and Bi-II specimens may be related to the presence of large percentages of porosity. It may also be related to the presence of Bi_2O_3 impurity phase [94]. Low temperature S values were comparable to that of the bulk (Figure 64b). Due to the nanostructuring in the Bi our polycrystalline bulk specimens, the κ values are lower than that of single crystals and bulk specimens. It is clear that the transport properties of Bi the nanocomposite specimens are greatly affected by the presence of porosity in the specimens. Our preliminary study on Bi nanostructured bulk specimens with different densities is a step forward to get a fundamental understanding on the processing dependencies of TE properties in the state-of-art TE materials. We emphasize that the TE properties may be controlled in some material systems by adjusting the densification parameters, as has been shown here.

Our preliminary transport data on Bi and Bi-Sb nanocomposites indicates this approach may be of interest for improved performance of materials for thermoelectric refrigeration. In continuation of this work our next aim is to achieve higher density for Bi and Bi-Sb nanostructured bulk specimens by varying the SPS parameters that may further allow enhancement in the TE properties in Bi and Bi-Sb systems. Also similar investigation will be carried out in other important TE materials systems.

Core-Shell

We successfully prepared PbTe/Ag core/shell crystals and employing spark plasma sintered (SPS) crystals in order to prepare nanocomposites. The core and core/shell nanocrystals were characterized by SEM, EDS, and TEM. Figure 65a and 65b are the representative images of 250 core/shell PbTe/Ag nanocrystals before and after SPS, respectively, and Figure 65c and 65d are representative images of EDS spectra of core and core/shell nanocrystals, respectively. After SPS, the PbTe/Ag core/shell nanocomposites were grinded to powder and TEM analysis was performed. TEM images shown in Figure 66a and 66b indicate the formation of Ag shell around the PbTe nanocrystals. This morphology appears to remain after SPS, i.e. the Ag shell remains attached to the PbTe nanocrystals. In order to understand the effect of Ag shell in the composites room temperature S and ρ were performed. As compared to the ρ value of PbTe core (101 m Ω -cm), the core/shell nanocomposites have 5 times higher resistivity. These results indicate that this approach may not be of interest for improved thermoelectric performance.

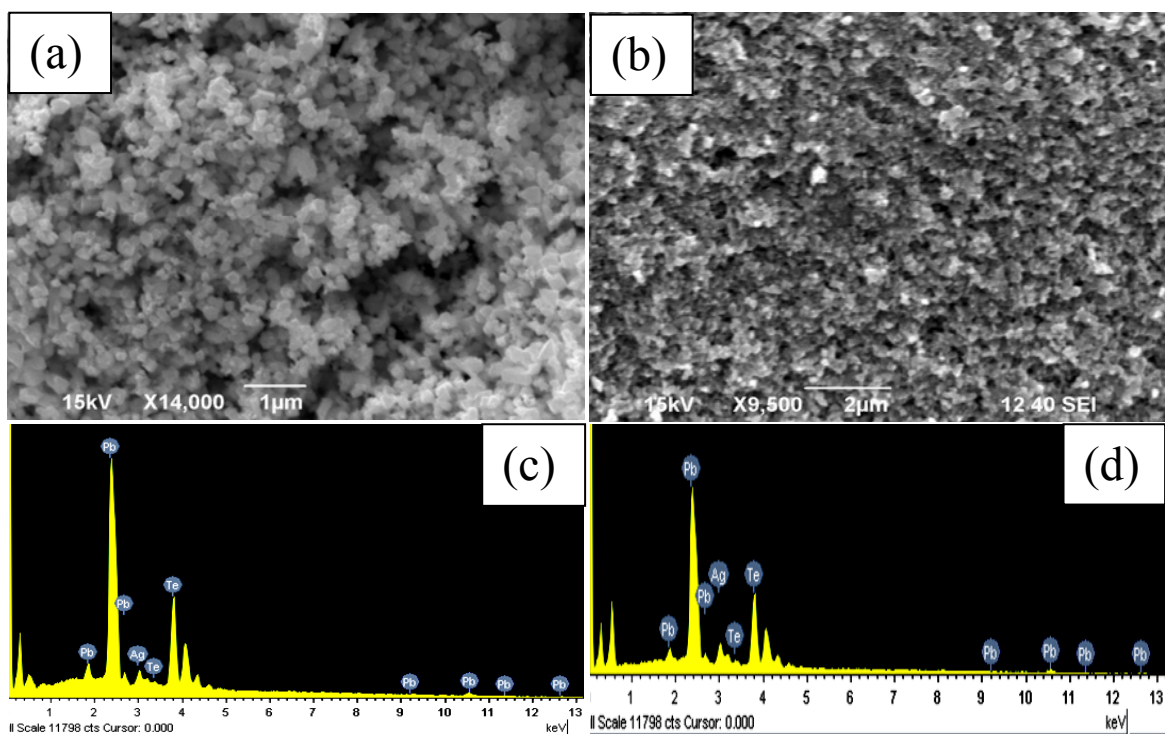


Fig. 65. SEM images of PbTe/Ag core/shell crystals (a) before and (b) after the SPS. EDS spectra of (a) PbTe and (b) PbTe/Ag core/shell crystals.

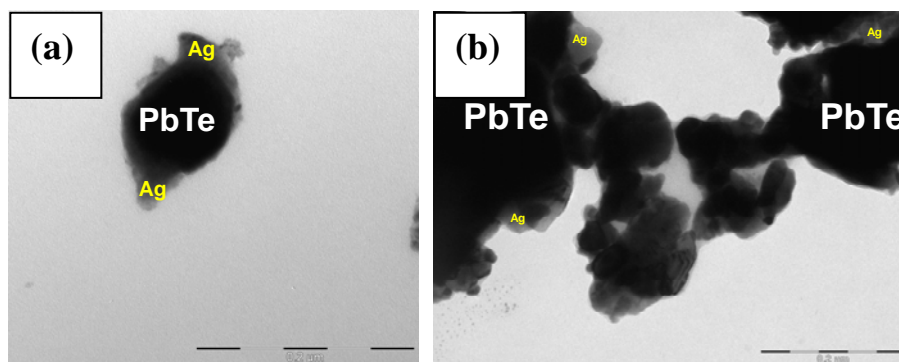


Fig. 66. TEM images of (a) PbTe/Ag nanocrystals and (b) ground PbTe/Ag after SPS.

Clathrate Nanocomposites for Dual Functional Thermoelectric and Thermomagnetic Cooling Applications

Infrared (IR) detectors are widely used in night vision, thermal imaging and threat detection systems for many military and space applications [93]. While conventional thermoelectric coolers work well down to 150 K, there is a need for cooling further to 80 K and below to improve the efficiency of IR detectors. This underscores the need for considering new materials and strategies for developing efficient solid-state coolers with a broad range in working temperature. While $\text{Eu}_8\text{Ga}_{16}\text{Ge}_{30}$ clathrates are usually known as excellent thermoelectric refrigerants at high temperature ($T > 200$ K), our recent discoveries of large, reversible magnetocaloric effects in these materials make them interesting for dual functional thermomagnetic and thermoelectric cooling applications [94,95]. The goal of our research is to use $\text{Eu}_8\text{Ga}_{16}\text{Ge}_{30}$ clathrates as the host matrix to make nanocomposites with tunable refrigerant capacity (RC) in the low to intermediate temperature range (10 - 100 K).

Experiment:

Polycrystalline $\text{Eu}_8\text{Ga}_{16}\text{Ge}_{30}$ with the type I crystal structure was synthesized by reacting the high purity elements in stoichiometric ratios inside a boron nitride (BN) crucible which was

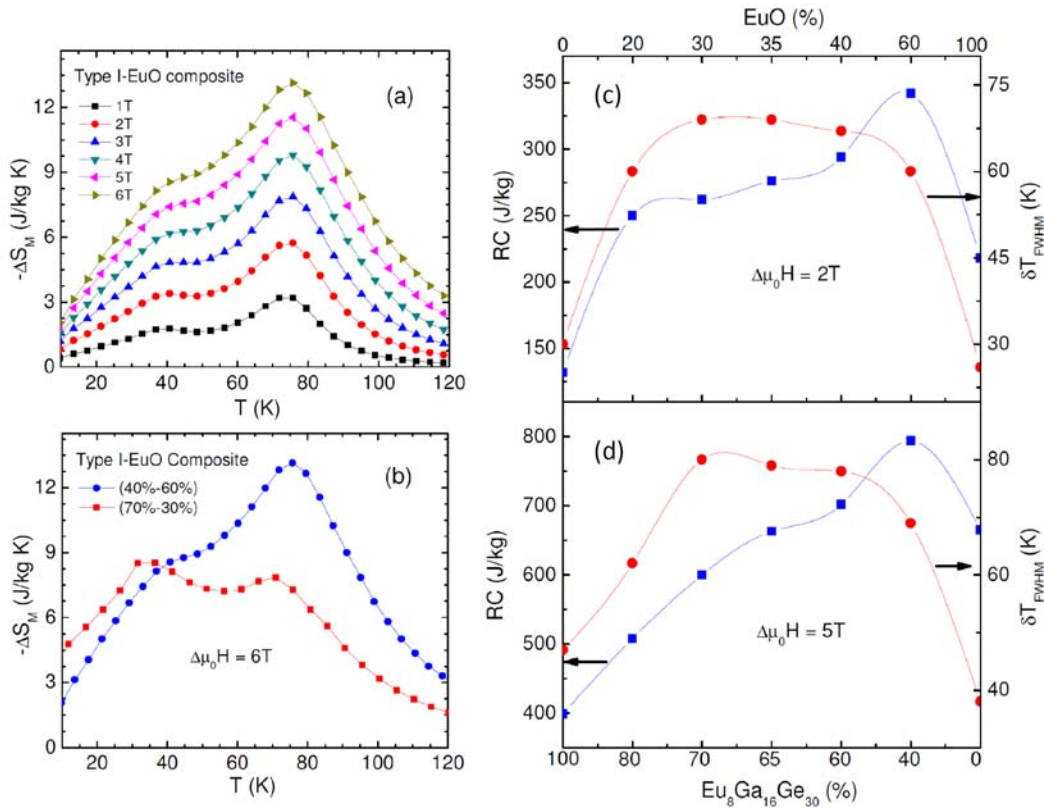


Fig. 67 (a) The temperature dependence of $-\Delta S_M$ (a) for different field changes up to 6 T for the Type I clathrate-EuO (40%-60%) composite and (b) for a field change of 6 T for the Type I clathrate-EuO (40%-60%) and (70%-30%) composites; (b) The refrigerant capacity (RC) and the temperature interval (δT_{FWHM}) vary with the clathrate/EuO ratio.

enclosed in a nitrogen atmosphere, inside a sealed quartz ampoule. The specimen was placed in an induction furnace at 1000 °C for 10 minutes followed by a rapid water quench. To make the clathrate-based composites, the type-I clathrates are combined with EuO at different portions (80%/20%, 70%/30%, 65%/35%, 60%/40%, 40%/60%). The samples were structurally characterized by XRD and their magnetic and magnetocaloric properties were studied using PPMS. Magnetic measurements were conducted using a Physical Property Measurement System from Quantum Design. In our study, the magnetic entropy change (ΔS_M) of the samples was calculated from a family of the M-H isotherms using the Maxwell relation, $\Delta S_M = \mu_0 \int (\partial M / \partial T)_H dH$, where M is the magnetization, H is the magnetic field and T is the temperature. The refrigerant capacity (RC) was calculated as $RC = [-\Delta S_M]_{\max} \times \delta T_{FWHM}$, where δT_{FWHM} is the full width at half maximum of the $\Delta S_M(T)$ curve.

Results and Discussion

Fig. 67a,b shows the temperature dependence of $-\Delta S_M$ for different applied field changes up to 6 T for the type I clathrate-EuO (40%-60%) composite and for the same field change of $\mu_0 \Delta H = 6$ T for the type I clathrate-EuO (40%-60%) and (70%-30%) composites. It is interesting to note that the large ΔS_M has been achieved over a wide temperature range in these composites. This is very beneficial for enhancing the cooling efficiency. More interestingly, the combination of the type I clathrates with EuO at appropriate portions can produce novel composites with enhanced RC for active magnetic refrigeration (AMR) around 70 K. Fig. 67c,d shows the variation in RC and FWHM with the portion of EuO and $\text{Eu}_8\text{Ga}_{16}\text{Ge}_{30}$ for the field change of 2 T and 5 T. We have achieved a very large RC of 794 J/kg at 5 T over a temperature interval of 70 K in the clathrate type I – EuO (40%-60%) composite, which is the largest value ever achieved among the existing materials for magnetic refrigeration around 70 K. This composite is particularly attractive for AMR for nitrogen liquefaction.

Overall, we have demonstrated the possibility of combining type I clathrates with other magnetocaloric materials such as EuO at appropriate portions to produce nanocomposites with enhanced and tunable refrigerant capacity for active magnetic refrigeration applications. We are investigating the possibility of combining the type VIII clathrate – EuO composite to produce refrigeration in two different temperature ranges for functional cooling applications. These results have been accepted for publication in *Applied Physics Letters*, 2011.

III. Reportable Outcomes

Publications and presentations in the 2010-2011 duration acknowledging support from CIFM through grant USAMRMC W81XWH-07-1-0708 (Participating CIFM researcher contributors are shown in bold):

Book chapters:

1. **K. Stojak, H. Srikanth, P. Mukherjee, M.H. Phan** and N.T.K. Thanh, Size- and Shape-Variant Magnetic Nanoparticles: Synthesis and Characterization for Biomedical Applications, in **Metal Nanoparticles of Complex Morphologies, Bottom-up Synthesis to Applications**, (2012) Ed Tapan K. Sau and Andrey L. Rogach. Wiley, Chapter 6.

Journal Publications:

2. “Polymer nanocomposites exhibiting magnetically tunable microwave properties” -**K. Stojak, S. Pal, H. Srikanth**, C. Morales, J. Dewdney, J. Wang, T. Weller, Nanotechnology **22**, 135602 (2011).
3. “Enhanced GMI effect and field sensitivity in Co-coated soft ferromagnetic amorphous ribbons” - **N. Laurita, A. Chaturvedi**, C. Bauer, P. Jayathilaka, Alex Leary, C. Miller, **M.H. Phan**, M.E. McHenry and **H. Srikanth**, Journal of Applied Physics **109**, 07C706 (2011).
4. “Giant magnetoimpedance and field sensitivity in amorphous and nanocrystalline ($\text{Co}_{1-x}\text{Fe}_x$)₈₉Zr₇B₄ ($x = 0, 0.025, 0.05, 0.1$) ribbons” -**A. Chaturvedi, N. Laurita**, A. Leary, **M.H. Phan**, M.E. McHenry and **H. Srikanth**, Journal of Applied Physics **109**, 07B508 (2011).
5. “Magnetic switching and magnetic transitions in ErCo₂ probed by radio frequency transverse susceptibility” -A.I. Figueroa, **S. Chandra, M.H. Phan, H. Srikanth**, C. M. Bonilla, L.M. García, F. Bartolomé, J. Bartolomé, and J. Herrero-Albillos, Journal of Applied Physics **109**, 07E118 (2011).
6. “Critical length and giant magnetoimpedance in Co-Fe-Ni-Si-B amorphous ribbons” -**A. Chaturvedi**, A.-T. Le, **M.H. Phan** and **H. Srikanth**, Materials Science and Engineering B **172**, 146 (2010)
7. “Correlation between magnetic softness, sample surface and magneto-impedance in Co₆₉Fe_{4.5}X_{1.5}Si₁₀B₁₅ (X = Ni, Al, Cr) amorphous ribbons” - **A. Chaturvedi, T. Dhakal**, A.-T. Le, **M.H. Phan** and **H. Srikanth**, Physica B: Condensed Matter **405**, 2836 (2010)
8. “Origin of the magnetic anomaly and tunneling effect of europium on the ferromagnetic ordering in Eu₈Ga₁₆Ge₃₀ type I clathrates” -**M. H. Phan**, V. Franco, **A. Chaturvedi**, S. Stefanoski, **G. S. Nolas** and **H. Srikanth**, *Physical Review B* **84**, 054436 (2011).
9. “Growth of uniform ZnO nanoparticles by a microwave plasma process”, **T. Wangenstein, T. Dhakal, M. Merlak, P. Mukherjee, M. H. Phan, S. Chandra, H. Srikanth, S. Witanachchi**, J. Alloys & Compounds **509**, 6859 (2011).

10. "Table-like magnetocaloric effect and enhanced refrigerant capacity in $\text{Eu}_8\text{Ga}_{16}\text{Ge}_{30}$ -EuO composite materials" - **A. Chaturvedi, S. Stefanoski, M.H. Phan, George S. Nolas, and H. Srikanth**, Applied Physics Letters, 2011 (in press).
11. "Fabrication and magnetic response probed by RF transverse susceptibility in $\text{La}_{0.67}\text{Ca}_{0.33}\text{MnO}_3$ nanowires" **S. Chandra**, A. I. Figueroa, Barnali Ghosh, A. K. Raychaudhuri, **M.H. Phan, P. Mukherjee, and H. Srikanth**, Physica B: Condensed Matter, 2011 (accepted).
12. "Transverse susceptibility as a biosensor for detection of nanoparticle-embedded human embryonic kidney cells" -**N. A. Frey-Huls, M. H. Phan**, A. Kumar, S. Mohapatra, S. S. Mohapatra, **P. Mukherjee and H. Srikanth**, Biosensors and Bioelectronics (under review)
13. "Au- Fe_3O_4 Composite Nanoparticles: Origins of Exchange Bias and Interfacial Coupling" -**N. A. Frey-Huls, M. H. Phan**, S. Srinath, **S. Chandra, H. Srikanth**, M. A. Garcia, Y. Lee, C. Wang, S. Sun and O. Iglesias, Nature Communications (submitted)
14. "Carbon nanotube-based gas sensors using the magnetoimpedance effect" -**A. Chaturvedi, N. Laurita, P. Mukherjee, H. Srikanth, and M.H. Phan**, Journal of Applied Physics (submitted)

Conference Presentations:

1. "Giant magnetoimpedance in magnetic nanoparticles patterned Co-based amorphous ribbons for biosensing applications" - **L. Nicholas, A. Chaturvedi, K. Stojak, S. Chandra, M. H. Phan, H. Srikanth**, the APS March Meeting, March 21 - 25, 2011, Dallas, Texas (Oral presentation)
2. "Correlation between magnetic softness, sample surface and magnetoimpedance in $\text{Co}_{69}\text{Fe}_{4.5}\text{X}_{1.5}\text{Si}_{10}\text{B}_{15}$ (X = Ni, Al, Cr) amorphous ribbons" - **A. Chaturvedi, T. Dhakal, S. Witanachchi, M.H. Phan, H. Srikanth**, and A.T. Le, the APS March Meeting, March 21 - 25, 2011, Dallas, Texas (Oral presentation)
3. "Synthesis and characterization of graphene patterned with Fe_3O_4 nanoparticles" - **S. Chandra, K. Stojak**, D. Ferizovic, M. Munoz, **M. H. Phan and H. Srikanth**, the APS March Meeting, March 21 - 25, 2011, Dallas, Texas (Oral presentation)
4. "Enhanced magnetoimpedance effect in $\text{Co}_{89}\text{Zr}_7\text{B}_4$ ribbon/ $\text{Fe}_{80}\text{Ni}_{20}$ bilayer structures" - **N. Laurita, A. Chaturvedi**, A. Leary, P. Jayathilaka, C. Bauer, **Casey W. Miller, M.H. Phan**, M.E. McHenry, **H. Srikanth**, the Symposium on Magnetic Materials for Energy Applications, February 27 to March 3, 2011, San Diego, California, USA (Oral presentation)

Invited Talks:

"Magnetocaloric effect in oxide nanostructures" - **H. Srikanth and M. H. Phan**, the Symposium on Magnetic Materials for Energy Applications, February 27 to March 3, 2011, San Diego, California, USA

H. Srikanth, Multifunctional Materials Workshop organized by DoD agencies, Kodiak, Alaska (July 31 - Aug03, 2011)

H. Srikanth, Magnetic nanostructures, CSIC, University of Autonomia – Madrid, Spain (May 30, 2011)

H. Srikanth, Cavendish Lab, Cambridge University, UK (June 6, 2011)

H. Srikanth, Physics Department, Imperial College, London UK (June 7, 2011)

H. Srikanth, Invited Speaker, Soft Magnetic Materials (SMM 20) Conference, Kos Island, Greece (September 2011)

‘A Bottom-Up Approach for Nanostructured Thermoelectrics’, **G.S. Nolas**, 9th European Conference on Thermoelectrics, Thessaloniki, Greece, September 30, 2011.

‘New Synthesis Techniques and Strategies for Materials Research towards Solid-state Power Conversion and Refrigeration Applications’, **G.S. Nolas**, Seminar for Inorganic Chemistry, Max-Planck Institute for Chemical Physics of Solids, Dresden, Germany, March 18, 2011.

‘Bottom-Up Strategy For Thermoelectric Nanocomposites’, **A. Datta**, American Physical Society Annual Meeting, Dallas, Texas, March 22, 2011.

‘Synthesis strategies and properties of nanostructures for optical, thermoelectric and sensing applications’, **A.Datta**, the Florida Cluster for Advanced Smart Sensor Technologies (FCASST) in the Department of Physics, University of South Florida, August 9, 2011.

IV. Conclusion

Update on Milestones:

- Studies of magnetic and hydrodynamic properties of bio-functionalized ferrofluids under flow conditions.

Magnetic properties of bio-functionalized ferrofluids have been completed and were presented in the last annual report. The hydrodynamic properties under flow conditions are being investigated by combining this task with “Synthesis of PEG, Dextran coated nanoparticles and clusters for hyperthermia experiments and their structural and magnetic characterization”. This study is in progress.

- Biosensor fabrication using carbon nanotube arrays and evaluating the potential to sense different analytes adsorbed to the surface.

Investigation of gas sensors based on carbon nanotubes and biosensors based on functionalized magnetic nanoparticles have been completed and presented in this report. In addition to carbon nanotubes, $\text{La}_{0.5}\text{Sr}_{0.5}\text{MnO}_3$ nanowires have also been investigated as a possible multifunctional sensor (results are presented in this report).

- Synthesis and characterization of InSb nanoparticles.
- Fabricate InSb-polymer hybrid solar cell structures and compare the performance with PbSe based devices

Synthesis of InSb quantum dots has not been successful. PbSe quantum dots are still the most efficient material for solar absorption to generate excitons. We have combined the two tasks to investigate multi-exciton generation and dissociation in PbSe QD by a femtosecond pump-probe technique. This study is under way.

Project Milestones for Proposal:

The following tables identify the milestones and timeline for each of the seven projects in the continuing proposal. The additional work for the three years of continuation, of which this is the end of the first year (Year 4 of project), is italicized and the timelines (for each project) are indicated. Green bars indicate accomplished work while the yellow bars indicate the tasks that have been changed or merged based on the results. This rearrangement is based on the considerations described in the update on third-year milestones:

Task I: Nanostructured materials for biomedical diagnostics and chemical sensing

Project 1: Functional magnetic fluids for biomedical applications.

RESEARCH TASKS	Year 1	Year 2	Year 3	Year 4	Year 5	Year 6
Chemical synthesis of magnetic nanoparticles and ferrofluids, Structural analysis, DC and AC magnetization studies						
Functionalization of ferrofluids with biocompatible surfactant coatings of the nanoparticles. Chemical and Physical properties characterization of the functionalized ferrofluids						
Studies of magnetic and hydrodynamic properties of bio-functionalized ferrofluids under flow conditions						
<i>Synthesis of PEG, Dextran coated nanoparticles and clusters for hyperthermia experiments and their structural and magnetic characterization</i>						
<i>Measurements and comparative analysis of specific absorption rates and AC power losses of ferrofluids for magnetic hyperthermia applications</i>						
<i>Bifunctional metal-oxide coupled and core-shell nanostructures</i>						

Project 2: Nanoparticle/nano-wire structures and polymer nanoparticles for sensing and molecular manipulation

RESEARCH TASKS	Year 1	Year 2	Year 3	Year 4	Year 5	Year 6
Synthesis and characterization of Au templates with variable spacing and formation of In nano-pore structures						
Growth of nano-wires of inorganic compounds with variable diameters.						
Formation of polymer nano-templates						
Manipulation of molecules using electrical stimulation						
Molecular dynamics simulations of structural and mechanical properties of oxide nanostructures and density functional theory studies of electronic properties of nano-wires and nano-ribbons						
<i>Development and testing of amorphous magnetic ribbons for MI-based sensing</i>						
<i>Improving the field sensitivity and figure of merit of giant magnetoelectricity (GME) materials</i>						

Project 3: Carbon-nanotube based sensors

RESEARCH TASKS	Year 1	Year 2	Year 3	Year 4	Year 5	Year 6
CVD and cluster deposition of carbon nanotube networks						
Structural, electrical, and capacitive measurements on nanotube networks						
Biosensor fabrication using carbon nanotube arrays and evaluating the potential to sense different analytes adsorbed to the surface						
Theoretical modeling and simulation of toxic absorption, external fields and mechanics on carbon nanotubes						
<i>Magnetoimpedance measurements and sensing of biomolecules</i>						
<i>Integrated ferroelectric-ferromagnetic high-aspect ratio nanostructures</i>						

Project 4: Functional materials for affecting cell proliferation and locomotion

RESEARCH TASKS	Year 1	Year 2	Year 3	Year 4	Year 5	Year 6
Magnetic nanoparticle attachment to cell membranes						
Design and fabrication of lithographically patterned metallic micro wires						
Design and fabrication of substrates with controlled nanotopography						
Study of cell migration, cell-substrate adhesion, and cell growth						
<i>Stimuli-response studies using ECIS of magnetic nanoparticle loaded cells</i>						
<i>An integrated functional materials approach to the development of an artificial Matrigel</i>						
<i>Formation and delivery of functionalized artificial platelets for rapid cessation of internal bleeding</i>						

Task II: Multifunctional composites for communication and energy applications

Project 5: Tunable multifunctional nano- and heterostructures for RF and microwave applications

RESEARCH TASKS	Year 1	Year 2	Year 3	Year 4	Year 5	Year 6
Chemical synthesis of ferrite nanoparticles and fabrication of polymer nanocomposite films, analysis of structural, electrical and magnetic properties						
PLD growth of ferroelectric/ferrite heterostructures with controlled interface strain, RF and microwave measurements of polymer composites and oxide films						
Materials growth efforts continued with piezoelectric films containing nanoparticle inclusions, experiments to study the magneto-electric and multiferroic coupled response in materials and prototype device structures						
<i>Fabricate and characterize ZnO:V, ZnO:Mn and ZnO:V/ZnO:Mn heterostructures. Investigate the multiferroic coupling in these structures</i>						
<i>Synthesis of ferroelectric-ferromagnetic nanopillar-nanoparticle structure and exploration of magnetoelectric coupling.</i>						

Project 6: Flexible photonic materials for solar-based energy sources

RESEARCH TASKS	Year 1	Year 2	Year 3	Year 4	Year 5
Synthesis and characterization of PbSe and PbS _x Se _{1-x} nanoparticles by microwave plasma					
Integration of nanoparticles with polymer and characterization of optical properties					
Formation of single cell device structures with nanoparticles of different sizes and characterization of the output					
Fabrication and evaluation of tandem structures					
Synthesis and characterization of InSb nanoparticles					
Fabricate InSb-polymer hybrid solar cell structures and compare the performance with PbSe based devices					

Task III: Solid-state materials for power generation and refrigeration

Project 7: High-performance bulk and nanocomposite thermoelectric materials for power generation

RESEARCH TASKS	Year 1	Year 2	Year 3	Year 4	Year 5	Year 6
Bulk nanocomposites: optimize synthesis parameters						
Core-shell approach towards optimization						
Structural and calorimetric analysis for thermal stability tests						
Measurement of TE properties						
Comparative studies and analysis: Synthesis bulk materials for comparison to the nano-scale TE materials						
Optimization employing the developed materials						
Device design development						
Measurement, optimization and re-development of prototype TE devices						
Theoretical modeling of conductance and thermopower of core-shell nanocomposites						
<i>Fabrication of CaCoO nanoparticle coatings by a microwave plasma process and investigation of thermoelectric properties</i>						
<i>Synthesis of bulk thermoelectrics</i>						

Relevance of the Research:

From the perspective of military applications specific to the US Army Medical Research and the DoD in general, we have identified three key targeted applications where timely advances are critically needed. The concerted effort in this Integrated Functional Materials Project and our ongoing development of an interdisciplinary Center for Integrated Functional Materials (CIFM) at USF will advance the science knowledge base in these areas. The three targeted tasks broadly encompass issues of most importance to the soldier in the battlefield. At the culmination of the projects specific advances are expected in new materials and functionalities that aid in diagnostics and communication of medical problems encountered by the soldier in the field, sensors with improved sensitivity and specificity to detect threats such as trace biological agents, and the need for novel portable and renewable energy and power sources to power these new devices.

Once established, CIFM will continue to be a national resource in the development of new materials and devices for the military and commercial sector, and a stimulant of industry in the United States based on emerging technologies and manufacturing processes. The specific outcome of the research activities is therefore expected to lead to new devices/systems/composite materials useful for the USAMRMC.

V. Bibliography

- (1) Pankhurst et al. *J. Phys. D: Appl. Phys.* **36**, R1671 (2003).
- (2) Gao et al. *Crystal Growth and Design* **10**, 2888 (2010).
- (3) D. Ung, L.D. Tung, G. Caruntu, D. Delapostas, Y. Alexandrous, I. Prior and N.T.K. Thanh, *CrystEngComm.* **2009**, *11*, 1309.
- (4) J. Gass, P. Poddar, J. Almand, S. Srinath and H. Srikanth, *Adv. Funct. Mater.* **16**, 71 (2006).
- (5) C. Morales, J. Dewdney, S. Susmita, S. Skidmore, K. Stojak, H. Srikanth, T. Weller and J. Wang, *IEEE Trans. Magn.* **1**, 1340 (2010).
- (6) Xie et. al., *Pure Appl. Chem.*, **78**, 1003 (2006).
- (7) K. Stojak, S. Pal, H. Srikanth, C. Morales, J. Dewdney, J. Wang, T. Weller, *Nanotech.* **22**, 135602 (2011).
- (8) S. Pal, S. Chandra, M.H. Phan, P. Mukherjee, and H. Srikanth, *Nanotech.* **20**, 485604 (2009).
- (9) Novoselov et al. *Science* **306**, 666 (2004).
- (10) Choi et al. *Critical Reviews in Solid State and Materials Sciences* **35**, 52 (2010).
- (11) Yu et al., *Appl. Phys. Lett.* **93**, 113103 (2008).
- (12) Krycka et al., *Phys. Rev. Lett.* **104**, 207203 (2010).
- (13) M. H. Phan and H. X. Peng, *Prog. Mater. Sci.* **53**, 323 (2008)
- (14) Ohodnicki et al., *J. App. Phys.* **104**, 113909 (2008).
- (15) Chaturvedi et al., *Mater. Sci. Engin. B* **172**, 146 (2010)
- (16) Y. Wang and John T. W. Yeow, *J. Sens.* **1**, 1 (2009).
- (17) G. V. Kurlyandskaya, *J. Magn. Magn. Mater.* **321**, 659 (2009).
- (18) Y. Tokura (Ed.), Colossal Magnetoresistive Oxides (Advances in Condensed Materials Science), vol. 2, Gordon and Breach Science Publishers, Amsterdam, 2000.
- (19) M.H. Phan and S.C. Yu, *J. Magn. Magn. Mater.* **308**, 325 (2007)
- (20) Decher, G.; Schlenoff, J. B., Eds. *Multilayer Thin Films: Sequential Assembly of Nanocomposite Materials*; Wiley-VCH: Weinheim, 2003.
- (21) Johnston, A. P. R.; Cortez, C.; Angelatos, A. S.; Caruso, F. *Curr. Op. Coll. Interface Sci.* 2006, *11*, 203-209.

- (22) Lvov, Y.; Möhwald, H., Eds. *Protein Architecture: Interfacing Molecular Assemblies and Immobilization Biotechnology*; Marcel Dekker: New York, 2000.
- (23) Kim, B. -S.; Choi, J. -W. *Biotechnol. Bioprocess Eng.* **2007**, *12*, 323-332.
- (24) Hammond, P. T. *Curr. Opin. Colloid Interface Sci.* **2000**, *4*, 430-442.
- (25) Peyratout, C. S.; Daehne, L. *Angew. Chem. Int. Ed.* **2004**, *43*, 3762-3783.
- (26) Sukhishvili, S. A. *Curr. Opin. Colloid Interface Sci.* **2005**, *10*, 37-44.
- (27) Schönhoff, M. *Curr. Opin. Colloid Interface Sci.* **2003**, *8*, 86-95.
- (28) Sukhorukov, G. B.; Fery, A.; Möhwald, H. *Prog. Polym. Sci.* **2005**, *30*, 885-897.
- (29) Hammond, P. T. *Adv. Mater.* **2004**, *16*, 1271-1293.
- (30) Ho, P. K. H.; Kim, J. S.; Burroughes, J. H.; Becker, H.; Li, S. F. Y.; Brown, T. M.; Cacialli, F.; Friend, R. H. *Nature* **2000**, *404*, 481-484.
- (31) Tang, Z. Y.; Kotov, N. A.; Magonov, S.; Ozturk, B. *Nat. Mater.* **2003**, *2*, 413-418.
- (32) Haynie, D. T.; Cho, E.; Waduge, P. *Langmuir* **2011**, *27*, 5700-5704.
- (33) Garza, J. M.; Schaaf, P.; Muller, S.; Ball, V.; Stoltz, J. F.; Voegel, J. C.; Lavalle, P. *Langmuir* **2004**, *20*, 7298-7302.
- (34) Podsiadlo, P.; Michel, M.; Lee, J.; Verploegen, E.; Kam, N. W. S.; Ball, V.; Lee, X. J.; Qi, Y.; Hart, A. J.; Hammond, P. T.; Kotov, N. A. *Nano Lett.* **2008**, *8*, 1762-1770.
- (35) Zhang, L.; Zhao, W.; Rudra, J. S.; Haynie, D. T. *ACS Nano* **2008**, *1*, 476-486.
- (36) Porcel, C.; Lavalle, P.; Ball, V.; Decher, G.; Senger, B.; Voegel, J. C.; Schaaf, P. *Langmuir* **2006**, *22*, 4376-4383.
- (37) Itoh, K.; Tokumi, S.; Kimura, T.; Nagase, A. *Langmuir* **2008**, *24*, 13426-13433.
- (38) Boulmedais, F.; Schwinte', P.; Gergely, C.; Voegel, J. -C.; Schaaf, P. *Langmuir* **2002**, *18*, 4523-4525.
- (39) Greenfield, N.; Fasman, G. D. *Biochemistry* **1969**, *8*, 4108-4116.
- (40) Picart, C.; Lavalle, P.; Hubert, P.; Cuisinier, F. J. G.; Decher, G.; Schaaf, P.; Voegel, J. C. *Langmuir* **2001**, *17*, 7414-7424.
- (41) Richert, L.; Lavalle, P.; Payan, E.; Shu, X. Z.; Prestwich, G. D.; Stoltz, J. F.; Schaaf, P.; Voegel, J. C.; Picart, C. *Langmuir* **2004**, *20*, 448-458.
- (42) Richert, L.; Boulmedais, F.; Lavalle, P.; Mutterer, J.; Ferreux, E.; Decher, G.; Schaaf, P.; Voegel, J. C.; Picart, C. *Biomacromolecules* **2004**, *2*, 284-294.
- (43) Notley, S. M.; Eriksson, M.; Wågberg, L. [*J. Colloid Interface Sci.*](#) **2005**, *292*, 29-37.

- (44) Kujawa, P.; Schmauch, G.; Viitala, T.; Badia, A.; Winnik, F. M. *Biomacromolecules* **2007**, *8*, 3169-3176.
- (45) Shouheng Sun and Hao Zeng *J. Am. Chem. Soc.* **124**, 8204 (2002).
- (46) H. Khurshid, V. Tzitzios, W. Li and G. C. Hadjipanayis *J. Appl. Phys.* **107**, 09A333 (2010).
- (47) J.H. Yin, J. Ding, B.H. Liu, X.S. Miao, J.S. Chen, *J. Magn. Magn. Mater.* **310** (2007) 2537.
- (48) M. T. Johnson, P.G. Kotula, C.B. Carter, *J. Cryst. Growth* **206** (1999) 299.
- (49) Y. Yamamoto, H. Tanaka, T. Kawai, *Jpn. J. Appl. Phys.* **40** (2001) L545.
- (50) B. D. Cullity, *Elements of X-ray Diffraction*, second ed., Addison-Wesley, New York, 1978.
- (51) H.P. Klug, L.E. Alexander, *X-ray Diffraction Procedures for Polycrystalline and Amorphous Materials*, second ed., John Wiley & Son Inc., New York, 1974.
- (52) C.N. Chinnasamy, B. Jeyadevan, K. Shinoda, K. Tohji, D.J. Djayaprawira, M. Takahashi, R. Justin Joseyphus, A. Narayanasamy, *Appl. Phys. Lett.* **83** (2003) 2862.
- (53) P.C. Dorsey, P. Lubitz, D.B. Chrisey, J. S. Horwitz, *J. Appl. Phys.* **79** (1996) 6338.
- (54) M.C. Terzzoli, S. Duhalde, S. Jacobo, L. Steren, C. Moin, *J. Alloys Compd.* **369** (2004) 209.
- (55) Y. Wang, Z.X. Song, D. Ma, X.Y. Wei, K. Xu, *Surface & Coatings Technology* **201** (2007) 5518.
- (56) P. Poddar, S. Srinath, J. Gass, B.L.V. Prasad, H. Srikanth, *J. Phys. Chem. C* **111** (2007) 14060.
- (57) Natl. Bur. Stand. (U.S.) Monogr. **25**, Sec. 9, (1971) 22.
- (58) D. Dimos, W. L. Warren, and H. N. Al-Shareef, *Thin Film Ferroelectric Materials and Devices* ed. by R. Ramesh (Kluwer Academic Publishers, Boston, p. 199, 1997).
- (59) H. N. Al-Shareef, O. Auciello, and A. I. Kingon, *J. Appl. Phys.* **77**, 2146 (1995).
- (60) M. S. Chen, T. B. Wu, and J. M. Wu, *Appl. Phys. Lett.* **68**, 1430 (1996).
- (61) R. Ramesh, W. K. Chan, B. Wilkens, H. Gilchrist, T. Sands, J. M. Tarascon, D. K. Fork, J. Lee, and A. Safari, *Appl. Phys. Lett.* **61**, 1537 (1992).
- (62) R. Ramesh, H. Gilchrist, T. Sands, V. G. Keramidas, R. Haakenaasen, and D. K. Fork, *Appl. Phys. Lett.* **63**, 3592 (1993).

- (63) R. von Helmolt, J. Wecker, B. Holzapfel, L. Schultz, and K. Samwer, *Phys. Rev. Lett.* **71**, 2331 (1993).
- (64) Z. Bi, E. Weal, H. Luo, A. Chen, J. Macmanus-Driscoll, Q. Jia, and H. Wang, *J. Appl. Phys.* **109**, 054302 (2011).
- (65) R. von Helmolt, J. Wecker, B. Holzapfel, L. Schultz, and K. Samwer, *Phys. Rev. Lett.* **71**, 2331 (1993).
- (66) S. Jin, T. H. Tiefel, M. McCormack, R. A. Fastnacht, R. Ramesh, and L. H. Chen, *Science* **264**, 413 (1994).
- (67) W. Eerenstein, M. Wiora, J. L. Prieto, J. F. Scott, and N. D. Mathur, *Nature Mater.* **6**, 348 (2007).
- (68) H. J. A. Molegraaf, J. Hoffman, C. A. F. Vaz, S. Gariglio, D. van der Marel, C. H. Ahn, and J. M. Triscone, *Adv. Mater.* **21**, 3470 (2009).
- (69) V. Garcia, S. Fusil, K. Bouzehouane, S. Enouz-Vedrenne, N. D. Mathur, A. Barthelemy, and M. Bibes, *Nature* **460**, 81 (2009).
- (70) S. M. Wu, S. A. Cybart, P. Yu, M. D. Rossell, J. X. Zhang, R. Ramesh, and R. C. Dynes, *Nature Mater.* **9**, 756 (2010).
- (71) J. Z. Sun, W. J. Gallagher, P. R. Duncombe, L. Krusin-Elbaum, R. A. Altman, A. Gupta, Y. Lu, G. Q. Gong, and G. Xiao, *Appl. Phys. Lett.* **69**, 3266 (1996).
- (72) J. O'Donnell, A. E. Andrus, S. Oh, E. V. Colla, and J. N. Eckstein, *Appl. Phys. Lett.* **76**, 1914 (2000).
- (73) T. Higuchi, T. Yajima, L. Fitting Kourkoutis, Y. Hikita, N. Nakagawa, D. A. Muller, and H. Y. Hwang, *Appl. Phys. Lett.* **95**, 043112 (2009).
- (74) Z. Bi, E. Weal, H. Luo, A. Chen, J. L. MacManus-Driscoll, Q. Jia, and H. Wang, *J. Appl. Phys.* **109**, 054302 (2011).
- (75) M. H. Huang, Y. Wu, H. Feik, N. Tran, E. Weber and P. Yang, *Adv. Mater.* **13**, 113 (2001).
- (76) Y. C. Kong, D. P. Yu, B. Zhang, W. Fang, and S. Q. Feng, *Appl. Phys. Lett.* **78**, 407 (2001).
- (77) J. J. Wu and S. C. Liu, *Adv. Mater.* **14**, 215 (2002).
- (78) Y. Lin, Y. Liu, and H. A. Sodano, *Appl. Phys. Lett.* **95**, 122901 (2009).
- (79) S. J. Limmer, S. Seraji, M. J. Forbess, Y. Wu, T. P. Chou, C. Nguyen, and G. Z. Cao, *Adv. Mater.* **13**, 1269 (2001).
- (80) M. Alexe, D. Hesse, V. Schimdt, S. Senz, H. J. Fan, M. Zacharias, and U. Gösel, *Appl. Phys. Lett.* **89**, 172907 (2006).

- (81) Y.Zhang, J.X.Zhang, and Q.M.Lu: Rapid Synthesis of $\text{Ca}_2\text{Co}_2\text{O}_5$, *Journal of Alloys and Compounds* 399 (2005), p.64.
- (82) T. Wangenstein, T. Dhakal, M. Merlak, S. Chandra, P. Mukherjee, S. Witanachchi M. H. Phan, and H. Srikanth : Growth of uniform ZnO nanoparticles by a microwave plasma process, Submitted Nov.(2010) to *Journal of Alloys and Compounds*.
- (83) T. Wangenstein, S. Witanachchi, and P. Mukherjee: Initial Studies of thermoelectric nanoparticle growth using a laser-assisted spray pyrolysis (LASP) method, Presented at
- (84) A. Datta, and G.S. Nolas, *CrystEngComm*. 2011, **13**, 2753.
- (85) S. J. Peppiatt, *Proc. R. Soc. London, Ser. A*, 1975, **345**, 401.
- (86) G. L. Allen, R. A. Bayles, W. W. Gile and W. A. Jesser, *Thin Solid Films*, 1986, **144**, 297.
- (87) P. Pawlow, *Z. Phys. Chem., Stoechiom. Verwandtschaftsl.*, 1909, **65**, 545.
- (88) E. A. Olson, M. Y. Efremov, M. Zhang, Z. Zhang and L. H. Allen, *J. Appl. Phys.*, 2005, **97**, 034304.
- (89) R. Martin-Lopez, B. Lenoir, X. Devaux, A. Dauscher and H. Scherrer, *Mater. Sci. Engin. A*, 1998, **248**, 147.
- (90) J. Martin, G.S. Nolas, H. Wang, and J.J. Yang, *J. Appl. Phys.* 2007, **102**, 103719.
- (91) J. P. Heremans, and C.M. Jaworski, *Appl. Phys. Lett.* 2008, **93**, 122107.
- (92) C.F. Gallo, B.S. Chandrashekhar, and P.H. Sutter, *J. Appl. Phys.* 1963, **34**, 144.
- (93) R. Radebaugh, Infrared Technology and Applications, *Proceedings of SPIE* **4130**, 363 (2000).
- (94) Phan et al., *Appl. Phys. Lett.* **93**, 252505 (2008).
- (95) Phan et al. *J. Appl. Phys.* **107**, 09A910 (2010).